# Direct generation of three-photon entanglement using cascaded downconversion

by

Deny R. Hamel

A thesis
presented to the University of Waterloo
in fulfillment of the
thesis requirement for the degree of
Doctor of Philosophy
in
Physics

Waterloo, Ontario, Canada, 2013

I hereby declare that I am the sole author of this thesis. This is a true copy of the thesis, including any required final revisions, as accepted by my examiners.

I understand that my thesis may be made electronically available to the public.

# Abstract

High quality entangled photon sources are a key requirement for many promising quantum optical technologies. However, the production of multi-photon entangled states with good fidelity is challenging. Current sources of multi-photon entanglement require the use of post-selection, which limits their usefulness for some applications. It has been an open challenge to create a source capable of directly producing three-photon entanglement. An important step in this direction was achieved with the demonstration of photon triplets produced by a new process called cascaded downconversion, but these previous measurements were not sufficient to show whether these photons were in an entangled state and only had detection rates of five triplets per hour. In this thesis, we show the first demonstration of a direct source of three-photon entanglement. Our source is based on cascaded downconversion, and we verify that it produces genuine tripartite entanglement in two degrees of freedom: energy-time and polarization.

The energy-time entanglement is similar to a three-particle generalization of an Einstein-Podolski-Rosen state; the three photons are created simultaneously, yet the sum of their energies is well defined, which is an indication of energy-time entanglement. To prove it, we use time-bandwidth inequalities which check for genuine tripartite entanglement. Our measurements show that the state violates the inequalities with what constitute, to the best of our knowledge, the strongest violation of time-bandwidth inequalities in a tripartite continuous-variable system to date.

We create polarization entanglement by modifying our experimental setup so that two downconversion processes producing orthogonally polarized triplets interfere to create Greenberger-Horne-Zeilinger states. By using highly efficient superconducting nanowire single photon detectors, we improve the detected triplet rate by 2 orders of magnitude to 660 triplets per hour. We characterize the state using quantum state tomography, and find a fidelity of 86% with the ideal state, beating the previous best value for a three-photon entangled state fidelity measured by tomography. We also use the state to perform two tests of local realism. We violate the Mermin and Svetlichny inequalities by 10 and 5 standard deviations respectively, the latter being the strongest violation to date. Finally, we show that, unlike previous sources of tree-photon entanglement, our source can be used as a source of heralded Bell pairs. We demonstrate this by measuring a CHSH inequality with the heralded Bell pairs, and by reconstructing their state using quantum state tomography.

## Acknowledgements

First, I want to thank my two co-supervisors, Dr. Kevin Resch and Dr. Thomas Jennewein. They have given me the opportunity to do amazing science with them over the last years, and they have been incredibly supportive of my projects and helpful with all of my questions. I also wish to thank the members of my committee, Dr. Donna Strickland and Dr. Joseph Emerson for their feedback and guidance. Finally, I want to thank Dr. Alan Migdall for agreeing to serve as my external examiner for my defence.

I am lucky to have a family that has always been supportive of my studies; I must thank my parents Normand and Denise, and my sister Elyse for their encouragement over the years. I want to thank Catherine for sticking by me through the often unpredictable journey that is a graduate degree, and maybe also for providing me with little bit of extra motivation to finish in a reasonable amount of time. Your love and understanding mean so much to me.

Acknowledgment must be given to the agencies that helped fund my graduate studies. I have been extremely fortunate to receive funding during my PhD studies from the NSERC Vanier Canada Graduate Scholarships, Ontario Graduate Scholarships, the Institute for Quantum Computing and the University of Waterloo Department of Physics & Astronomy.

I am infinitely indebted to Sae Woo Nam and his team at NIST for lending us the superconducting nanowire single-photon detectors we used for our final triplet experiments. I don't know how much time these detectors took off of my PhD, but I do know that we wouldn't have gotten such good data without them. Huge thanks also go to Aaron Miller and Krister Shalm who worked so hard to get those detectors working in Waterloo on a freezing cold week in January.

I was also fortunate to work with some awesome post-docs during my PhD: Robert Prevedel early on for an experiment on entropic uncertainty principles; Hannes Hübel and Krister Shalm who worked with me on the cascaded downconversion experiments; Zhizhong Yan who worked on the NFAD detectors; and Piotr Kolenderski who performed time-resolved double-slit experiment. I have certainly learned from all of your wisdom and experience.

Being a member of two research groups, I was lucky to have many brilliant colleagues. I would like to thank from Kevin's group: Jonathan Lavoie for being the first student to jump through all the hoops, so that I could learn from his experience, and for letting me steal light from his laser when I needed it to align my interferometer; Kent Fisher for his contribution to the entropic uncertainty experiments, for his love of puns and for uploading the explanation of an optical C-NOT on the group wiki so I could study it the night before my comprehensive exam; John Donohue for all of his wordsmithing prowess and infinite trivia knowledge; Mike Mazurek for all of his great saves and for splitting the Clif bars with me, so I don't have to eat the chocolate chip flavored ones; Maggie Agnew for being an awesome experimentalist and hockey player; and Lydia Vermeyden for taking care of my first Sagnac source and making it hers — that is to say, better.

From Thomas's group, I am grateful to: Evan for helping me figure out all aspects of life, from quantum optics to commuting, and for taking over the triplets experiment; Rolf Horn who I could always count on to be in the lab for some life advice, a good laugh and some great science discussions; Chris Erven who worked with me on my original Sagnac source; Jean-Philippe Bourgoin and Aimee Gunther for helping with the triplet setup; Tong Zhao who worked on the PID controller for the active phase stabilization; Catherine Holloway for her constant updates on cycling safety; and Chris Pugh, for being possibly the most cheerful person I've ever met.

Finally, I want to thank all the other great people at IQC and UW whose presence helped make my time in Waterloo wonderful, from everyone who participated in those great cookie time conversations to the members of the Spin Ice hockey team and the IQC ball hockey team.

## Dedication

À ma famille

# Contents

# List of Tables

# List of Figures

# Chapter 1

# Background

## 1.1 Introduction

Quantum information science is a field which aims to harness the properties of quantum mechanics for a wide variety of applications such as quantum computing [1, 2, 3], quantum cryptography [4, 5] and quantum metrology [6, 7, 8]. Various physical systems are being studied for these applications, varying from trapped ions or neutral atoms to spin systems in diamond NV centers and superconducting qubits [9].

One particularly interesting physical system for the study of quantum information is light. In a way it is quite unique. For most quantum information platforms, the main problem is to prevent interactions; the system should not interact with the environment, and different parts of the system should not interact with each other at the wrong times. Preventing or mitigating these unwanted effects is very difficult, and is the subject of intensive research. In optics the problem is reversed; the big challenge comes from the fact that photons do not interact much with each other.

We have to resort to other means to make photons act on each other. This is mainly done in two ways in quantum optics: either when the photons are created by a nonlinear process, or when they are detected. Therefore, any novel capability in state preparation — particularly in entangled photon creation — greatly enhances the range of possible quantum optics experiments.

In this thesis, we present such an improvement in state preparation. We demonstrate a novel source of three-photon entanglement based on cascaded downconversion. Unlike other sources of multi-photon entanglement, it produces entangled photon triplets directly, without depending intrinsically on post-selection.

The structure of this thesis is dictated by the two main experiments performed with this source. These are presented in Chapters 3 and 4. The first is a published letter and the second is a manuscript for an article which will be submitted soon. As these chapters contain articles which are meant to stand on their own, they are not limited to results, containing some background and theory as well. They are however not exhaustive, so we precede the results with two other chapters. This chapter aimed to provide background and motivation for those experiments, whereas Chapter 2 will present theory to complement the results in following chapters. Finally, Chapter 5 presents additional experimental details that were not included in Chapters 3 and 4, but which could be of interest to others pursuing similar experiments.

## 1.2 Entanglement

Quantum entanglement lies at the heart of the experiments described in this thesis. Later, in Section 2.1, we will discuss what it is more formally. First, let us go over some of the important highlights in its history.

The interest in quantum entanglement goes back to 1935. The term is attributed to Schrödinger [10], and was coined in response to concerns brought about by Einstein, Podolski and Rosen (EPR) about the completeness of quantum mechanics [11]. Entanglement was seen as a peculiar feature of quantum mechanics: something counter-intuitive, which according to EPR indicated that quantum mechanics was an incomplete theory. The predictions of quantum mechanics for entangled states were at odds with their view that the world was local and realistic[1].

---

[1] The two fundamental premises of EPR are *locality* and *realism*. Locality means that no information can travel faster than the speed of light. Realism means that if the outcome of a measurement can be predicted with absolute certainty, it is an element of physical reality.

A conceptual breakthrough in the study of entanglement was made by John Bell, who showed that the assumptions of locality and realism were in some cases incompatible with the predictions of quantum mechanics [12]. Such results are now called *Bell inequalities.* Once Bell's results were adapted in a way that they would be experimentally measurable [13], the next requirement was a source of entangled particles which could be used to perform these experiments. The first solution was to use pairs of photons produced by an atomic cascade of calcium. This was used in several early experimental verifications of Bell inequalities, like the experiment by Freedman and Clauser [14], as well as those by Aspect et al.[15, 16, 17]. However, atomic cascades are not ideal; photons are emitted in random directions, making them hard to collect and working with single atoms is difficult [18]. Soon a more practical way to produce photonic entanglement was found: a nonlinear optical process called spontaneous parametric downconversion.

## 1.3 Downconversion and photonic entanglement

Spontaneous parametric downconversion (SPDC), also known as parametric downconversion, parametric fluorescence, or just downconversion, is a process which can produce photon pairs in a nonlinear material. It was first demonstrated by Harris at al. [19] and Magde & Mahr [20] in 1967. Later it was shown that, in agreement with theoretical predictions [21], downconversion is a process which emits pairs of photons simultaneously [22]. This demonstration confirmed the idea that downconversion can be seen as the annihilation of a pump photon and the simultaneous creation of two twin photons [18]. We will explore this in more detail in Section 2.3.

By the end of the 1980s, downconversion was being used for various experiments on two-photon interference [23]. Around the same time, Ou and Mandel [24] and Shih and Alley [25] showed that downconversion could be used to produce polarization entangled photon pairs. This was followed by many other experiments showing ways of producing polarization entanglement with SPDC [26, 27, 28, 29, 30]. A good review was written by Edamatsu [18], and some of the details are also found in my MSc thesis [31]. Downconversion led to a revolution for photonic entanglement experiments; it made entanglement sources made accessible, and enabled a very large number of experiments with entangled photon pairs. The next step was to adapt these methods to produce multipartite entanglement.

## 1.4 Sources of multi-photon entanglement

Around the same time that SPDC was first employed to produce photonic entanglement, it was becoming clear, for example with the works of Svetlichny [32], Mermin [33], and Greenberger, Horne and Zeilinger [34], that multipartite entanglement had properties distinguishing it from bipartite entanglement. Logically, the next question to ask was how could these states be created. As SPDC had been shown to be useful to produce bipartite photonic entanglement, it was natural to try to extend it to get multipartite entanglement. Greenberger, Horne and Zeilinger suggested a way to do this. They proposed to create a four-photon path-entangled state using a cascade of downconversion [34]. This scheme is the inspiration for the work in this thesis, but when it was proposed, it was not yet realizable as we shall see in Section 1.5.

A few years later, another method to produce multi-photon entanglement, based on quantum erasure, was proposed [35]. The idea of the scheme, explained in more detail in Appendix A, is to interfere independently produced photon pairs. When the photons are detected, only a subset of events is kept based on which detectors registered a photon. This process is called post-selection. With this method, the detection of photons is part of the state preparation. It means that the same physical process which destroys the states — detecting the photons — is the process which also creates the desired quantum states.

However, for many applications this is not a concern. Often we are already forced to post-select on photon detections, since the detectors are not perfectly efficient. The method was first implemented in 1999 to produce a tripartite photon entanglement [36], and was then adapted and scaled up to show four- [37], five- [38], six- [39] and eight- [40] photon entanglement. Other states, such as multi-photon cluster states [41], W state [42] or Dicke states [43] have also been shown, all of them relying on this type of post-selection. Moreover, states produced in this way can be used for linear optical quantum computing [3].

Nonetheless, it is not true that this post-selection can always be ignored. Beyond the questions regarding the existence of a state which is created and destroyed at the same time, there are also some practical limitations brought about by this post-selection. As we shall see in Chapter 4, one such example is the case of heralding Bell pairs. Three particle quantum states which should be sufficient for this task no longer are if they are produced using post-selection as proposed by [35]. Another limitation is that some quantum gates rely on post-selection [44]; these cannot be applied in succession when the state production requires post-selection. It is therefore relevant and important to try to produce multi-photon entangled states using methods that do not require this post-selection.

There have been many proposals of how photon triplets could be produced directly. Perhaps the most straightforward is to use a third order nonlinearity to produce photon triplets spontaneously [45, 46]. However, experiments have so far required seeding at one of the downconversion wavelengths to observe signal [47, 48]. Another possibility is to produce three-photon entangled states by combining two photons from independent downconversions using sum-frequency generation [49, 50]. This idea has been investigated in recent years [50, 51], but has not yet shown to produce photon triplets. The use of three-photon cascade in quantum dots has also been investigated [52], and other, more exotic, processes have also been proposed including electron-positron annihilation [53] and a triple Compton effect [54]. However in this thesis, we will concentrate on the production of entangled photon triplets using cascaded downconversion.

## 1.5 Cascaded downconversion

As we mentioned previously, when cascaded downconversion was first proposed [34], it was not yet experimentally feasible. This was mainly due to the downconversion efficiency of available materials at the time. Indeed, materials like BBO were used, which has an efficiency (see footnote [2]) of around $10^{-12}$. With detectors limited to count rates of less

---

[2] By efficiency we mean the number of pairs of downconversion photons produced per number of pump photons, or equivalently the ratio between the intensity of the downconversion and the intensity of the pump. Note that for most nonlinear processes this definition does not make sense, since the signal intensity scales non-linearly to the pump intensity. For SPDC this scaling is linear, so there is no problem defining the efficiency in this way. SPDC is still considered a nonlinear process, since it relies on a nonlinear response of the material to the electric field.

than around MHz, the best possible count rates with these materials are on the order of 1 triplet per year, making it nearly impossible to get enough statistics for such an experiment.

A large improvement came from the development of novel nonlinear materials. The development of periodic poling for quasi-phasematching, which we will review in Section 2.5, allows for much better downconversion efficiencies by making the largest nonlinear coefficients of materials available and allowing for longer interaction lengths. Additional progress came from integrated waveguides for downconversion, further improving the efficiency of SPDC [55].

With these new materials, cascaded downconversion came within reach. During my MSc, Hannes Hübel and I performed an experiment to show the creation of photon triplets from cascaded SPDC [56]. This was the first experimental demonstration of the direct production of photon triplets. There was however still one important deficiency in this demonstration. While we showed conclusively the creation of photon triplets, this initial experiment did not provide any conclusive evidence that the three photons were entangled in any way. This is a significant limitation, since the very motivation for even trying cascaded downconversion is to use it to produce entangled states.

The experiments in this thesis aim to address this problem. The first main result, shown in Chapter 3, is a demonstration that the photon triplets are energy-time entangled. This was done using time-bandwidth uncertainty inequalities, discussed in Section 2.2.3.

The second experiment is shown in Chapter 4. In that experiment, we use cascaded downconversion to produce polarization entangled three-photon states, and show the quality of the state using various tests, such as quantum state tomography (see Section 2.2.1) and local realism tests (see section 2.2.4). We also show that the state can be used as source of heralded Bell pairs. Of our two main experiments, this is arguably the more important one because polarization entanglement is usually regarded as a more useful type of entanglement than energy-time entanglement, since it can be more directly applied to many quantum information schemes.

Before getting to these results, we move on to Chapter 2, where we will go over some of the theory and tools which will be useful for a better understanding of the subsequent chapters.

# Chapter 2

# Theory

In this chapter, our goal is to provide some of the theoretical tools which will be useful for the later chapters of the thesis. We begin with a reminder of the basic definitions of entanglement, followed with an overview of methods used to detect entanglement. We then discuss the main method of producing entanglement with photons: spontaneous parametric downconversion.

## 2.1 Entanglement

### Pure states

Since the goal of this thesis is to show multi-photon entanglement from cascaded SPDC, we should begin by defining exactly what is entanglement. First, let us recall that in quantum mechanics, pure states are represented by vectors in a Hilbert space, which may be discrete or continuous. States of composite systems are described as vectors in the space given by the tensor product of the subsystem Hilbert spaces. To be more explicit, let us take two systems, $A$ and $B$, each with their associated Hilbert spaces $\mathcal{H}_A$ and $\mathcal{H}_B$. The state of the joint system is defined as a vector in:

$$\mathcal{H}_{AB} = \mathcal{H}_A \otimes \mathcal{H}_B \tag{2.1}$$

where $\otimes$ represents the tensor product. If we take any two vectors in these subsystems, $|\psi\rangle_A \in \mathcal{H}_A$ and $|\phi\rangle_B \in \mathcal{H}_B$, then the state given by their tensor product:

$$|\mathrm{S}\rangle_{AB} = |\psi\rangle_A \otimes |\phi\rangle_B, \tag{2.2}$$

belongs to the Hilbert space $\mathcal{H}_{AB}$, and is therefore a valid quantum state. Such a state is called *separable.* Any other state, that is any state which cannot be factored in such a way, we can write as:

$$|\mathrm{E}\rangle_{AB} \neq |\psi\rangle_A \otimes |\phi\rangle_B, \tag{2.3}$$

and is called *entangled.*

### Mixed states

The definition of entanglement given above assumes pure states; for mixed state, it needs to be generalized. Mixed states are not represented by a state vector, but by a Hermitian, positive semi-definite operator of trace 1, called the density matrix $\rho$. A mixed state is separable if and only if it can be written as a convex sum of separable states:

$$\rho = \sum_i p_i \rho_i^A \otimes \rho_i^B. \tag{2.4}$$

The condition that the sum must be convex means that $\sum_i p_i = 1$. Any state which cannot be written in this way is entangled.

### Multipartite entanglement

For multipartite pure states, the definition given above can be extended directly. However, for mixed states the situation is slightly more complicated. The definition of entanglement for bipartite mixed states can be extended in two ways: *full inseparability* [57] and *genuine multipartite entanglement* [58]. One has to be particularly careful in distinguishing between these two definitions, since their nomenclature is not uniformly recognized, particularly in older papers.

Full inseparability is defined by looking at the different way in which a mixed state can be factored. A tripartite state may be separable in several different ways:

$$\rho = \sum_i \eta_i \rho_{1,2,i} \otimes \rho_{3,i}, \tag{2.5}$$

$$\rho = \sum_i \eta_i \rho_{1,3,i} \otimes \rho_{2,i}, \tag{2.6}$$

$$\rho = \sum_i \eta_i \rho_{2,3,i} \otimes \rho_{1,i}, \tag{2.7}$$

$$\rho = \sum_i \eta_i \rho_{1,i} \otimes \rho_{2,i} \otimes \rho_{3,i}, \tag{2.8}$$

The first three states are called *biseparable* across a single cut, while the last one is *fully separable.* Any tripartite state which cannot be written in any of the above forms is called *fully inseparable.*

The definition of full separability has limitations if we want to characterize the presence of multipartite entanglement. Indeed, consider the following state:

$$\rho = \frac{1}{2}\rho_{12} \otimes \rho_3 + \frac{1}{2}\rho_1 \otimes \rho_{23}. \tag{2.9}$$

Such a state can be fully inseparable, even though it is clearly just a mixture of different bipartite entangled states. It does not have any “genuine” tripartite entanglement.

A state is therefore said to have *genuine tripartite entanglement* if and only if it cannot be written as a convex sum of fully separable and biseparable states.

### Important entangled states

In this thesis, there are a few important entangled states to which we will refer on several occasions. We are mostly interested with the polarization states of photons. This is a two-level system, often referred to as a qubit. We usually chose as its basis states the horizontal and vertical polarizations, noted as $|H\rangle$ and $|V\rangle$ respectively. For systems containing two qubits, the Bell states are defined as:

$$\begin{aligned} |\phi^{\pm}\rangle &= \frac{1}{\sqrt{2}}\left(|HH\rangle \pm |VV\rangle\right) \\ |\psi^{\pm}\rangle &= \frac{1}{\sqrt{2}}\left(|HV\rangle \pm |VH\rangle\right) \end{aligned} \tag{2.10}$$

These states are maximally entangled, and together form an orthogonal basis in the two-qubit space. We will also use a three-qubit extension of the $|\phi^{\pm}\rangle$ states. These are called GHZ states after Greenberger, Horne and Zeilinger. We define:

$$|\mathrm{GHZ}^{\pm}\rangle = \frac{1}{\sqrt{2}}\left(|HHH\rangle \pm |VVV\rangle\right) \tag{2.11}$$

This is also a maximally entangled state, but for a three qubit system. More states can be added to form what is known as the GHZ basis, but this will not be required for our purposes.

## 2.2 State characterization and entanglement detection

Now that we have covered the definition of entanglement, the next topic to address is how to tell if a state is entangled or not. This is often not a simple task. Indeed, for larger systems there is not even a known general way of telling if an arbitrary density matrix represents an entangled state. There exist however several ways that the presence of entanglement can be detected. In this section we discuss the ones we use in later chapters.

### 2.2.1 Quantum state tomography

One method for determining if a state is entangled is quantum state tomography. Here, the idea is to completely reconstruct the density matrix of the quantum state, by doing a series of measurements on an ensemble of states. Once the density matrix is obtained, although there is no efficient *general* test to determine if it represents an entangled state, there are various entanglement criteria which can be used [59]. The advantage of quantum state tomography is that it essentially provides all of the information about the state, allowing us to conclude much more than just whether or not the state is entangled. For example, from the density matrix we can calculate the purity of the state or it's fidelity with a target state. As can be expected, this additional information comes at a cost. Compared to other entanglement criteria, quantum state tomography requires a lot more measurements. Indeed, for a state of $n$ qubits, a minimum of $4^n$ projective measurements are required[1], one for each free parameter of the density matrix plus one for normalization.

From these measurements, the density matrix must then be reconstructed. This can be done in a few ways. In this thesis, we use a method called maximum likelihood [60, 61]. In this technique, the un-normalized density matrix is parameterized according to its 16 free parameters in such a way that it is always physical. We then find the set of parameters which gave the best fit with the data. An overview of how this is done can be found in my MSc thesis [31].

### 2.2.2 Entanglement witnesses

To address the issue caused by the large number of measurements required for quantum state tomography, we can use entanglement witnesses. These are defined as follows: an observable $W$ is an entanglement witness if and only if it satisfies the following properties [59]:

$$\begin{aligned} &\mathrm{Tr}(W\rho_s) \geq 0 \text{ for any separable state } \rho_s \\ &\mathrm{Tr}(W\rho_e) < 0 \text{ for at least one entangled state } \rho_e. \end{aligned} \tag{2.12}$$

Therefore, if we can experimentally measure an entanglement witness, and we find that the measured expectation value is negative, then we know that the state is entangled. It

---

[1] This number of measurements assumes projective measurements where only one outcome of the measurement is used. If we measure both outcomes of a measurement, then $3^n$ measurements are required [59].

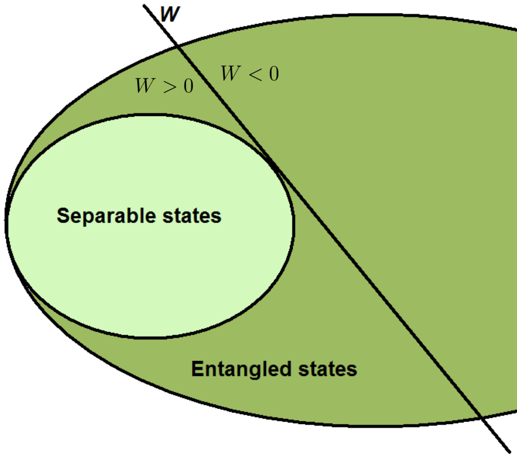

Figure 2.1: Visual representation of an entanglement witness. Separable states form a convex subset of the set of all states. The straight line represents the hyperplane where $\mathrm{Tr}(W\rho) = 0$. This figure and its caption were originally published in my MSc thesis [31].

is clear from the definition that an entanglement witness can never conclusively tell us if a state is separable [59]. This statement is easy to grasp by looking at Figure 2.1, which is a visual representation of the above definition. However, the inability of entanglement witnesses to determine conclusively the separability of a state is not a concern for us in this thesis, as we are interested in showing entanglement rather then the lack of it.

In theory, for any entangled state, there exists a witness which can detect it. This is called the completeness of entanglement witnesses theorem [62]. However, the theorem does not imply that it is easy to find a witness that will detect a given quantum state. In fact, finding a witness which to detect a particular quantum state is not trivial, particularly if it needs to be implemented experimentally. Nonetheless, for many classes of states there are known entanglement witnesses which are possible to implement. An excellent review of this topic was written by Gühne and Tóth [59]. Various witnesses can be used depending on the task at hand. For example, sometimes different witnesses will offer a tradeoff between the number of measurements and tolerances to noise.

We mentioned earlier that the advantage of entanglement witnesses is that they do not require as many measurements as quantum state tomography. This advantage is in some cases drastic, and never more so than for GHZ states [63], which are states of the form:

$$|\mathrm{GHZ}\rangle = \frac{1}{\sqrt{2}}(|00...0\rangle + |11...1\rangle). \tag{2.13}$$

Indeed, it is somewhat surprising that a GHZ state containing any number of qubits can be detected using only two local measurement settings[2]. In the three-qubit case, a witness is given by:

$$W = \frac{3}{2} - \sigma_x^{(1)}\sigma_x^{(2)}\sigma_x^{(3)} - \frac{1}{2}\left[\sigma_z^{(1)}\sigma_z^{(2)} + \sigma_z^{(1)}\sigma_z^{(3)} + \sigma_z^{(2)}\sigma_z^{(3)}\right] \tag{2.14}$$

where $\sigma_x = |H\rangle\langle V| + |V\rangle\langle H|$ and $\sigma_z = |H\rangle\langle H| - |V\rangle\langle V|$ are Pauli measurements. It goes without saying that being able to detect entanglement with only two measurement settings regardless of the number of particles is a huge advantage compared to the number of measurements required for quantum state tomography. This is particularly true for experiments where it takes a long time to accumulate enough statistics for each measurement setting, such as experiments with cascaded downconversion. We therefore used this witness for the first detection of three-photon GHZ states produced by cascaded downconversion. This experiment is presented in Section 5.5.

### 2.2.3 Uncertainty relations

The history of uncertainty relations as entanglement criteria began with the famous paper by Einstein, Podolski and Rosen which presented what is now known as the EPR paradox [11]. In their attempt to show that quantum mechanics is incomplete, the authors introduced a quantum state of two particles with the following form:

$$\psi(x_1, x_2) = \int_{-\infty}^{\infty} e^{\frac{i(x_1 - x_2 + x_0)p}{\hbar}} dp, \tag{2.15}$$

---

[2] Here by "measurement settings" we refer to the number of projective measurements that need to be applied to the state to obtain the witness, assuming that all the outcomes of the projective measurements are measured. For example, the witness in Equation 2.14 has four terms, but the three last terms can all be obtained by measuring $\sigma_z^{(1)}\sigma_z^{(2)}\sigma_z^{(3)}$ and combining the counts in different ways.

where $x_0$ is a constant. This state is an eigenstate of two observables: the difference in position of the particles, $x_1 - x_2$, and the sum of their momenta, $p_1 + p_2$. Based on two fundamental assumptions, *locality* and *realism*, Einstein et al. argued the following: with the two particles spatially separated, one could measure either the position or momentum of the first particle and thus immediately know with certainty the corresponding position or momentum of the second particle. To them, this meant that the second particle must of had a well-defined position and momentum, in violation of Heisenberg's uncertainty principle.

Strictly speaking however, there is no paradox; there is no uncertainty principle between $x_1 - x_2$ and $p_1 + p_2$ as they are commuting observables. What we now know is that the state in Equation 2.15 is entangled, and that this is why we can simultaneously have $\Delta(x_1 - x_2) = 0$ and $\Delta(p_1 + p_2) = 0$. The role of these uncertainties as an indicator for entanglement was formalized in 2000 by Duan et al. [64]. They showed that for the observables:

$$u = |a|x_1 + \frac{1}{a}x_2 \tag{2.16}$$

and

$$v = |a|p_1 - \frac{1}{a}p_2, \tag{2.17}$$

where $a$ is a constant and the commutation relation between $x_i$ and $p_j$ is $[x_i, p_j] = i\delta_{i,j}$ (see footnote [3]), we have:

$$\langle(\Delta u)^2\rangle_\rho + \langle(\Delta v)^2\rangle_\rho \geq a^2 + \frac{1}{a^2}, \tag{2.18}$$

where $\langle(\Delta u)^2\rangle_\rho = \langle u^2\rangle_\rho - \langle u\rangle_\rho^2$ is the variance of a measurement of the observable $u$ on the separable state $\rho$. Since this holds for any separable state, if a state happens to violate this inequality, it cannot be separable and must therefore be entangled. This type of inequality can thus be used as a method to detect entanglement.

The EPR observables we discussed earlier are just the special case when $a = -1$. In this case, the inequality becomes:

---

[3] This is the usual canonical commutation relation with $\hbar = 1$.

$$\langle[\Delta(x_1 - x_2)]^2\rangle_\rho + \langle[\Delta(p_1 + p_2)]^2\rangle_\rho \geq 2. \tag{2.19}$$

The EPR state is an example of a state which violates the inequality, proving that it is entangled.

It is sometimes more practical to turn these inequalities into product inequalities. To show how this can be done, we note that since the inequalities only depend on the commutation relation between $x_i$ and $p_j$, they also hold if these variables are rescaled as $x'_i = sx_i$ and $p'_j = p_j/s$. For example, taking Equation 2.19 and rescaling the variables we have:

$$[\Delta(sx_1 - sx_2)]^2 + [\Delta(\frac{p_1}{s} + \frac{p_2}{s})]^2 \geq 2. \tag{2.20}$$

We have dropped the expectation value and the state subscript $\rho$ for simplicity, but this equation and the ones to follow should still be understood as being applicable to the expectation values for separable states. We can factor out the scaling constant from the variances as follows:

$$s^2[\Delta(x_1 - x_2)]^2 + \frac{1}{s^2}[\Delta(p_1 + p_2)]^2 \geq 2. \tag{2.21}$$

The inequality is valid for any value of $s$. What we want to find is the value of $s$ that minimizes the left-hand side of the inequality. We do this in the usual way, by setting its derivative with respect to $s$ to 0 and solving for s.

$$\frac{\partial}{\partial s}s^2[\Delta(x_1 - x_2)]^2 + \frac{1}{s^2}[\Delta(p_1 + p_2)]^2 = 2s[\Delta(x_1 - x_2)]^2 - \frac{2}{s^3}[\Delta(p_1 + p_2)]^2 = 0 \tag{2.22}$$

Solving for $s$, or rather for $s^2$, we obtain:

$$s^2 = \frac{\Delta(p_1 + p_2)}{\Delta(x_1 - x_2)}. \tag{2.23}$$

By substituting this value of $s^2$ into the inequality 2.21, we find:

$$\frac{\Delta(p_1+p_2)}{\Delta(x_1-x_2)}[\Delta(x_1-x_2)]^2 + \frac{\Delta(x_1-x_2)}{\Delta(p_1+p_2)}[\Delta(p_1+p_2)]^2 \geq 2, \tag{2.24}$$

which simplifies to:

$$\Delta(x_1-x_2)\Delta(p_1+p_2) \geq 1. \tag{2.25}$$

This is the product form of inequality 2.19. As will be discussed in Chapter 3, these kinds of variance inequalities can be generalized for multipartite entanglement. This was done by van Loock and Furusawa [65], who derived inequalities which verify the presence of full inseparability. In Chapter 3, we adapt these inequalities so that they detected genuine tripartite entanglement, and use our new inequalities to prove that the photon triplets produced by cascaded downconversion are entangled in energy-time.

### 2.2.4 Local realism tests

The first tests of local realism were invented by John Bell, as a way of quantitatively addressing the questions of locality and realism brought up by EPR. These tests, known as Bell inequalities, put bounds on the measurement results possible if nature obeys the principles of locality and realism. Because their derivation deliberately ignores quantum mechanics, it might seem strange to consider them as entanglement criteria, since entanglement is a property of quantum mechanical states. However, it can be shown that in the framework of quantum mechanics, any state violating a Bell inequality must be entangled. Bell inequalities are therefore entanglement criteria [4]. We use these local realism tests in Chapter 4 to verify the presence of entanglement in a three-photon state, and in a heralded two-photon state.

Let us show how to derive three different tests of local realism which are used to verify entanglement of two- or three-photon systems in Chapter 4 of this thesis. These derivations are adapted from Lavoie et al. [66].

---

[4] In fact, any Bell inequality can be transformed into an entanglement witness. Indeed, for any Bell inequality of the form $S_{\mathrm{Bell}} \geq X$, the operator defined as $W_{\mathrm{Bell}} = X - S_{\mathrm{Bell}}$ is a witness according to the definition in Section 2.2.2.

### CHSH inequality

We start by considering a case with two particles A and B. We assume that these are very far apart, so that they may not be influenced by each other or by measurements performed on the other. This is the assumption of locality. For each particle, one of two measurements may be chosen, $\mathbf{a}$ or $\mathbf{a}'$ for particle A, and $\mathbf{b}$ or $\mathbf{b}'$ for particle B. Each of these measurements has two possible outcomes: $+1$ or $-1$. According to realism, the outcome of each measurement is determined by the properties of the particle. In other words, for particle A, if measurement $\mathbf{a}$ is chosen, the measurement outcome $a = \pm 1$ is predetermined. If instead we chose to measure $\mathbf{a}'$, then we will get the measurement outcome $a' = \pm 1$, which is also predetermined. The same is true for particle B. This implies that for any single measurement of this experiment, either $b - b' = 0$ and $b + b' = \pm 2$ or $b + b' = 0$ and $b - b' = \pm 2$. Therefore, we will have:

$$\begin{aligned} S_2 &= a(b + b') + a'(b - b') = \pm 2 \\ S_2' &= a(b' - b) + a'(b + b') = \pm 2. \end{aligned} \tag{2.26}$$

If we repeat a measurement of $S_2$ multiple times, we will always obtain a value of either $-2$ or 2. Therefore, expanding the terms and averaging over many runs of the experiment, we get:

$$-2 \leq \langle ab \rangle + \langle ab' \rangle + \langle a'b \rangle - \langle a'b' \rangle \leq 2, \tag{2.27}$$

which gives us the following CHSH inequality:

$$|E(\mathbf{a}, \mathbf{b}) + E(\mathbf{a}, \mathbf{b}') + E(\mathbf{a}', \mathbf{b}) - E(\mathbf{a}', \mathbf{b}')| \leq 2. \tag{2.28}$$

Here, we have rewritten the ensemble average of the product of measurement outcome, $\langle ab \rangle$, as the correlation function $E(a, b)$.

**Mermin inequality**

We can expand the derivation to a case with three particles. We add a third particle C, with its own measurement settings $\mathbf{c}$ or $\mathbf{c}'$. It also has predetermined outcomes $c = \pm 1$ and $c' = \pm 1$. This means that either $c - c' = 0$ and $c + c' = \pm 2$, or $c + c' = 0$ and $c - c' = \pm 2$. Combining this fact with Equation 2.26 yields:

$$S_3 = S_2(c' - c) + S_2'(c + c') = -2abc + 2ab'c' + 2a'bc' + 2a'b'c = \pm 4. \tag{2.29}$$

If we average this result over many runs of the experiments, we get the Mermin inequality for three particles:

$$|E(\mathbf{a}', \mathbf{b}', \mathbf{c}) + E(\mathbf{a}', \mathbf{b}, \mathbf{c}') + E(\mathbf{a}, \mathbf{b}', \mathbf{c}') - E(\mathbf{a}, \mathbf{b}, \mathbf{c})| \leq 2. \tag{2.30}$$

**Svetlichny inequality**

To obtain the Svetlichny inequality, we allow for arbitrarily strong correlations between the particles A and B, but assume that particle C is completely independent. In this model, the factorization in Equation 2.26 is no longer valid. We have to write:

$$\begin{aligned} \bar{S_2} &= (ab) + (ab') + (a'b) - (a'b') = \pm 4 \\ \bar{S_2'} &= -(ab) + (ab') + (a'b) + (ab') = \pm 4. \end{aligned} \tag{2.31}$$

Each value in parenthesis has a value of ±1, which is predetermined. Because $\bar{S_2}$ and $\bar{S_2'}$ depend on those same four values, we know that if one of them is 4, the other one must be 0. By studying all the possible combinations of values, we can see that[5]:

$$\bar{S_2}c - \bar{S_{2'}}c' = (ab)c + (ab)c' + (ab')c - (ab')c' + (a'b)c - (a'b)c' - (a'b')c - (a'b')c' = 0, \pm 4. \tag{2.32}$$

This is easier to see if we factor the previous equation in the following way:

---

[5] Note that the derivation in [66] mistakenly states that this equation can also be equal to ±2.

$$\bar{S}_2 c - \bar{S}_{2'} c' = [(ab) - (a'b')][c + c'] + [(ab') + (a'b)][c - c'] = 0, \pm 4. \tag{2.33}$$

Since the result of individual measurements is always between −4 and +4, then by averaging over many measurements we will get:

$$\begin{aligned} S_{\text{Svet}} = |&E(\mathbf{a},\mathbf{b},\mathbf{c}) + E(\mathbf{a},\mathbf{b},\mathbf{c}') + E(\mathbf{a},\mathbf{b}',\mathbf{c}) - E(\mathbf{a},\mathbf{b}',\mathbf{c}') \\ &+ E(\mathbf{a}',\mathbf{b},\mathbf{c}) - E(\mathbf{a}',\mathbf{b},\mathbf{c}') - E(\mathbf{a}',\mathbf{b}',\mathbf{c}) - E(\mathbf{a}',\mathbf{b}',\mathbf{c}')| \leq 4, \end{aligned} \tag{2.34}$$

which is the Svetlichny inequality.

## 2.3 Spontaneous parametric downconversion

The main method of producing entangled photons is through the use of spontaneous parametric downconversion. This process, which can be understood as a time reversal of sum frequency generation, produces photons in pairs. To see this, we can consider the following Hamiltonian for SPDC, which is obtained by quantizing the classical electric field energy density in a nonlinear medium [67, 68]:

$$\hat{H} = -\frac{\epsilon_0}{3} \int_V d^3r \chi^{(2)} \hat{E}_p^{(+)} \hat{E}_s^{(-)} \hat{E}_i^{(-)} + H.c. \tag{2.35}$$

Here $\chi^{(2)}$ is an element of the second order nonlinear susceptibility tensor, $\epsilon_0$ is the vacuum permittivity, *H.c.* is the Hermitian conjugate and $s$ and $i$ are indices representing the two downconverted modes. Usually, the pump field can be treated classically, while the downconverted fields must be treated in a quantum way. We consider the pump to be a monochromatic plane wave propagating in the $z$ direction. It can be written as:

$$\hat{E}_p^{(+)} = \alpha e^{i(k_p z - \omega_p t)}, \tag{2.36}$$

where $\alpha$ is the classical electric field amplitude. The two downconverted fields, which we need to keep quantized, are given by:

$$\hat{E}_j^{(-)} = -i \sum_{\vec{k_j}} \sqrt{\frac{\hbar \omega_{j,\vec{k_j}}}{2\epsilon_0 V}} \vec{\epsilon}_{\vec{k_j}} \hat{a}^\dagger_{j,\vec{k_j},} e^{-i(\vec{k_j} \cdot \vec{r} - \omega_{\vec{k_j}} t)}. \tag{2.37}$$

We will assume that the downconverted fields are plane waves also propagating along the $z$ axis, and we will only consider a single polarization. The electric field operators can thus be simplified to:

$$\hat{E}_j^{(-)} = -i \sum_{k_j} \sqrt{\frac{\hbar \omega_{j,k_j}}{2\epsilon_0 V}} \hat{a}^\dagger_{j,k_j} e^{-i(k_j z - \omega_{k_j} t)}. \tag{2.38}$$

By substituting this form of the electric field operators $\hat{E}_0^{(-)}$ and $\hat{E}_1^{(-)}$ in the Hamiltonian of Equation 2.35, we find:

$$\hat{H} = \frac{\epsilon_0}{3} \alpha \sum_{k_s,k_i} \int_V d^3r \chi^{(2)} \left[ -i \sqrt{\frac{\hbar \omega_{k_s}}{2\epsilon_0 V}} \right] \left[ -i \sqrt{\frac{\hbar \omega_{k_i}}{2\epsilon_0 V}} \right] \hat{a}^\dagger_{k_s} \hat{a}^\dagger_{k_i} e^{i(k_p - k_s - k_i)z} e^{i(\omega_{k_s} + \omega_{k_i} - \omega_p)t} + H.c. \tag{2.39}$$

From this, we can find the effective quantum state after the interaction. The quantum state evolves according to:

$$|\psi(t)\rangle = \exp\left[ \frac{1}{i\hbar} \int_{-t/2}^{t/2} dt' \hat{H}(t') \right] |\text{vac}\rangle \tag{2.40}$$

where $|\text{vac}\rangle$ represents the vacuum state. Expanding the exponential to the first order yields:

$$|\psi(t)\rangle \sim |\text{vac}\rangle + \frac{1}{i\hbar} \int_{-t/2}^{t/2} dt' \hat{H}(t') |\text{vac}\rangle. \tag{2.41}$$

By combining Equations 2.41 and Equation 2.39, we find that the non-vacuum portion of the quantum state is proportional to:

$$\psi(t)\rangle \sim \frac{\epsilon_0}{3i\hbar}\alpha \sum_{k_s,k_i}\int_0^t dt' \int_V d^3r\chi^{(2)} \left[-i\sqrt{\frac{\hbar\omega_{k_s}}{2\epsilon_0 V}}\right]\left[-i\sqrt{\frac{\hbar\omega_{k_i}}{2\epsilon_0 V}}\right]\hat{a}^\dagger_{k_s}\hat{a}^\dagger_{k_i} e^{i(k_p-k_s-k_i)z} e^{i(\omega_{k_s}+\omega_{k_i}-\omega_p)t'}|\text{vac}\rangle. \tag{2.42}$$

We have to do two integrations, one in space and one in time. For the integration in time, we assume that interaction time is long [69], so that we can use the following relation:

$$\lim_{t\to\infty}\int_{-t/2}^{t/2} dt' e^{i\Delta\omega t'} = 2\pi\delta(\Delta\omega), \tag{2.43}$$

with $\Delta\omega = \omega_s + \omega_i - \omega_p$. For the integration in space, the $x$ and $y$ directions are straightforward since we assumed plane waves. For the $z$ direction, we have:

$$\int_0^{L_z} dz' e^{i\Delta k z'} = e^{i\frac{\Delta k L_z}{2}} L_z \,\text{sinc}\left(\frac{\Delta k L_z}{2}\right), \tag{2.44}$$

where $\Delta k = k_p - k_s - k_i$ and $L_z$ is the length of the crystal. If we combine the results of the two integrations in Equations 2.44 and 2.43 with Equation 2.42, and ignore some of the constants, we are left with:

$$|\psi(t)\rangle \sim \alpha\chi^{(2)} \sum_{k_s,k_i} \sqrt{\omega_{k_s}\omega_{k_i}}\,\delta\left(\frac{\Delta\omega}{2}\right)\text{sinc}\left(\frac{\Delta k L_z}{2}\right)|1_{\omega_{k_s}}, 1_{\omega_{k_i}}\rangle. \tag{2.45}$$

Let us focus on some of the consequences of the form of the quantum state in Equation 2.45. The first is that photons at $\omega_s$ and $\omega_i$ are produced in pairs. Secondly, the delta function imposes:

$$\omega_p = \omega_s + \omega_i, \tag{2.46}$$

which is referred to as energy conservation. The sinc function means that in order to get appreciable signal, we need:

$$k_p \approx k_s + k_i. \tag{2.47}$$

This condition is called phasematching, which we will discuss in more detail in Section 2.5.

To produce polarization entangled pairs, we need two processes producing photon pairs as in Equation 2.45 that can interfere coherently. This can be done in several ways, either with different phasematching conditions in a crystal [27], with two different crystals [28, 70, 71] or with a single crystal pumped in two directions [30]. An overview of these methods was presented in my MSc thesis [31], and another good reviews is given by Edamatsu [18].

## 2.4 Cascaded spontaneous parametric downconversion

We have seen in the previous section that applying the SPDC Hamiltonian to the vacuum leads to a quantum state containing pairs of photons. For cascaded downconversion, we require two SPDC Hamiltonians, which are applied one after the other. The first one is the same Hamiltonian given in Equation 2.35, but in this section we will write it in a simplified single frequency form as:

$$\hat{H}_1 = \alpha\lambda_1 \hat{a}_0^\dagger \hat{a}_1^\dagger + H.c, \tag{2.48}$$

where $\lambda_1$ is a parameter characterizing the strength of the interaction. The two downconverted modes are now referred to as modes 0 and 1, to be consistent with the convention used in Chapter 4. For the second Hamiltonian, the pump beam is at frequency $\omega_0$, and the two downconverted frequencies are $\omega_2$ and $\omega_3$. The mode at $\omega_0$ cannot be treated classically, as it is a non-classical state produced by the first SPDC. The Hamiltonian can be written as:

$$\hat{H}_2 = \lambda_2 \hat{a}_0 \hat{a}_2^\dagger \hat{a}_3^\dagger + H.c. \tag{2.49}$$

To get the final quantum state, we need to apply both evolution operators to the vacuum state:

$$|\psi\rangle = U_2 U_1 |\text{vac}\rangle = e^{-iH_2} e^{-iH_1} |\text{vac}\rangle \tag{2.50}$$

If we expand each exponential to first order, and apply this evolution operator to the vacuum state, we get:

$$|\psi\rangle \sim \left[1 - i\lambda_2 \hat{a}_0 \hat{a}_2^\dagger \hat{a}_3^\dagger + H.c.\right] \left[1 - i\alpha\lambda_1 \hat{a}_0^\dagger \hat{a}_1^\dagger + H.c.\right] |\text{vac}\rangle \tag{2.51}$$

Expanding and ignoring vacuum terms yields:

$$|\psi\rangle \sim -i\alpha\lambda_1 |1_{\omega_0}, 1_{\omega_1}, 0_{\omega_2}, 0_{\omega_3}\rangle - \alpha\lambda_1\lambda_2 |0_{\omega_0}, 1_{\omega_1}, 1_{\omega_2}, 1_{\omega_3}\rangle. \tag{2.52}$$

The second term making up this state corresponds to three photons being produced at frequencies $\omega_1$, $\omega_2$ and $\omega_3$. We also see that this portion of the state amplitude is linearly related to the pump field strength, so we expect the probability of detecting photon triplets to scale linearly with the intensity of the pump. Just like with two-photon polarization entanglement from SPDC, we can produce three-photon entanglement from cascaded SPDC by interfering two processes producing orthogonally polarized photon triplets. This is shown in Chapter 4.

## 2.5 Phasematching, quasi-phasematching and periodic poling

As we mentioned in Section 2.3, to get appreciable signal from downconversion, the phasematching condition, $k_p \approx k_s + k_i$, needs to be fulfilled. Since most materials are dispersive, this condition is usually not met on its own. Several methods exist to compensate for this dispersion to allow for phasematching [72].

One solution is to use a birefringent material in combination with either temperature or angle tuning. However, this is not always possible; some materials do not have sufficient birefringence, while others are not birefringent at all. Moreover, in many materials there is a strong nonlinearity between fields all polarized in the same direction[6], in which case birefringence is not helpful. Birefringent phasematching also causes problems with

---

[6] This would be the nonlinear coefficient $d_{33} = \frac{1}{2}\chi^{(2)}_{zzz}$

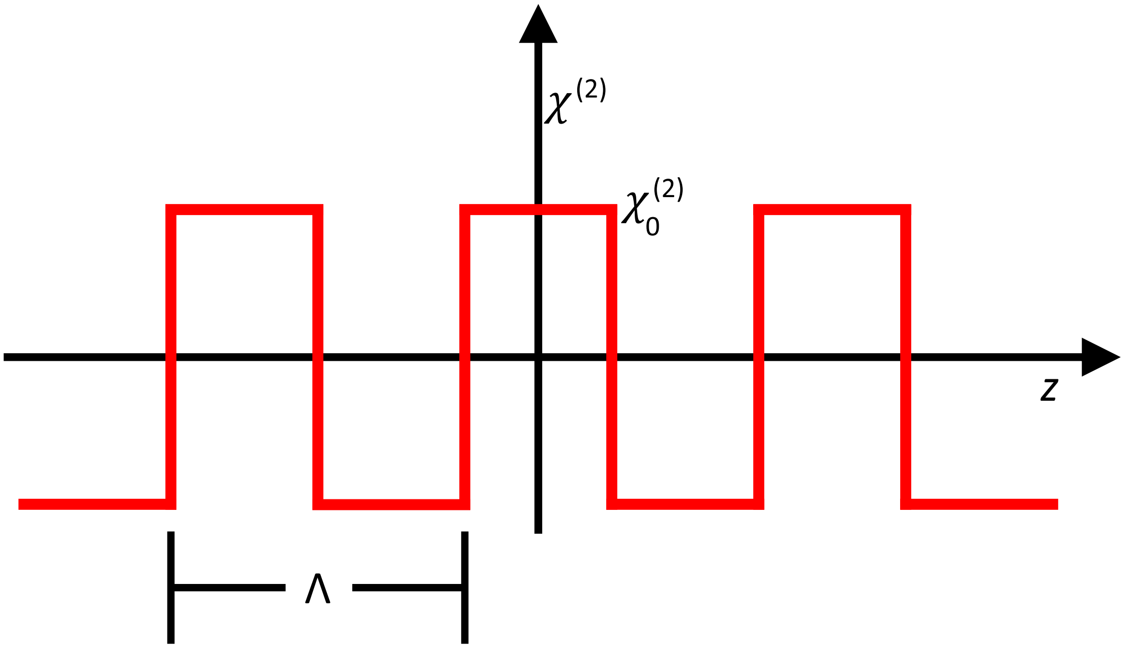

Figure 2.2: Effective nonlinear coefficient in a periodic material. The nonlinear coefficient can be written as a step function, which goes from $\chi_0^{(2)}$ to $-\chi_0^{(2)}$, with a period of $\Lambda$. This figure and its caption were originally published in my MSc thesis [31].

long crystals, because the orientation of the crystal is defined by the phasematching condition. This means that pump and downconversion beams are not oriented along one of the crystallographic axes, leading to spatial walk-off.

In these cases, quasi-phasematching can be used instead. First proposed by Armstrong [73], the basic idea of quasi-phasematching is to periodically reverse the direction of the nonlinear material. This is shown in Figure 2.2. This modulation of the nonlinear coefficient modifies the phasematching condition of Equation 2.47. To see this, can start by writing the nonlinear coefficient as:

$$\chi^{(2)}(z) = \chi_0^{(2)} \operatorname{sgn}\left(\cos\frac{2\pi z}{\Lambda}\right). \tag{2.53}$$

Here $\chi_0^{(2)}$ is the second order nonlinear response coefficient, $z$ is the position in the direction of propagation of the beam, and sgn, the sign function, returns 1 for positive arguments and -1 for negative arguments. By expanding this equation as a Fourier series, it is easy to show that it can be rewritten as:

$$\chi^{(2)} = \sum_{m=-\infty}^{\infty} \frac{2\chi_0^{(2)}}{\pi m} \sin\left(\frac{m\pi}{2}\right) e^{i\frac{2\pi m}{\Lambda}z}. \tag{2.54}$$

By substituting this form of $\chi^{(2)}$ into Equation 2.35, the additional factor of $e^{i\frac{2\pi m}{\Lambda}z}$ results in a modified phasematching condition [31]:

$$k_p = k_s + k_i - \frac{2\pi m}{\Lambda}. \tag{2.55}$$

where $m$ is an integer giving the quasi-phasematching order. We are usually interested in first order phasematching, so the phasematching condition becomes:

$$k_p = k_s + k_i + \frac{2\pi}{\Lambda}. \tag{2.56}$$

To achieve the reversal of the nonlinear coefficient in the material, a technique called periodic poling is used [74]. Electrodes are applied at regular intervals on a ferroelectric nonlinear crystal as shown in Figure 2.3. A high voltage is then applied to the material as it is heated. This produces a reversal of the domains in the material's lattice, providing the required inversion of the nonlinear coefficient.

In the experiments described in this thesis, two materials are used to produce downconversion. The first is called periodically poled potassium tytanyl phosphate, or PPKTP. It is commonly used for second harmonic generation to produce light in the blue to near ultra-violet region [75]. We employ it to produce downconversion of a 404 nm pump to 776 nm and 842 nm. The second material is periodically poled lithium niobate, or PPLN, another widely used nonlinear material [75]. We utilize it for downconversion with a pump at 776 nm, producing photons at 1530 nm and 1570 nm.

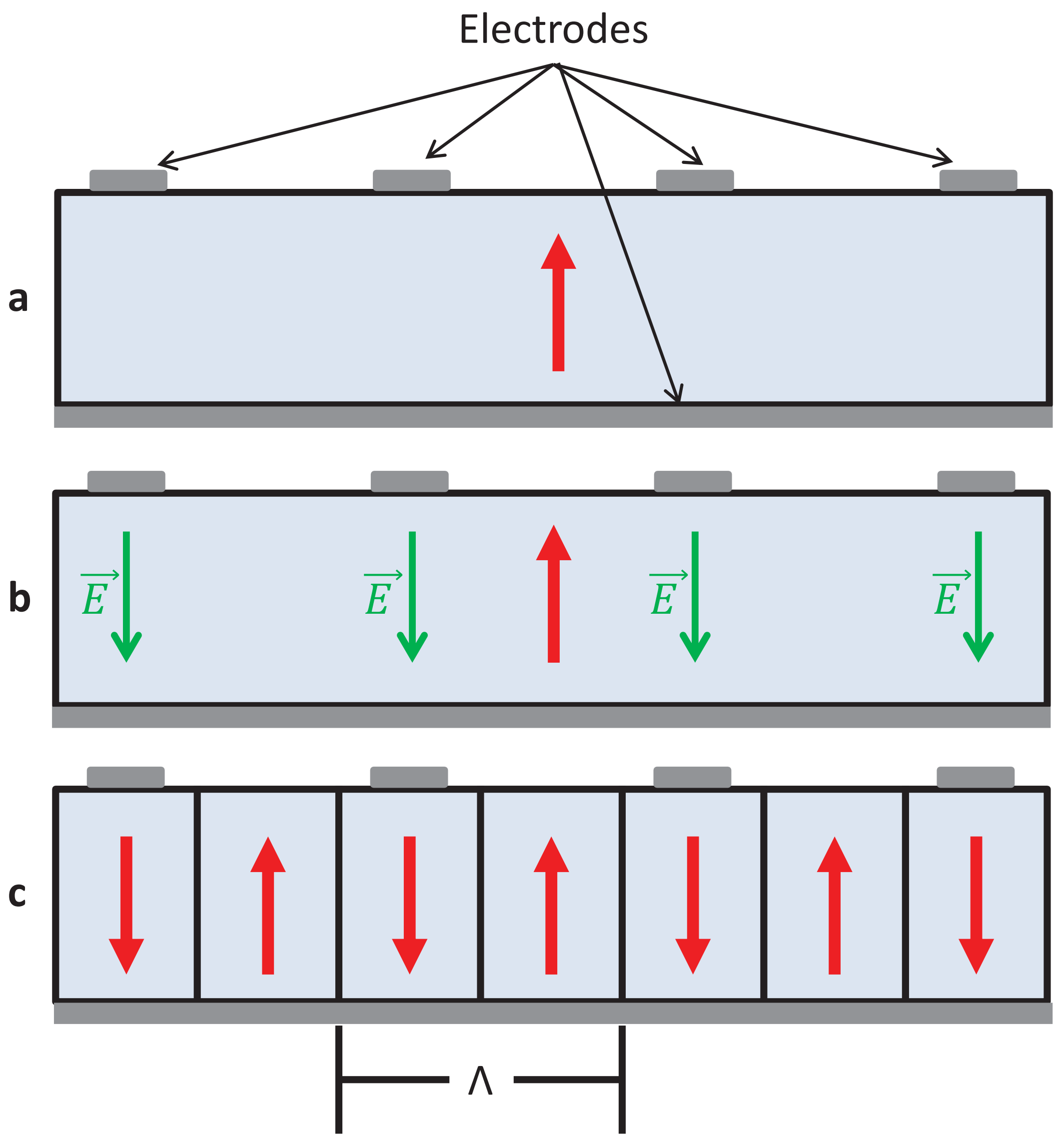

Figure 2.3: Sketch of the periodic poling method. **a**, In the beginning, all the domains point in the same direction indicated by the red arrow. **b**, An electric field is then applied in the opposite direction, inverting the domains in the affected regions. **c**, We are left with the desired periodic material. This figure and its caption were originally published in my MSc thesis [31].

# Chapter 3

# Three-photon energy-time entanglement

## 3.1 Notes and acknowledgements

In this chapter we describe the experimental demonstration of genuine tripartite energy-time entanglement of photon triplets produced by cascaded downconversion. This was the first proof that cascaded downconversion can produce photons which are entangled.

**Notice**: The content of this chapter has been published in:

Lynden K. Shalm, Deny R. Hamel, Zhizhong Yan, Christoph Simon, Kevin J. Resch and Thomas Jennewein, Three-photon energytime entanglement. *Nature Physics*, 9:19-22, 2012.

**Author contributions**

**Lynden K. Shalm** and **Deny R. Hamel** carried out the experiment,

**Christoph Simon**, **Kevin J. Resch** and **Thomas Jennewein** conceived the experiment,

**Zhizhong Yan** developed the detectors and electronics used in the experiment,

**Lynden K. Shalm**, **Deny R. Hamel**, **Kevin J. Resch** and **Thomas Jennewein** analysed the data,

**All authors** contributed to the writing of the manuscript.

## 3.2 Uncertainly relations and multipartite entanglement

Entangled quantum particles have correlations stronger than those allowed by classical physics. These correlations are at the heart of deep foundational questions in quantum mechanics,[11, 12, 17] and form the basis of many emerging quantum technologies [2, 5, 76, 6, 7, 8]. While the discrete variables of up to 14 ions [77] and the continuous variables between three intense optical beams [78, 79] have been entangled, it has remained an open challenge to entangle the continuous properties of three or more individual particles. Here we experimentally demonstrate genuine tripartite continuous-variable entanglement between three separated particles. In our setup the three particles are photons created directly from a single input photon; the creation process leads to quantum correlations between the energies and emission times of the photons. The entanglement between our photons is the three-party generalization of the Einstein-Podolsky-Rosen (EPR)[11] correlations for continuous variables, and could serve as a valuable resource in a wide variety of quantum information tasks.

We directly generate three entangled photons using the nonlinear process of cascaded spontaneous parametric downconversion (C-SPDC)[56]. In downconversion, a pump photon, with frequency $\omega_p$, inside a nonlinear material will occasionally fission into a pair of daughter photons with frequencies $\omega_0$ and $\omega_1$. The total energy in the process is conserved [80] with $\hbar\omega_p = \hbar\omega_0 + \hbar\omega_1$. The daughter photons share strong energy and time correlations that are the hallmark of entanglement [81, 82]. The SPDC process is repeated with one of these daughter photons, at $\omega_0$, now serving as the pump, creating a pair of granddaughter photons simultaneously at $\omega_2$ and $\omega_3$. Again energy is conserved, and the total energy of the the three photons created in C-SPDC must sum to the energy of the pump: $\hbar\omega_p = \hbar\omega_1 + \hbar\omega_2 + \hbar\omega_3$. The simplified representation of our three-photon state in frequency space, assuming a monochromatic pump, has the form

$$\Psi_{CSPDC} \approx \int_{\omega_1}\int_{\omega_2} d\omega_1 d\omega_2 G_1(\omega_1,\omega_p-\omega_1)G_2(\omega_2,\omega_p-\omega_1-\omega_2)a_1^\dagger(\omega_1)a_2^\dagger(\omega_2)a_3^\dagger(\omega_p-\omega_1-\omega_2)\left|0\right\rangle, \tag{3.1}$$

where $G_1(\omega_1, \omega_p - \omega_1)$ and $G_2(\omega_2, \omega_p - \omega_1 - \omega_2)$ are the joint-spectral functions resulting from the phasematching conditions of the first and second SPDC crystals respectively [49]. The three photons, consequently, share strong spectral correlations and exhibit genuine tripartite energy-time entanglement.

To verify the tripartite entanglement of the photons generated in our C-SPDC process we use continuous variable entanglement criteria, that we derive based on the work of van Loock and Furusawa [65], for position and momentum. Consider three separable particles each described by the dimensionless observables $x_k$, $p_k$ ($k = 1, 2, 3$) fulfilling the commutation relations $[x_k, p_l] = i\delta_{kl}$ (note: van Loock and Furusawa [65] use a different commutation relation than the one used here). Each individual particle must satisfy the uncertainty relationship $\Delta x_i \Delta p_i \geq 1/2$. Together, all three particles must satisfy the following position-momentum uncertainty inequalities (see Supplementary Information for details):

$$\Delta(x_2 - x_1)\Delta(p_1 + p_2 + p_3) \geq 1, \tag{3.2}$$

$$\Delta(x_3 - x_2)\Delta(p_1 + p_2 + p_3) \geq 1, \tag{3.3}$$

$$\Delta(x_3 - x_1)\Delta(p_1 + p_2 + p_3) \geq 1. \tag{3.4}$$

Violating any one of these inequalities is sufficient to demonstrate that a state contains some entanglement. Violating any two inequalities demonstrates that the state is fully inseparable [57]. For pure states full inseparability implies genuine tripartite entanglement [58]. However, full inseparability and genuine tripartite entanglement are not, in general, the same thing. Mixtures of bipartite entangled states that are fully inseparable but not genuinely tripartite entangled are also capable of violating two of the above inequalities. A more general entanglement criterion is therefore required to detect genuine tripartite entanglement. In the Supplementary Information we provide an overview of the definitions of full inseparability and genuine tripartite entanglement and derive the following inequalities:

$$
\begin{aligned}
\left[\Delta(x_2 - x_1) + \Delta(x_3 - x_1)\right] \Delta(p_1 + p_2 + p_3) &\geq 1. &(3.5)\\
\left[\Delta(x_2 - x_1) + \Delta(x_3 - x_2)\right] \Delta(p_1 + p_2 + p_3) &\geq 1, &(3.6)\\
\left[\Delta(x_3 - x_2) + \Delta(x_3 - x_1)\right] \Delta(p_1 + p_2 + p_3) &\geq 1, &(3.7)\\
\left[\Delta(x_2 - x_1) + \Delta(x_3 - x_1) + \Delta(x_3 - x_2)\right] \Delta(p_1 + p_2 + p_3) &\geq 2. &(3.8)
\end{aligned}
$$

Violating any one of them is sufficient to demonstrate genuine tripartite entanglement.

The position and momentum operators $x$ and $p$ are well-defined for narrow-band photons [83], such as those generated by our C-SPDC process, with the usual commutation relation $[x, p] = i$. Because photons propagate at the speed of light, $c$, measuring the arrival time, $t$, of a photon at a single-photon detector is equivalent to measuring its longitudinal position $x$ ($t = x/c$), and measuring its frequency, $\omega$, is equivalent to measuring its longitudinal momentum $p$ ($\hbar\omega = cp$). Using this correspondence it is possible to write down the energy-time equivalents to the inequalities in equations 3.5-3.8:

$$
\begin{aligned}
\left[\Delta(t_2 - t_1) + \Delta(t_3 - t_1)\right] \Delta(\omega_1 + \omega_2 + \omega_3) &\geq 1. &(3.9)\\
\left[\Delta(t_2 - t_1) + \Delta(t_3 - t_2)\right] \Delta(\omega_1 + \omega_2 + \omega_3) &\geq 1, &(3.10)\\
\left[\Delta(t_3 - t_2) + \Delta(t_3 - t_1)\right] \Delta(\omega_1 + \omega_2 + \omega_3) &\geq 1, &(3.11)\\
\left[\Delta(t_2 - t_1) + \Delta(t_3 - t_1) + \Delta(t_3 - t_2)\right] \Delta(\omega_1 + \omega_2 + \omega_3) &\geq 2. &(3.12)
\end{aligned}
$$

States of the form in Equation 3.1 can violate all the inequalities maximally, ie the left-hand side goes to zero, and thus exhibit genuine tripartite entanglement.

Measuring the difference in arrival times of the three photons using fast single-photon detectors gives the required timing uncertainties for testing the inequalities. However, directly measuring the frequencies of each individual photon with the precision needed (sub-GHz resolution over a bandwidth of several THz) to violate the inequalities is infeasible with current count rates. Instead we rely on the fact that energy is conserved in the process of downconversion. The energy of the pump is equal to the energy of the three daughter photons created in C-SPDC ($\hbar\omega_p = \hbar\omega_1 + \hbar\omega_2 + \hbar\omega_3$); measuring the frequency of the pump provides a direct measurement of the total frequency, of the three daughter photons required by the inequalities. We experimentally verify that energy is conserved in downconverion in our high-efficiency PPLN waveguide, the central component of our experiment, using an unbalanced interferometer (see Supplementary Information for more details). In addition, energy (frequency) conservation in second-order nonlinear processes, like downconversion, has been extensively verified using techniques like Franson interferometry [81, 82], and been measured down to a line width of 200 kHz, an uncertainty much smaller than the scale considered in our experiment, in second-harmonic generation [84, 85] (the time-reversed process of SPDC).

To create our three entangled photons using C-SPDC (see Figure 3.1), first a narrowband pump laser at 404 nm is used to produce a pair of non-degenerate SPDC photons at 776 nm and 842 nm. The photon at 776 nm is then sent through a second SPDC crystal where a pair of granddaughter photons at 1530 nm and 1570 nm are generated (see Methods Summary for more details). This process leaves the 842 nm, 1530 nm and 1570 nm photons entangled in energy and time. Our setup detects an average of 7 triples/hour, from which we can infer the generation of 45 triples/minute accounting for losses due to coupling and detection. In order to obtain sufficient photon counts with small statistical fluctuations, data was collected for a total of 72.6 hours.

The timing information from the detections was analyzed, and the triple coincidence counts binned into a 2D histogram based on $t_2 - t_1$ and $t_3 - t_2$ as shown in Figure 2. From the histogram it is clear that the photon arrivals are tightly correlated in time. The uncertainty in the arrival time between any pair of photons can be found by integrating over the arrival time of the other photon, removing its dependence as shown in Figure 3. From these integrated histograms we find that $\Delta(t_2 - t_1) = 0.37 \pm 0.02$ ns, $\Delta(t_3 - t_2) = 0.162 \pm 0.004$ ns, and $\Delta(t_3 - t_1) = 0.31 \pm 0.02$ ns. Our measurements are limited by the timing jitter in our detectors and the resolution of our time-tagging unit (156 ps). The effect of the jitter can be clearly seen in the elliptical shape of the 2D arrival time histogram—the jitter on the detector used to detect the 842 nm photon is a factor of two larger than the jitter of the two telecom detectors. This is reflected in the uncertainty $\Delta(t_3 - t_2)$ which is approximately a factor of two smaller than either $\Delta(t_2 - t_1)$ or $\Delta(t_3 - t_1)$. Alternatively we can study the two-photon coincidences between detectors D1 & D2 and D2 & D3 independent of the third detector (see Supplementary Information) to verify that integrating over the third photon yields the correct two-photon timing histograms. The need for gating with the 1570 nm detector ($t_3$) prevents the coincidences between $t_3$ and $t_1$ from being analyzed

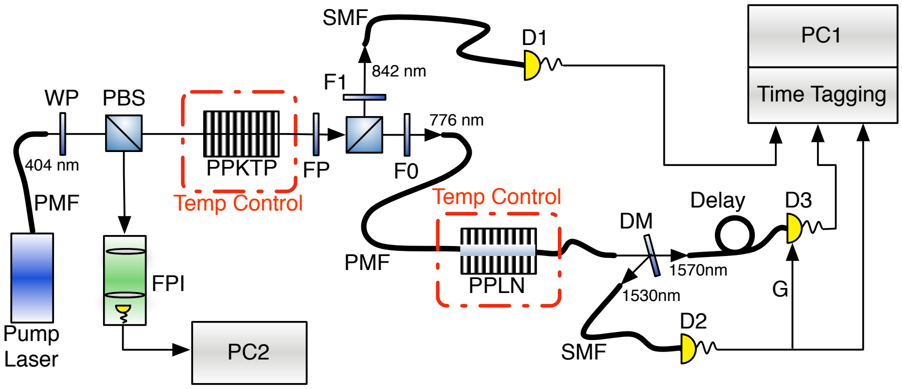

Figure 3.1: Our three entangled photons are created using C-SPDC. A narrowband pump laser at 404 nm downconverts into a pair of orthogonally polarised photons at 842 nm and 776 nm inside a periodically-poled Potassium Titanyl Phosphate (PPKTP) crystal. A filter (FP) removes the remaining pump light. A polarising beamsplitter is used to separate the two photons, and narrowband filters, F0 and F1, are used to block stray light. The photon at 842 nm is coupled into a single-mode fibre and sent to the single-photon detector D1. The photon at 776 nm is coupled into single mode fibre and sent to a periodically-poled Lithium Niobate (PPLN) waveguide where it downconverts into a pair of photons at 1530 nm and 1570 nm. The photons are outcoupled into free space where a dichroic mirror is used to split the photons. The photons are then coupled back into single-mode fibre and sent to single-photon detectors D2 and D3 (see Methods Summary for more information about the detectors). The signals from all three detectors are sent to a time tagging unit, and a computer (PC1) is used to process coincidence events. The spectrum of the 404 nm pump laser is continuously monitored throughout the run using a Fabry-Perot interferometer (FPI) controlled by a second computer (PC2).

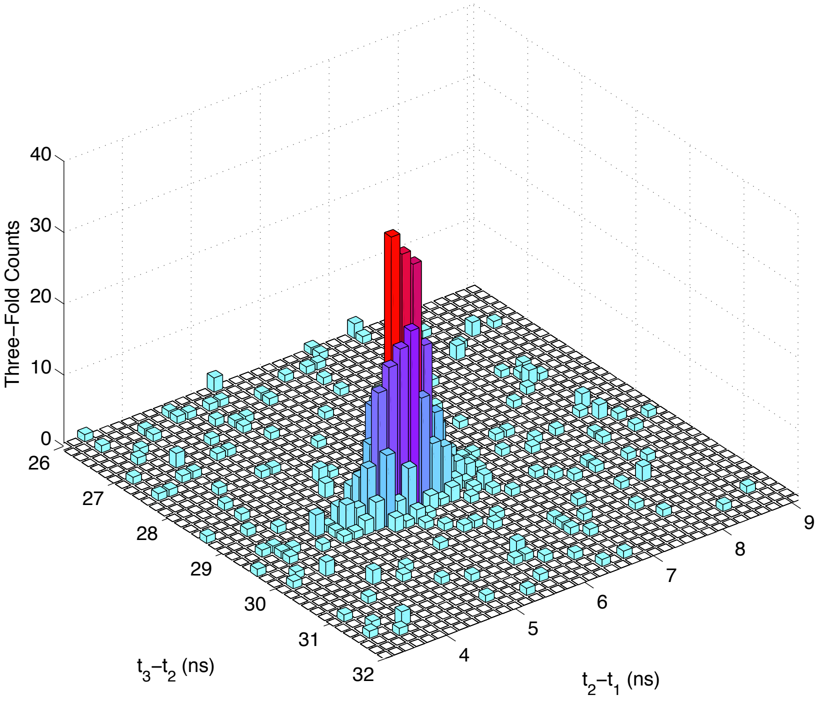

Figure 3.2: 2D histogram of the timing information for the measured triple coincidences over 72.6 hours. The triple events are all localized to a small region of the histogram, indicating strong correlations in the arrival times of the three photons.

independent of $t_2$, but the 50 ns gate width is much larger than the uncertainty in the arrival time of a photon, and approximates the response of a free-running detector.

It is possible for the first downconversion crystal to create two pairs of photons. To prevent two pump photons at 776 nm from reaching detectors D2 and D3 and creating a false triple, a spectral filter is used that blocks the pump light. Additionally, the telecom detectors have a negligible efficiency at the pump wavelength. By tuning the temperature of the PPLN waveguide off of phasematching, we verified that the primary source of accidental triples is due to coincidences with detector darkcounts [56].

Due to energy conservation, the energy uncertainty of the photon triplets is given by the energy uncertainty in the 404 nm pump photons. To measure the uncertainty in the pump

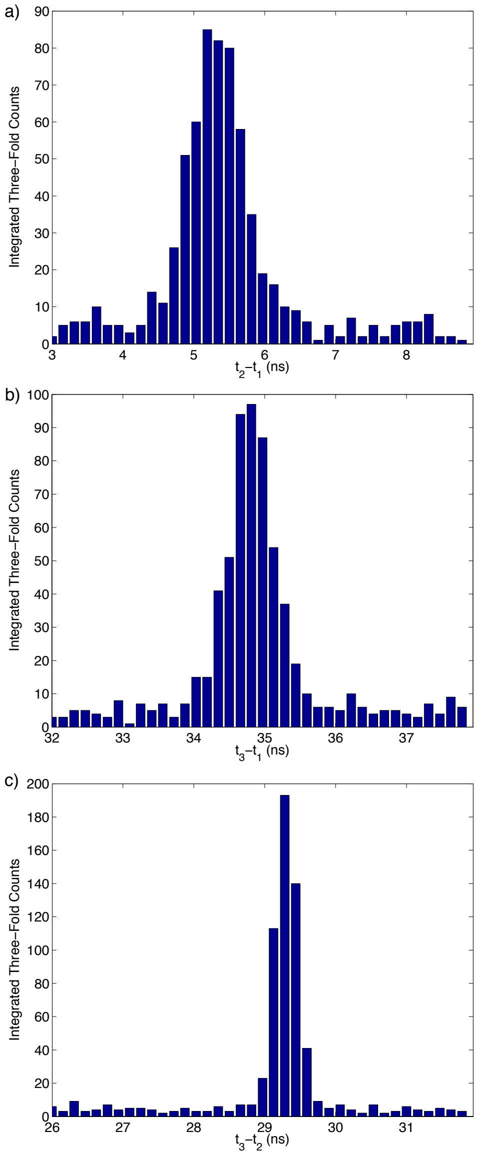

Figure 3.3: Histograms of the difference in arrival times between two of the three photons measured over 72.6 hours. Each histogram is obtained by integrating the triples counts over the arrival time of the third photon to remove its dependence on the results. From this we find the uncertainty in the arrival times of the photons to be a) $\Delta(t_2 - t_1) = 0.37 \pm 0.02$ ns, b) $\Delta(t_3 - t_2) = 0.162 \pm 0.004$ ns, and c) $\Delta(t_3 - t_1) = 0.31 \pm 0.02$ ns. The timing uncertainties were verified using two-fold coincidence data that was obtained at the same time as the three-fold coincidence data (see Supplementary Information).

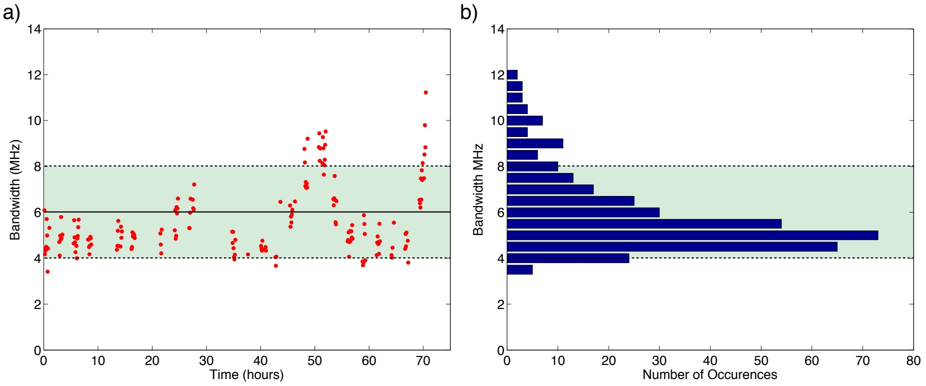

Figure 3.4: Bandwidth of the pump photons as measured by a Fabry-Perot interferometer at five minute intervals during the 72.6 hour run. a) The measured bandwidth as a function of time. The fluctuations in the measured bandwidths are the result of thermal drifts in the apparatus over the course of the run. b) Histogram of the measured pump bandwidths over the duration of the run. The average bandwidth is measured to be $\Delta\omega_p/2\pi$ =6 MHz with a standard deviation of 2 MHz (illustrated by the shaded regions in the graphs).

energy, a scanning Fabry-Perot interferometer (FPI) was used to continuously monitor the bandwidth of the 404 nm laser throughout the experiment. Due to instabilities caused by temperature fluctuations, the measured bandwidth fluctuates over time as shown in Figure 4a, leading to the distribution in Figure 4b. The average value and standard deviation of this distribution yield a pump bandwidth of $\Delta\omega_p/2\pi = (6 \pm 2)$ MHz.

The four measured time-bandwidth products for our three photons are

$$[\Delta(t_2 - t_1) + \Delta(t_3 - t_1)]\,\Delta(\omega_1 + \omega_2 + \omega_3) = 0.03 \pm 0.01, \tag{3.13}$$

$$[\Delta(t_2 - t_1) + \Delta(t_3 - t_2)]\,\Delta(\omega_1 + \omega_2 + \omega_3) = 0.02 \pm 0.01, \tag{3.14}$$

$$[\Delta(t_3 - t_2) + \Delta(t_3 - t_1)]\,\Delta(\omega_1 + \omega_2 + \omega_3) = 0.018 \pm 0.005, \tag{3.15}$$

$$[\Delta(t_2 - t_1) + \Delta(t_3 - t_1) + \Delta(t_3 - t_2)]\,\Delta(\omega_1 + \omega_2 + \omega_3) = 0.03 \pm 0.01. \tag{3.16}$$

Our three photons strongly violate inequalities 3.9-3.12 and are genuinely tripartite entangled. The state exhibits energy-time correlations close to to the ideal state described in Equation 3.1 where the time-bandwidth products are exactly zero. This state is the continuous-variable analogue to the famous Greenberger, Horne and Zeilinger (GHZ) entangled state [63, 65], and the natural extension of the two-party continuous-variable EPR state [81, 82, 86]. The limiting factor in our measurements is the several hundred picosecond timing jitter of our detectors. Based on the bandwidth of our downconverted photons, the arrival times of the three photons should have a fundamental uncertainty on the order of a picosecond. With the development of faster detectors we should be able to lower our measured values of the inequalities, which are already close to ideal, by over two orders of magnitude.

Recent improvements in telecom wavelength detectors [87] and advances in nonlinear materials promise to dramatically increase our detected triples rate [46, 88]. Furthermore, new techniques to enhance the strength of nonlinear effects [50, 89] means that our scheme can in principle be scaled up to larger photon numbers. A major advantage of our states is that the continuous-variable entanglement is distributed amongst three individual photons, each at a different, tunable, wavelength, enabling the creation of hyper-entangled states that simultaneously take advantage of both discrete and continuous variable quantum correlations. This multiplexing of entanglement over multiple discrete and continuous degrees of freedom may have important applications in quantum communication tasks. For example, a slight modification to our setup would enable a photon at 776 nm to be interfaced with an atomic storage medium like Rb while the remaining two photons are transmitted over telecom fibres to remote quantum nodes. This would open up new possibilities in the storage and distribution of quantum information needed for quantum computing, cryptography, and secret sharing, and could lead to new fundamental tests of quantum mechanics.

## 3.3 Methods Summary

In our setup (shown if Figure 1) we use a grating-stabilized pump laser with a wavelength of 404 nm and a bandwidth of 5 MHz (Toptica Bluemode) to pump a 30 mm PPKTP crystal phase matched for Type-II SPDC. A pair of orthogonally polarised signal and idler photons at 842 nm and 776 nm respectively are generated co-linearly, and a polarising beam splitter (PBS) is used to separate them. The signal photon at 842 nm is coupled into an optical fibre and sent to a Si single-photon detector. With 12 mW of pump power $10^6$ signal photons/s are detected. The idler photon is fibre-coupled and sent to a second SPDC crystal, a 30 mm Type-I phase matched PPLN waveguide (HC Photonics), where it fissions into a pair of granddaughter photons at 1570 nm and 1530 nm. These granddaughter photons are outcoupled into free space and then split using a dichroic mirror. The photon at 1530 nm is sent to a free-running InGaAs/InP-Avalanche Photo Diodes (Princeton Lightwave, Negative Feedback Avalanche Diode - NFAD) detector cooled to 193 K operating at 10% efficiency with approximately 100 dark counts/s. This detector is used to gate a second InGaAs/InP detector (iD Quantique, id201-SMF-ULN) operating at 25% detection efficiency with a 50 ns gate window to detect the granddaughter photon at 1570 nm. The gated detector had a much higher dark count rate of approximately $5 \times 10^{-5}$ dark counts/(ns of gate). The arrival times of each of photons in the three detectors are recorded by a time-tagging system (DotFast/UQDevices) with 156 ps resolution. In this way all the timing statistics from the two-fold and three-fold coincidence events generated by the C-SPDC process can be measured.

## 3.4 Genuine tripartite entanglement

### 3.4.1 Fully inseparable versus genuine tripartite entanglement

There are two definitions that have been introduced for describing three-particle entanglement: *fully inseparable* [57] and *genuine tripartite entanglement* [58]. While these terms are sometimes used interchangeably in the literature, they mean different things. In [57] a classification scheme for three particle entanglement was developed based on the following set of tripartite states:

$$\rho = \sum_i \eta_i \rho_{1,2,i} \otimes \rho_{3,i}, \tag{3.17}$$

$$\rho = \sum_i \eta_i \rho_{1,3,i} \otimes \rho_{2,i}, \tag{3.18}$$

$$\rho = \sum_i \eta_i \rho_{2,3,i} \otimes \rho_{1,i}, \tag{3.19}$$

$$\rho = \sum_i \eta_i \rho_{1,i} \otimes \rho_{2,i} \otimes \rho_{3,i}. \tag{3.20}$$

The first three states are biseparable as they are factorizable across a single cut while the final state is said to be fully separable as all three particles can be factorized. Tripartite states that cannot be written in *any* of these forms were defined to be fully inseparable [57].

Genuine tripartite entanglement [58] refers to states that cannot be written as a convex sum of just fully separable and biseparable states. In other words, they cannot be written as a convex sum of the states in equations 3.17-3.18. These two definitions are not equivalent. For example, consider the state,

$$\rho = \frac{1}{2}\rho_{12} \otimes \rho_3 + \frac{1}{2}\rho_1 \otimes \rho_{23}. \tag{3.21}$$

This mixed state is not genuine tripartite entangled as it is a convex sum of biseparable states, yet it may be fully inseparable. In section D we present a more explicit example of a state that is fully inseparable but does not contain genuine tripartite entanglement.

In [65] a criterion for detecting tripartite full inseparability in continuous systems is developed. In the following sections we build on this work to derive a stronger criteria capable of detecting genuine tripartite entanglement.

### 3.4.2 Uncertainty relations

Consider three separable particles each described by the dimensionless observables $x_k$, $p_k$ ($k = 1, 2, 3$) fulfilling the commutation relations $[x_k, p_l] = i\delta_{kl}$ (note: the derivation in [65] uses a commutator with a different scaling factor). Each individual particle must satisfy the uncertainty relation $\Delta x_i \Delta p_i \geq 1/2$.

For a general three particle state $\rho = \sum_i \eta_i \rho_{123,i}$, the variance in $\Delta^2(x_1 - x_2)_\rho$ is given as:

$$\begin{aligned}
\Delta^2(x_1 - x_2)_\rho &= \left\langle (x_1 - x_2)^2 \right\rangle_\rho - \langle x_1 - x_2 \rangle_\rho^2 \\
&= \sum_i \eta_i \left\langle (x_1 - x_2)^2 \right\rangle_i - \left( \sum_i \eta_i \langle x_1 - x_2 \rangle_i \right)^2 \\
&= \sum_i \eta_i \left\langle (x_1 - x_2)^2 \right\rangle_i - \left( \sum_i \eta_i \langle x_1 - x_2 \rangle_i \right)^2 + \sum_i \eta_i \langle x_1 - x_2 \rangle_i^2 - \sum_i \eta_i \langle x_1 - x_2 \rangle_i^2 \\
&= \sum_i \eta_i \Delta^2(x_1 - x_2)_i + \sum_i \eta_i \langle x_1 - x_2 \rangle_i^2 - \left( \sum_i \eta_i \langle x_1 - x_2 \rangle_i \right)^2 .
\end{aligned} \tag{3.22}$$

From the Cauchy-Schwarz inequality $\sum_i \eta_i \langle x_1 - x_2 \rangle_i^2 \geq \left( \sum_i \eta_i \langle x_1 - x_2 \rangle_i \right)^2$, therefore the last two terms in equation 3.22 will always be greater than or equal to zero. This leads to the inequality:

$$\Delta^2(x_1 - x_2)_\rho \ \geq \ \sum_i \eta_i \Delta^2(x_1 - x_2)_i. \tag{3.23}$$

This result holds for any sum or difference of operators of this form. The uncertainty in $(x_1 - x_2)$ for the mixed state $\rho$ is greater than or equal to the uncertainties in $(x_1 - x_2)$ of the components of the mixture.

$$\Delta^2(x_1 - x_3)_\rho \ \geq \ \sum_i \eta_i \Delta^2(x_1 - x_3)_i, \tag{3.24}$$

$$\Delta^2(x_2 - x_3)_\rho \ \geq \ \sum_i \eta_i \Delta^2(x_2 - x_3)_i, \tag{3.25}$$

$$\Delta^2(p_1 + p_2 + p_3)_\rho \ \geq \ \sum_i \eta_i \Delta^2(p_1 + p_2 + p_3)_i. \tag{3.26}$$

These results lead to the following position and momentum inequality:

$$\Delta^2(x_1 - x_2)\Delta^2(p_1 + p_2 + p_3) \geq \left( \sum_i \eta_i \Delta^2(x_1 - x_2)_i \right) \left( \sum_j \eta_j \Delta^2(p_1 + p_2 + p_3)_j \right). \tag{3.27}$$

Applying the Cauchy-Scharwz inequality to the right hand side of the previous equation yields:

$$\begin{aligned}
\Delta^2(x_1 - x_2)\Delta^2(p_1 + p_2 + p_3) &\geq \left(\sum_i \eta_i \Delta(x_1 - x_2)_i \Delta(p_1 + p_2 + p_3)_i\right)^2, && (3.28)\\
\Delta(x_1 - x_2)\Delta(p_1 + p_2 + p_3) &\geq \sum_i \eta_i \Delta(x_1 - x_2)_i \Delta(p_1 + p_2 + p_3)_i. && (3.29)
\end{aligned}$$

Following the same steps we also find:

$$\begin{aligned}
\Delta(x_2 - x_3)\Delta(p_1 + p_2 + p_3) &\geq \sum_i \eta_i \Delta(x_2 - x_3)_i \Delta(p_1 + p_2 + p_3)_i, && (3.30)\\
\Delta(x_1 - x_3)\Delta(p_1 + p_2 + p_3) &\geq \sum_i \eta_i \Delta(x_1 - x_3)_i \Delta(p_1 + p_2 + p_3)_i. && (3.31)
\end{aligned}$$

### 3.4.3 Uncertainty relations for detecting continuous variable genuine tripartite entanglement

In [65] van Loock and Furusawa study the permutations of a particular class of three-particle states defined as:

$$\rho = \sum_i \eta_i \rho_{i,12} \otimes \rho_{i,3}, \tag{3.32}$$

where particles 1 and 2 can be entangled with one another, but are separable from particle 3, and derive a set of inequalities:

$$\begin{aligned}
[\Delta(x_1 - x_2)]^2 + [\Delta(p_1 + p_2 + p_3)]^2 &\geq 2, && (3.33)\\
[\Delta(x_2 - x_3)]^2 + [\Delta(p_1 + p_2 + p_3)]^2 &\geq 2, && (3.34)\\
[\Delta(x_1 - x_3)]^2 + [\Delta(p_1 + p_2 + p_3)]^2 &\geq 2. && (3.35)
\end{aligned}$$

It is important to note that in [65] a different scaling factor for the commutator is used which leads to the right-hand side of these inequalities having a value of one instead of two in that work.

As the derivation of inequalities 3.33-3.35 depends only on the form of the commutator, they also hold for rescaled variables $x'_k = sx_k$, $p'_k = p_k/s$ for any scaling factor $s$. Minimizing the expressions on the left of the inequalities with respect to the scaling factor $s$ yields the following product inequalities:

$$\Delta(x_1 - x_2)\Delta(p_1 + p_2 + p_3) \geq 1, \tag{3.36}$$

$$\Delta(x_2 - x_3)\Delta(p_1 + p_2 + p_3) \geq 1, \tag{3.37}$$

$$\Delta(x_1 - x_3)\Delta(p_1 + p_2 + p_3) \geq 1. \tag{3.38}$$

States that simultaneously violate any two of these inequalities are fully inseparable. Now consider the following $\rho$ that is a mixture of all possible biseparable and fully separable states.

$$\rho = \sum_i \eta_i \rho_{i,12} \otimes \rho_{i,3} + \sum_j \mu_j \rho_{j,13} \otimes \rho_{j,2} + \sum_k \gamma_k \rho_{k,23} \otimes \rho_{k,1} + \sum_l \nu_l \rho_{l,1} \otimes \rho_{l,2} \otimes \rho_{l,3}, \tag{3.39}$$

where $\eta_i$, $\mu_j$, $\gamma_k$, and $\nu_l$ are probabilities with $\sum_i \eta_i + \sum_j \mu_j + \sum_k \gamma_k + \sum_l \nu_l = 1$. With the correct choice of parameters it is possible for $\rho$ to violate two of the van Loock and Furusawa inequalities simultaneously despite not containing *any* genuine tripartite entanglement (an explicit example is given in section 3.4.4). A more stringent test is needed to look for genuine tripartite entanglement.

Using the results from inequalities 3.29-3.31 we find that:

$$\begin{aligned} \Delta(x_1 - x_2)\Delta(p_1 + p_2 + p_3) \geq & \sum_i \eta_i \Delta(x_1 - x_2)_i \Delta(p_1 + p_2 + p_3)_i + \\ & \sum_j \mu_j \Delta(x_1 - x_2)_j \Delta(p_1 + p_2 + p_3)_j + \\ & \sum_k \gamma_k \Delta(x_1 - x_2)_k \Delta(p_1 + p_2 + p_3)_k + \\ & \sum_l \nu_l \Delta(x_1 - x_2)_l \Delta(p_1 + p_2 + p_3)_l. \end{aligned} \tag{3.40}$$

If the component of the state $\rho_{i,12}$ is entangled across particles 1 and 2, then the lowest possible value of $\Delta(x_1 - x_2)_i \Delta(p_1 + p_2 + p_3)_i$ is zero. The remaining three terms are for cases where particles 1 and 2 are on opposite sides of a separable cut; from equation 3.2 the minimum value of the uncertainty products are $\Delta(x_1-x_2)_j\Delta(p_1+p_2+p_3)_j = \Delta(x_1-x_2)_k\Delta(p_1+p_2+p_3)_k = \Delta(x_1-x_2)_l\Delta(p_1+p_2+p_3)_l = 1$. The uncertainty product in equation 3.40 can then be written as:

$$\begin{aligned}\Delta(x_1-x_2)\Delta(p_1+p_2+p_3) &\geq \sum_i \eta_i(0) + \left(\sum_j \mu_j + \sum_k \gamma_k + \sum_l \nu_l\right)(1),\\ &\geq \sum_j \mu_j + \sum_k \gamma_k + \sum_l \nu_l. \qquad (3.41)\end{aligned}$$

Following the same arguments it is possible to show that:

$$\Delta(x_1-x_3)\Delta(p_1+p_2+p_3) \geq \sum_i \eta_i + \sum_k \gamma_k + \sum_l \nu_l. \qquad (3.42)$$

$$\Delta(x_2-x_3)\Delta(p_1+p_2+p_3) \geq \sum_i \eta_i + \sum_j \mu_j + \sum_l \nu_l. \qquad (3.43)$$

Adding inequalities 3.41 and 3.42 yields the sum inequality:

$$\begin{aligned}\left[\Delta(x_1-x_2)+\Delta(x_1-x_3)\right]\Delta(p_1+p_2+p_3) &\geq \qquad (3.44)\\ \sum_i \eta_i &+ \sum_j \mu_j + 2\left(\sum_k \gamma_k + \sum_l \nu_l\right).\end{aligned}$$

The right-hand side is minimized by setting $\sum_k \gamma_k = \sum_l \nu_l = 0$ giving:

$$\left[\Delta(x_1-x_2)+\Delta(x_1-x_3)\right]\Delta(p_1+p_2+p_3) \geq 1. \qquad (3.45)$$

Similarly we find:

$$\left[\Delta(x_1-x_2)+\Delta(x_2-x_3)\right]\Delta(p_1+p_2+p_3) \geq 1, \qquad (3.46)$$

$$\left[\Delta(x_2-x_3)+\Delta(x_1-x_3)\right]\Delta(p_1+p_2+p_3) \geq 1. \qquad (3.47)$$

Violating any of these sum inequalities 3.45-3.47 indicates that the state cannot be written with at most biseparable terms, and thus must be genuine tripartite entangled.

It is also possible to add the three inequalities 3.41-3.43 together:

$$\begin{aligned}\left[\Delta(x_1-x_2)+\Delta(x_1-x_3)+\Delta(x_2-x_3)\right]\Delta(p_1+p_2+p_3) &\geq \qquad (3.48)\\ 2\left(\sum_i \eta_i + \sum_j \mu_j + \sum_k \gamma_k\right) &+ 3\left(\sum_l \nu_l\right),\end{aligned}$$

which is minimized when $\sum_l \nu_l = 0$ leading to:

$$[\Delta(x_1 - x_2) + \Delta(x_1 - x_3) + \Delta(x_2 - x_3)]\,\Delta(p_1 + p_2 + p_3) \;\;\geq\;\; 2. \tag{3.49}$$

Violating this inequality also demonstrate the presence of genuine tripartite entanglement.

### 3.4.4 Example states

Consider the following three states of three different particles written in the position basis:

$$\psi_1(x_1, x_2, x_3) \;=\; \frac{1}{N_1} e^{-\left(\frac{x_1}{2\sigma_1}\right)^2} e^{-\left(\frac{x_2}{2\sigma_2}\right)^2} e^{-\left(\frac{x_3}{2\sigma_3}\right)^2} e^{-\left(\frac{x_1 - x_2}{2\sigma_c}\right)^2}, \tag{3.50}$$

$$\psi_2(x_1, x_2, x_3) \;=\; \frac{1}{N_2} e^{-\left(\frac{x_1}{2\sigma_4}\right)^2} e^{-\left(\frac{x_2}{2\sigma_5}\right)^2} e^{-\left(\frac{x_3}{2\sigma_6}\right)^2} e^{-\left(\frac{x_1 - x_3}{2\sigma_c}\right)^2}, \tag{3.51}$$

$$\psi_3(x_1, x_2, x_3) \;=\; \frac{1}{N_3} e^{-\left(\frac{x_1}{2\sigma_7}\right)^2} e^{-\left(\frac{x_2}{2\sigma_8}\right)^2} e^{-\left(\frac{x_3}{2\sigma_9}\right)^2} e^{-\left(\frac{x_2 - x_3}{2\sigma_c}\right)^2}, \tag{3.52}$$

where $N_1$, $N_2$, and $N_3$ are normalization constants and $\sigma_1$ through $\sigma_6$ are adjustable width parameters. The width $\sigma_c$ represents a correlation length for each of the states. When $\sigma_c \to 0$ two of the particles in each of the states become perfectly entangled with one another. The lower bound of the derived uncertainty relations 3.45-3.49 are saturated by pure states of the form shown in equations 3.50-3.52, and are therefore tight.

In general, full inseparability does not imply genuine tripartite entanglement. Consider the fully inseparable state composed of an equal mixture of $\psi_1$ and $\psi_2$ with $\sigma_c = 0$, $\sigma_{2,3,5,6} = 1$, and $\sigma_{1,4} \to \infty$. This mixed state, despite containing no component of genuine tripartite entanglement, simultaneously violate the van Loock and Furusawa inequalities 3.2 and 3.4. However, when tested against the new inequality derived in 3.5, it reaches a minimum value of $\sqrt{2} > 1$; our inequality is able to discern that this state contains no genuine tripartite entanglement. A similar fully inseparable mixed state, composed of an equal mixture of $\psi_1$, $\psi_2$, and $\psi_3$ with $\sigma_c = 0$, $\sigma_{1,2,4,6,8,9} = 1$, and $\sigma_{3,5,7} = 1/\sqrt{2}$, is capable of simultaneously violating *all three* of the van Loock and Furusawa inequalities despite not being genuinely tripartite entangled. When tested against the new inequality 3.49 it reaches a value of $\sqrt{6} > 2$, demonstrating that it is not genuinely tripartite entangled.

In the specific case of pure states, full inseparability implies genuine tripartite entanglement. With the assumption of purity, both the van Loock and Furusawa inequalities as well as the ones derived here are capable of detecting genuine tripartite entanglement. For example, the pure state

$$\psi_4(x_1,x_2,x_3) \;=\; \frac{1}{N_4} e^{-\left(\frac{x_1}{2\sigma_1}\right)^2} e^{-\left(\frac{x_2}{2\sigma_2}\right)^2} e^{-\left(\frac{x_3}{2\sigma_3}\right)^2} e^{-\left(\frac{x_1-x_2}{2\sigma_c}\right)^2} e^{-\left(\frac{x_1-x_3}{2\sigma_c}\right)^2}, \tag{3.53}$$

where $N_4$ is a normalization constant, exhibits perfect correlations between particles 1-3 when $\sigma_c \to 0$ (for finite widths $\sigma_{1,2,3}$), and is both fully inseparable and genuinely tripartite entangled. This pure state will violate the van Loock and Furusawa inequalities as well as the inequalities 3.45-3.47 and 3.49. It is only in the more general case of mixed states that the relations derived by van Loock and Furusawa need to be extended in order to detect genuine tripartite entanglement.

## 3.5 Alternate measurement of the photon timing uncertainty

To verify that integrating over the third photon yields the correct two-photon timing histograms, the raw two-photon coincidence data from the measured time tags between photons 1 and 2 as well as the coincidences between photons 2 and 3 were analyzed independently of detecting the other photon. While the timing uncertainty between two detectors are conditioned on the presence of a third photon, this measurement of the arrival times (shown in Figure 3.5) is different in that it is conditioned only on two photons. From this data, it was found that $\Delta(t_2-t_1) = 0.4 \pm 0.2$ ns and $\Delta(t_3-t_2) = 0.16 \pm 0.04$ ns, which agree with the integrated values measured in the paper. The reason for the larger error is due to the large number of accidental counts. In the histogram between $t_2 - t_1$ the large background is caused by the coincidences between dark counts on the free-running InGaAs/InP detector [90] and the $10^6$ trigger photons per second on the Si detector. The number of dark counts, and hence signal-to-noise ratio, is lower in the $t_3 - t_2$ histogram; here the background is primarily due to accidental coincidences between dark counts between the two telecom detectors. As the first telecom detector $t_2$ gated the second telecom detector $t_3$, our setup did not allow us to measure the two-fold coincidence histogram $t_3 - t_1$ independent of photon 2.

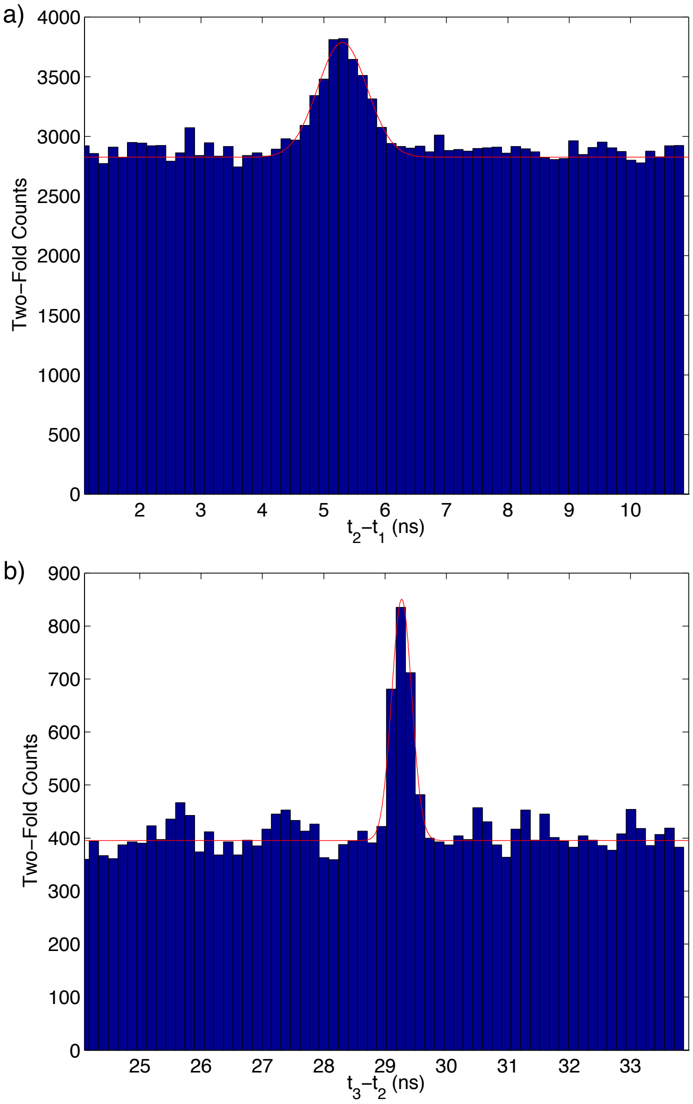

Figure 3.5: Histograms of the arrival times between a) photons 1 and 2 and b) photons 2 and 3. This was accomplished by examining the two-fold coincidences, as opposed to the three-fold coincidences, from the collected time tags. From these histograms an uncertainty in the difference between the arrival times was found to be $\Delta(t_2 - t_1) = 0.4 \pm 0.2$ ns and $\Delta(t_3 - t_2) = 0.16 \pm 0.04$ ns which agrees with the integrated uncertainties measured in the main paper.

## 3.6 Two photon energy-time entanglement

In a separate experiment we directly measured for 1.6 s the two photon energy-time entanglement between the pair of daughter photons (at 842 nm and 776 nm) created at the first stage of our C-SPDC process as shown in Figure3.6. Both daughter photons were sent to single-photon detectors. The pump power was attenuated so that approximately 14,000 coincidences/s were detected. A time tagging unit was used to store the arrival times of the photons, and a computer then sorted the time tags into extract coincidence events. The histogram of arrival times of the two photons is shown in Figure 3.7, and the uncertainty in the arrival times measured to be $\Delta(t_0 - t_1) = 0.30 \pm 0.01$ ns. Simultaneously the Fabry-Perot interferometer monitored the bandwidth of the pump, yielding a bandwidth of $\Delta\omega_p = 4.6 \pm 0.8$ MHz.

To show bipartite entanglement it is sufficient to violate the two party inequality $\Delta(\omega_0 + \omega_1)\Delta(t_0 - t_1) \geq 1$ [65]. As energy is conserved in SPDC we can use the fact that $\omega_0 + \omega_1 = \omega_p$. This leads to a time-bandwidth product of $\Delta(\omega_0 + \omega_1)\Delta(t_0 - t_1) = 0.0014 \pm 0.0002$ that violates the classical limit by more than 4000 standard deviations.

## 3.7 Energy conservation in SPDC

The conservation of energy in downconversion plays a central role in our experiment; we are able to obtain the energy uncertainty in our daughter photons by directly measuring the energy uncertainty in our pump light. To confirm that energy is indeed conserved in downconversion in our system, we perform two independent experimental tests. The first test is designed to rule out a time-dependent energy loss where the crystal carries away a portion of the pump photon's energy, while the second test allows us to study whether the spectrum of the two downconverted photons is broadened due to energy nonconservation in the crystal. Through our measurements we are able to rule out any significant energy nonconservation that would alter our main results; our three-photon state, presented in the main body of the paper, is genuinely tripartite entangled.

It is important to note that, in addition to our tests, there is a large body of theoretical and experimental work that supports the conservation of energy in downconversion. The

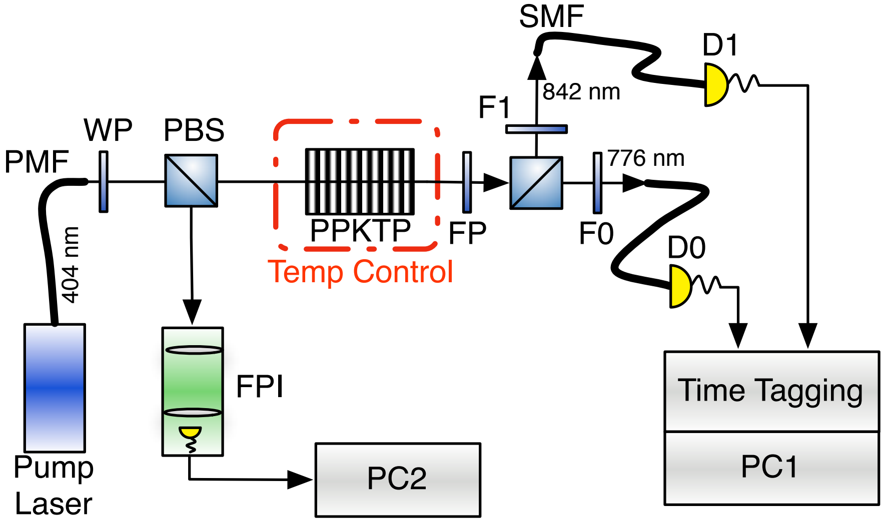

Figure 3.6: Direct measurement of two-photon energy-time entanglement. A narrowband pump laser at 404 nm is used to pump a periodically-poled Potassium Titanyl Phosphate (PPKTP) that downconverts into a pair of orthogonally polarized photons at 842 nm and 776 nm. A filter (FP) removes the remaining pump. A polarizing beamsplitter is used to separate the two photons, and narrowband filters, F0 and F1, are used to minimize stray light. The photons at 842 nm and 776 nm are coupled into single-mode fibres and sent to the single-photon detectors D0 and D1. The signals from both detectors are sent to a time tagging unit, and a computer (PC1) is used to process coincidence events. The spectrum of the 404 nm pump laser is continuously monitored throughout the run using a Fabry-Perot interferometer (FPI) controlled by a second computer (PC2).

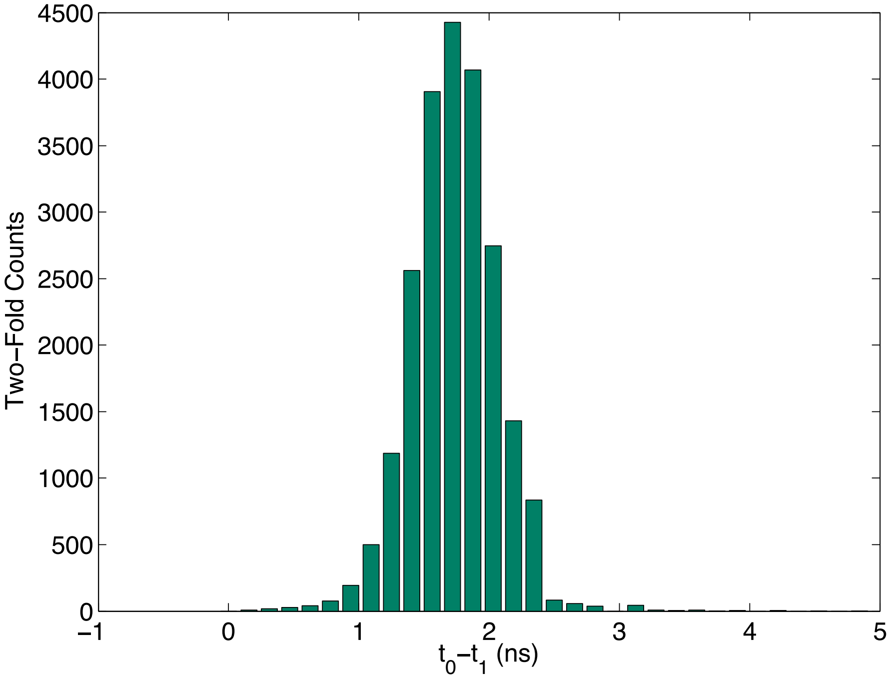

Figure 3.7: Two-photon coincidence histogram of the difference in arrival times of the 842 nm and 776 nm photons from downconversion. From this histogram, the uncertainty in the difference in arrival times was measured to be $\Delta(t_0 - t_1) = 0.30 \pm 0.01$ ns.

theoretical underpinnings of energy conservation in downconversion were first worked out 45 years ago [91]. Since then, many of the experiments, techniques, and technologies in quantum optics based on parametric second-order nonlinear processes rely on the fact that energy is conserved. For example, it is energy conservation that gives rise to the tight energy-time entanglement that exists between daughter photons [81, 82] in downconversion. Also, energy conservation plays a critical role in most squeezing experiments. A local oscillator, usually a portion of the pump light, is interfered with the squeezed light at the detectors. If energy were not conserved then the local oscillator would not remain phase coherent with the squeezed light against which it is beat, and detecting high levels of squeezing would not be possible [92].

### 3.7.1 Time-dependent energy loss

First we consider a downconversion crystal that absorbs a portion of the pump energy $\hbar\zeta$. In this scenario energy is no longer conserved between the pump photon ($\omega_p$) and the signal ($\omega_s$) and idler ($\omega_i$) photons:

$$\omega_p = \omega_s + \omega_i + \zeta, \tag{3.54}$$

where $\Delta$ is the standard deviation. The uncertainty in the pump frequency can then be written as

$$\Delta(\omega_p) = \Delta(\omega_s + \omega_i + \zeta). \tag{3.55}$$

If the energy loss is independent of the signal and idler frequencies, then $\langle \zeta(\omega_s + \omega_i) \rangle = \langle \zeta \rangle \langle (\omega_s + \omega_i) \rangle$ and

$$\Delta^2(\omega_p) = \Delta^2(\omega_s + \omega_i) + \Delta^2(\zeta). \tag{3.56}$$

If the energy loss, $\hbar\zeta$, is constant, then the uncertainty in the pump is equal to the uncertainty in the signal and idler photons. In this case measuring the bandwidth of the pump photons directly gives the bandwidth of the sum of the signal and idler frequencies, and our violation of the genuine tripartite uncertainty relations stands. It is possible that the energy loss is not constant, but rather fluctuates in time. We aim to put an upper bound on $\Delta(\zeta)$ from such fluctuations.

In order to experimentally study the energy mismatch we use a polarizing Mach-Zehnder interferometer (MZI), and place a PPLN waveguides in each arm (see Figure 3.8). One of the PPLN guides was the one used in the experiment in the main paper, and the other is an identically manufactured one from same supplier with the same specifications. This setup is pumped directly with a diode laser at 775 nm which has a narrow line-width of about 1 MHz (Toptica DL-100PRO). The PPLN crystals generate photon pairs at 1530 nm and 1570 nm through SPDC in either the top arm with horizontal polarization, or the lower arm with vertical polarization. The beams are combined in a PBS which leads to perfect two-fold entanglement of the downconverted photons.

To study the quantum state generated by the MZI, we will first consider the propagation of the beams once the they exit the SPDC medium. The wave vectors are

$$k_p = k_s + k_i + \frac{\zeta}{c_0}, \tag{3.57}$$

where the k-vectors for signal ($k_s$) and idler ($k_i$) beams are offset from the k-vector of the pump ($k_p$) due to the energy loss in the crystal $\zeta/c_0$, where $c_0$ is the vacuum speed of light.

The state of the twin-photons generated by SPDC will evolve with time $t$ and space $x$. The state of the photons in the first arm of the MZI can be written as

$$\begin{aligned}
|\Psi_{SPDC}\rangle_1 &= \int d\omega_p G(\omega_p) \int d\omega_s \int d\omega_i \\
&\quad G(\omega_s)G(\omega_i)e^{i(\omega_s t - k_s x_1)}e^{i(\omega_i t - k_i x_1)} \left|H,H\right\rangle_{s,i} \delta(\omega_p - \omega_s - \omega_i - \zeta), \qquad (3.58)\\
&= \int d\omega_p G(\omega_p) \int d\omega_s \int d\omega_i G(\omega_s) G(\omega_p - \omega_s - \zeta) e^{i(\omega_p - \zeta_1)t} e^{-i(k_p - \frac{\zeta_1}{c_0})x_1} \left|H,H\right\rangle_{s,i},
\end{aligned}$$

where $G(\omega_p)$, $G(\omega_s)$, and $G(\omega_i)$ are the spectral functions of the pump, signal and idler photons respectively, and $\hbar\zeta_1$ is the energy loss in the crystal. Similarly, the state of the downconverted photons in the second arm of the MZI are given by:

$$|\Psi_{SPDC}\rangle_2 = \int d\omega_p G(\omega_p) \int d\omega_s \int d\omega_i G(\omega_s) G(\omega_p - \omega_s - \zeta) e^{i(\omega_p - \zeta_2)t} e^{-i(k_p - \frac{\zeta_2}{c_0})x_2} \left|V,V\right\rangle_{s,i}. \tag{3.59}$$

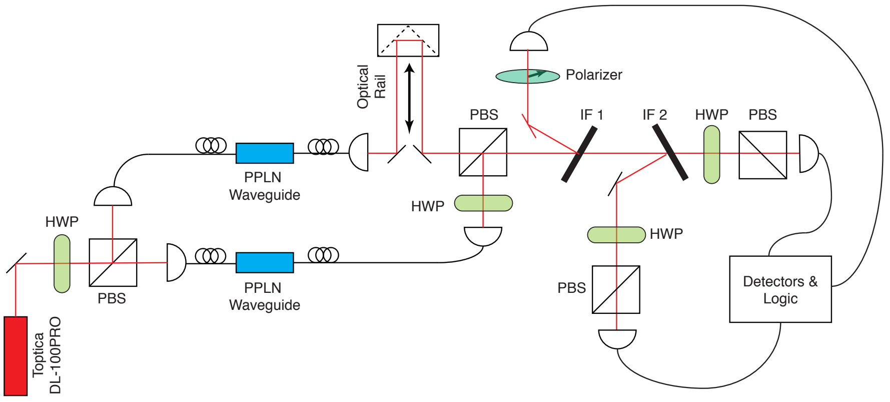

Figure 3.8: Experimental Setup. Our pump laser is a Toptica DL-100PRO which has a linewidth of about 1 MHz at 775 nm. The polarization of the pump light is set to $|D\rangle$ using a half-wave plate (HWP). A polarizing beamsplitter (PBS) forms the first part of a Mach-Zehnder Interferometer, splits the light equally between two arms. Each arm is fiber-coupled and then sent to a PPLN waveguide where Type-0 SPDC occurs. The resulting daughter photons are centered at 1530 nm and 1570 nm. The SPDC and pump light are outcoupled and recombined on a second PBS. An optical rail is inserted in one arm, allowing the path length to be varied by several meters. A filter (IF 1) is used to reject the pump light. The pump light is sent through a polarizer at $45^o$ and then the light is sent to a detector where the counts are modified. The telecom downconverted photons pass through IF 1 and are then separated by a second filter (IF 2) that transmits light above 1550 nm. A half-wave plate, polarizer, and single-photon detector are used to measure the polarization state of the downconverted photons in each arm, and the resulting signals are processed by coincidence logic.

The spectra of the downconverted photons from the two crystals are matched using temperature tuning. The combined output state of the MZI, which now includes the phase terms that depend on both arm lengths $x_1, x_2$, and the time $t$, is:

$$\begin{aligned} |\Psi\rangle = \quad & \int d\omega_p G(\omega_p) \int d\omega_s \int d\omega_i G(\omega_s) G(\omega_p - \omega_s - \zeta) e^{i(\omega_p - \zeta_1)t - k_p - \frac{\zeta_1}{c_0})x_1} \times \\ & \Big[ |H, H\rangle_{s,i} + e^{i(\zeta_2 - \zeta_1)t - k_p(x_2 - x_1) - \frac{\zeta_2}{c_0}x_2 + \frac{\zeta_1}{c_0}x_1} |V, V\rangle_{s,i} \Big], \end{aligned} \tag{3.60}$$

This is a polarization entangled state. Factoring out a global phase, this state can be rewritten as:

$$\begin{aligned} |\Psi\rangle = \quad & \int d\omega_p G(\omega_p) \int d\omega_s \int d\omega_i G(\omega_s) G(\omega_p - \omega_s - \zeta) \times \\ & \Big[ |H, H\rangle_{s,i} + e^{i(\zeta_2 - \zeta_1)t - k_p(x_2 - x_1) - \frac{\zeta_2}{c_0}x_2 + \frac{\zeta_1}{c_0}x_1} |V, V\rangle_{s,i} \Big], \end{aligned} \tag{3.61}$$

The phase term between the horizontal and vertical polarization depends on the path lengths, the frequency of the pump as well as the frequency mismatch.

A second polarizing beamsplitter recombines the two arms, placing the photons in the same output path. A dichroic mirror separates the signal and idler photons and they are then sent to a polarization analyzer and single-photon detectors. The polarization analyzers are set to measure in the $|D\rangle = \frac{1}{\sqrt{2}}(|H\rangle + |V\rangle)$ and $|A\rangle = \frac{1}{\sqrt{2}}(|H\rangle - |V\rangle)$ basis, leading to fringes as the phase between the two arms in the interferometer changes. The oscillations in the coincidence signal, in the limit of a narrowband pump after integrating over the signal and idler frequencies, are proportional to:

$$P_{coinc} \propto \frac{1}{2} \Big[ 1 + \cos((\zeta_2 - \zeta_1)t - (k_p(x_2 - x_1) - \frac{\zeta_2}{c_0}x_2 + \frac{\zeta_1}{c_0}x_1) \Big]. \tag{3.62}$$

For typical measurement time scales on the order of seconds $(\frac{\zeta_2}{c_0}x_2 + \frac{\zeta_1}{c_0}x_1) \ll (\zeta_2 - \zeta_1)t$ and we can ignore its contributions. For a fixed path delay the $(x_2 - x_1)k_p$ term is constant, and any oscillations will be due the $(\zeta_2 - \zeta_1)t$ term. We make the assumption that $\zeta_1$ and $\zeta_2$ fluctuate independently. This is reasonable as the crystals are far apart from one another and are contained in separate ovens; they each experience a different environment. Figure 3.9 shows the experimental results of a 0.22 m path delay measurement for both the

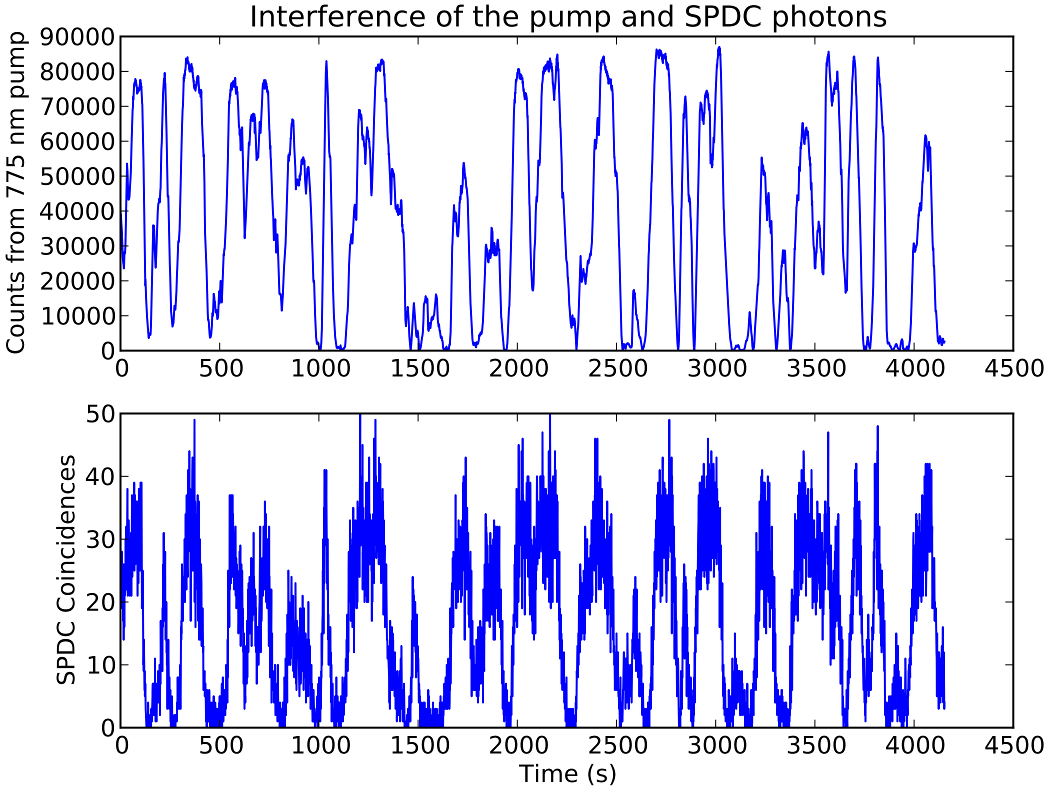

Figure 3.9: Interference fringes at a path delay of $(x_2 - x_1) = 0.22$ m. The top panel is the signal from the pump photons while the bottom panel is the coincidence data from the downconverted photons. Note that both signals closely follow one another.

pump and the SPDC coincidences. The frequency of the coincidence fringes is on the order of several Hz and we see a visibility of $.90 \pm .06$. If the fluctuations in the crystal energy loss were faster than the Hz timescale of the measurement, the fringes would be washed out and the visibility degraded. The energy loss would lead to frequency broadening on the Hz scale which is insignificant compared to the error bars in the main experiment on the MHz scale. Therefore $\Delta(\omega_p) = \Delta(\omega_s + \omega_i)$.

In our experiment, the change in phase that we observe is almost certainly due to instabilities in our path length since we made no attempt to actively stabilize the path length difference. If we observe the oscillations in the pump light, collected simultaneously, we see that the pump fringes closely follow the coincidence fringes. This measurement puts an upper bound on the change in the energy uncertainty at the Hz level, which is insignificant in our experiment.

### 3.7.2 Frequency dependent energy loss

The second scenario we consider is a crystal that, through additional sources of energy uncertainty, broadens the spectrum of the downconverted photons. If such broadening occurs, then the two-photon coherence length of photon pairs will be shorter than the coherence length of the pump. However, if the coherence length of the downconverted pair is the same as the pump's coherence length, then we can conclude that energy is conserved.

To measure the coherence length of the downconverted photons we use the same polarization MZI as before, except this time we introduce a variable path length imbalance. The state of the photons after the interferometer is given in Equation 3.62 except now $\zeta_1$ and $\zeta_2$ are frequency dependent. To see interference we again use a polarization analyzer to measure the state in the diagonal basis. The resulting two-photon coincidence oscillations are proportional to:

$$\begin{aligned} P_{coinc} \propto \quad & \int d\omega_p |G(\omega_p)|^2 \int d\omega_s \int d\omega_i |G(\omega_s) G(\omega_p - \omega_s - \zeta)|^2 \times \\ & \frac{1}{2}\Big[1 + \cos((\zeta_2 - \zeta_1)t - k_p(x_2 - x_1) - \frac{\zeta_2}{c_0}x_2 + \frac{\zeta_1}{c_0}x_1)\Big]. \end{aligned} \tag{3.63}$$

At long path length differences the frequency dependence of $\zeta_1$ and $\zeta_2$ in the $\frac{\zeta_1}{c_0}x_1 - \frac{\zeta_2}{c_0}x_2$ term can cause the fringes to wash out faster. This leads to a reduced visibility compared to what would be expected in the case where energy is conserved and $k_p(x_2 - x_1)$ is the only term.

In our experiment we measure the visibility of the coincidence fringes for a number of different path length imbalances and plot the results in Figure 3.10. Over the 2.4 m path length range scanned the visibility remains nearly constant. From a theoretical fit (assuming Gaussian pulses) of the coincidence data we find that $\Delta(\omega_s + \omega_i) = (7 \pm 6) \times 2\pi$ MHz. This is within error of the original $1 \times 2\pi$ MHz bandwidth of the pump. Furthermore, as seen in Figure 3.10, the pump visibilities closely track those measured for the downconversion, providing strong evidence that the coherence lengths of the downconverted photons and pump are the same and that energy is conserved.

If an extra $(7 \pm 6) \times 2\pi$ MHz of broadening takes place in each crystal in our triplet experiment, then we estimate the actual three-photon downonverted bandwidth to be $(12 \pm 7) \times 2\pi$ MHz (obtained by adding the extra broadening in quadrature with the measured pump bandwidth of $(6 \pm 2) \times 2\pi$ MHz). Even with this broadening we still violate the genuine tripartite inequalities from the main paper by 31, 48, 48, and 48 standard deviations respectively.

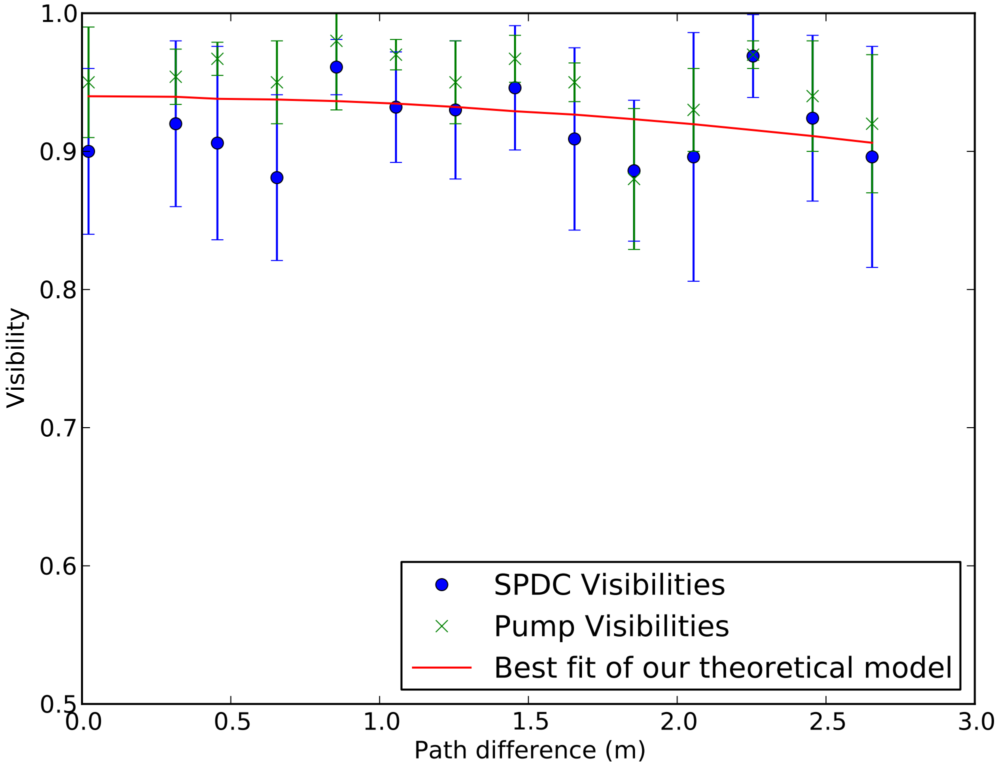

Figure 3.10: Interference visibility over different path lengths in the MZI. Blue circles correspond to the measured visibilities for the SPDC photons. For comparison the visibilities of the pump light, measured simultaneously with the SPDC data, are shown as the green crosses. The pump visibilities and SPDC visibilities are strongly correlated with one another. The theoretical model that best fits the SPDC data has a $\Delta(\omega_s + \omega_i) = (7 \pm 6) \times 2\pi$ MHz.

# Chapter 4

# Direct generation of three-photon polarization entanglement

## 4.1 Notes and acknowledgements

In this chapter we describe the experimental demonstration of genuine tripartite polarization entanglement of photon triplets produced by cascaded downconversion, and their application as a source of heralded Bell pairs.

**Notice**: The content of this chapter is part of manuscript to be submitted for publication. The full list of authors is:

Deny R. Hamel, Lynden K. Shalm, Hannes Hübel, Aaron J. Miller, Francesco Marsili, Varun B. Verma, Richard P. Mirin, Sae Woo Nam, Kevin J. Resch and Thomas Jennewein

## 4.2 Abstract

Non-classical states of light are of fundamental importance for emerging quantum technologies. Cascaded downconversion is a promising method for creating multipartite entangled-photon states. Here, we show the direct production of polarization-entangled photon

triplets in a Greenberger-Horne-Zeilinger (GHZ) state by cascading two entangled downconversion processes. Using high efficiency superconducting nanowire single-photon detectors, we detect photon triplets at a rate of 660 per hour, with a state fidelity of 86%. We use our three-photon entangled state to test local realism by violating the Mermin and Svetlichny inequalities, and show the ability to herald Bell states, a task which was not possible with previously demonstrated three-photon GHZ states. These results represent a significant breakthrough in multi-photon entangled state production, and provide a new resource for optical quantum information processing.

## 4.3 Introduction

Quantum optical technologies promise to revolutionize fields as varied as computing, metrology and communication. In most cases these applications require entangled states of light, but because photons are notoriously weakly interacting, creating entanglement between photons after they have been produced is challenging [3, 93]. Consequently, the ability to generate entanglement during the production process is of crucial importance for photons. New capabilities of quantum sources are thus critical for the advancement of quantum optical implementations.

The production of high-quality multi-photon entanglement, such as Greenberger-Horne-Zeilinger (GHZ) states [63], is particularly challenging. Currently the most established method for producing photonic entanglement is spontaneous parametric downconversion (SPDC). This is a process which naturally produces photons in pairs, making it simple to entangled the various degrees of freedom of two photons [27, 28, 30]. On the other hand, experiments with three or more entangled photons [36, 37, 42, 39, 40] have thus far relied on combining photons from two or more different pair sources using linear optics and employing outcome post-selection: selecting only a specific subset of measurement outcomes while ignoring others [35, 94].

With this approach, the action of observing the photons both creates and destroys the state at the same time. While this post-selection may be acceptable for some applications, it restricts the usefulness of the resulting entangled states for others. One example is heralding Bell states, also known as event-ready entanglement, which is the ability to know that a maximally entangled two-photon state is present before it is destroyed [95, 96]. This task, which is useful for applications such as quantum repeaters [76], loophole-free Bell tests [97] and optical quantum computing [98, 99], is in theory easily achieved with an appropriate three-photon state, but does not work if this state is created with SPDC and outcome post-selection. Therefore, creating three-photon entanglement directly, without the need for such post-selection, would represent a significant advance in photonic quantum information processing.

This goal can be achieved through cascaded downconversion [34, 100, 56], a process where one of the photons from a primary SPDC process is used to pump a secondary downconversion source. Specifically, if the primary source produces polarization-entangled photon pairs, and one of those photons is used to pump a secondary polarization-entangled source [101], the resulting three-photon state will be a GHZ entangled state (Fig. 4.1A). In this work, we use cascaded downconversion to produce entangled photon triplets directly without relying on outcome post-selection. We fully characterize the entangled photon triplets with quantum state tomography, use them to perform local realism tests and to generate heralded Bell states.

While cascaded downconversion naturally produces photon triplets which are entangled in energy and time [102], to obtain polarization entanglement is significantly more challenging. It is necessary to create a coherent superposition of two orthogonally polarized cascaded downconversion processes (Fig. 4.1A), where the photons must be indistinguishable in their spectral, timing, and spatial characteristics. In addition, the phase between the two processes has to be stable. These requirements are challenging due to the properties of the high-efficiency downconverters employed here to make cascaded downconversion possible.

Fully characterizing a three-qubit state with quantum state tomography requires at least $3^3 = 27$ measurement settings. Performing this number of measurements with sufficient event statistics would be very challenging with the highest previously reported detection rates of 7 triplets per hour [102], where an important limiting factor was the low single-photon detection efficiency. Here, we employ newly developed superconducting nanowire single-photon detectors (SNSPDs) with high system detection efficiency of over 90% at 1550 nm [103], promising a hundred-fold increase in detected triplet rates. This dramatic improvement enables us to perform quantum state tomography and other demanding tests and applications of the three-photon entangled state.

## 4.4 State production and characterization.

The three-photon states we aim to produce are GHZ states of the form

$$|\mathrm{GHZ}^{\pm}\rangle = \frac{1}{\sqrt{2}}(|HHH\rangle \pm |VVV\rangle). \tag{4.1}$$

Here $|H\rangle$ and $|V\rangle$ represent horizontally and vertically polarized photons respectively. The setup (Fig. 4.1B) can be understood as a cascade of two sources of entangled photon pairs [101]. First, a Sagnac source [30, 104] produces non-degenerate polarization-entangled photon pairs with wavelengths of 776 nm and 842 nm into modes 0 ad 1 respectively. These are in the Bell state $|\Phi\rangle = \frac{1}{\sqrt{2}}(|H\rangle_0|H\rangle_1 + e^{i\theta(\vartheta)}|V\rangle_0|V\rangle_1)$, where the phase $\theta(\vartheta)$ can be controlled by tuning the tilt angle $\vartheta$ of the quarter-wave plate (QWP) in the pump beam. The 776 nm photon is used to pump the second entangled photon pair source, a polarizing Mach-Zehnder interferometer with a downconversion crystal in each arm [105]. If it downconverts, pair of photons at 1530 nm and 1570 nm are created in modes 2 and 3 with a polarization state depending on the pump photon according to: $|H\rangle_0 \rightarrow |H\rangle_2|H\rangle_3$ or $|V\rangle_0 \rightarrow e^{i\phi}|V\rangle_2|V\rangle_3$, where $\phi$ is the phase difference between the paths. This phase is kept constant using active stabilization. The quantum state describing the photon triplets is

$$|\psi\rangle = \frac{1}{\sqrt{2}}\left(|H\rangle_1|H\rangle_2|H\rangle_3 + e^{i(\phi+\theta(\vartheta))}|V\rangle_1|V\rangle_2|V\rangle_3\right). \tag{4.2}$$

Each photon is subjected to a polarization projective measurement, and detected using single photon detectors. All three-photon detection events are recorded as a set of time stamps. To analyze the data we use a coincidence window of 1.25ns, which is larger than the combined timing jitters of the detectors and the timing electronics. We observe the phase dependance of the GHZ states by changing the pump QWP tilt angle $\vartheta$, and measuring the three-photon correlation in the diagonal polarization basis, $E(\sigma_x, \sigma_x, \sigma_x)$ with $\sigma_x = |H\rangle\langle V| + |V\rangle\langle H|$ (see supplementary materials). Quantum mechanics predicts that for the state in equation 4.2, $E(\sigma_x, \sigma_x, \sigma_x) = \langle\sigma_x\sigma_x\sigma_x\rangle = \cos(\phi + \theta(\vartheta))$. The high-visibility sinusoidal dependance of the correlation on the phase $\theta(\vartheta)$ (Fig. 4.2) is a clear

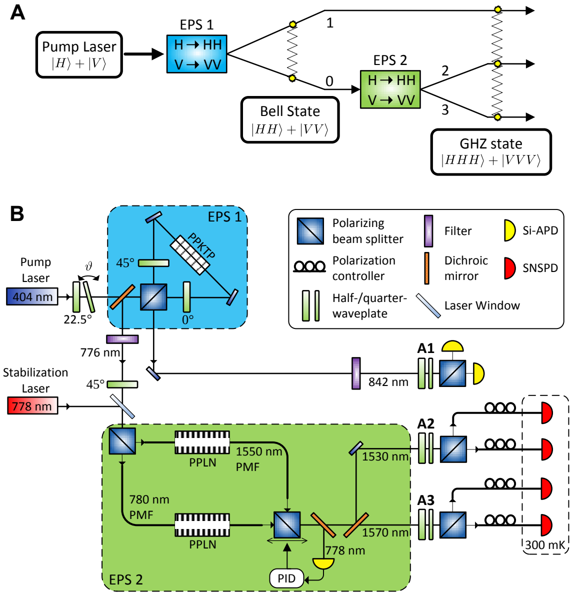

Figure 4.1: Polarization entangled photons using cascaded SPDC. (**A**) Basic scheme. The first entangled photon source (EPS1) produces entangled photons in modes 0 and 1. The photon in mode 0 is used to pump the second entangled photon source (EPS2), thus transferring the entanglement to two new photons in modes 2 and 3 to produce a GHZ state. (**B**) Detailed setup. A Sagnac source produces entangled photon pairs at 842 nm and 776 nm using a periodically-poled potassium titanyl phosphate (PPKTP) crystal. The photons at 776 nm are used to pump a Mach-Zehnder source, which produces entangled photons at 1530 nm and 1570 nm in periodically-poled lithium niobate (PPLN) waveguides. The three-photon state is analyzed using controllable measurement settings implemented with motorized wave plates (A1, A2 and A3) and polarizing beam splitters. Photons at 842 nm are detected using silicon avalanche photodiodes (Si-APD), while photons at telecom wavelengths are detected using superconducting nanowire single-photon detectors (SNSPD). The signal from all detectors is sent to a time-tagging unit. The phase in the interferometer is controlled using a piezo-controller and a proportional-integral-derivative controller (PID). See supplementary materials for additional details.

signature of GHZ entanglement. For subsequent measurements, the QWP tilt angle is set such that the correlation is either at a minimum or a maximum, resulting in $|\mathrm{GHZ}^-\rangle$ or $|\mathrm{GHZ}^+\rangle$ respectively.

We fully characterize the three-photon state by performing quantum state tomography to reconstruct its density matrix. All 27 possible combinations of $\sigma_x$, $\sigma_y = -i|H\rangle\langle V| + i|V\rangle\langle H|$ and $\sigma_z = |H\rangle\langle H| - |V\rangle\langle V|$ are applied to the three photons. Each setting is measured for 16 minutes, over a total of 7.2 hours. A histogram of time differences for all three-photon detections (Fig. 4.3) shows the the tight temporal correlations of the triplets. Using a coincidence window of 1.25ns around the peak yields a total of 4798 three-fold coincidences which are used for tomographic state reconstruction. This corresponds to a triplet detection rate of 11.1 triplets per minute. The state is reconstructed using a semidefinite-programming algorithm implementation of the maximum likelihood method [61]. The reconstructed density matrix $\rho$ (Fig. 4.4) has a fidelity with the state $|\mathrm{GHZ}^-\rangle$ of $F = \langle\mathrm{GHZ}^-|\rho|\mathrm{GHZ}^-\rangle = 86.2\%$, a fidelity with $|\mathrm{GHZ}^+\rangle$ of 10.9% and a purity $P = \mathrm{Tr}(\rho^2)$ of 0.776. The most likely sources of imperfection are an incomplete overlap of the downconversion spectra of the two crystals in the second entangled pair source and an imperfect phase stabilization in the Mach-Zehnder interferometer. Nonetheless, our GHZ state fidelity is, to the best of our knowledge, the highest fidelity for a three-photon GHZ state measured with tomography, surpassing the previous records of 84% [66, 106].

## 4.5 Local realism tests

The original motivation behind the introduction of GHZ states was that multipartite entanglement allows for a striking exposition of the incompatibility of local realism and quantum mechanics [63], through inequalities such as Mermin's [33] or Svetlichny's [32]. These inequalities can also be recast as entanglement criteria [107, 108], and here we use them as a further demonstration of the quality of our GHZ state.

The Mermin inequality derived by imposing locality and realism for all particles. Here, we look at the following three-particle version of the inequality:

$$S_{\mathrm{Mermin}} = |E(a', b', c) + E(a', b, c') + E(a, b', c') - E(a, b, c)| \leq 2. \tag{4.3}$$

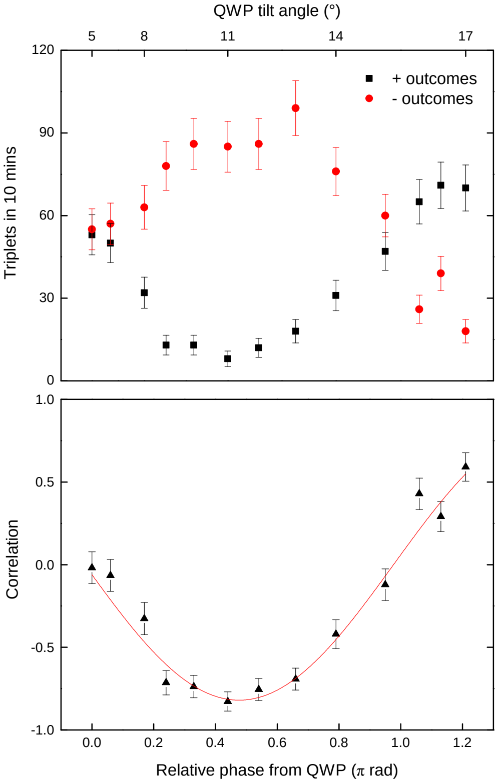

Figure 4.2: Measurement to determine optimal phase. Measured triplets with positive (black squares) and negative (red circles) contributions to the diagonal basis correlation (top), and the corresponding correlation $E(\sigma_x, \sigma_x, \sigma_x)$ (bottom). The line is a sinusoidal fit with the amplitude and phase as fitting parameters, from which we extract an amplitude of $0.82 \pm 0.03$. Setting the QWP tilt angle $\vartheta$ to $11^\circ$ produces a relative phase of $0.44 \pm 0.03\pi$ and minimizes the correlation, resulting in a $|\text{GHZ}^-\rangle$ state.

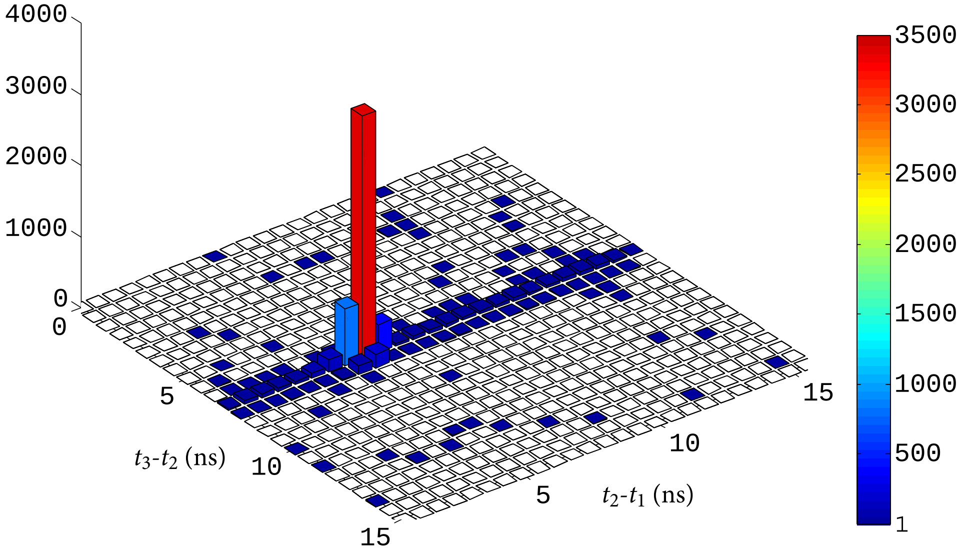

Figure 4.3: Two-dimensional histogram of time differences between detected photon events. The large peak corresponds to photon triplets from cascaded down-conversion, showing that they have tight time-correlations. The line above the background at a constant value of $t_3 - t_2$ is the main source of accidental triplets. It is due to events where a photon pair produced in the second downconversion is detected within 15 ns of an unrelated photon at 842 nm. The reason a similar line is not seen for a constant value of $t_2 - t_1$ is that the count rates at detectors 2 and 3 are three orders of magnitude smaller than those at $D_1$, so an accidental three-fold coincidence is much more likely to involve an uncorrelated photon at $D_1$. The resulting signal to noise ratio in this histogram is 73:1.

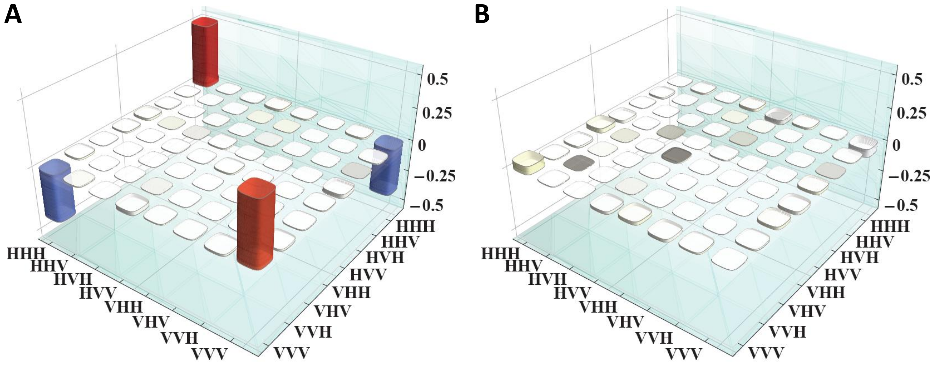

Figure 4.4: Real (**A**) and imaginary (**B**) parts of the tomographically reconstructed density matrix of the polarization-entangled photon triplets. The density matrix is reconstructed from the measured three-fold coincidences with no background subtraction.

The inequality holds for any local hidden variable theory. It can be violated with a GHZ state by applying the measurements $a = b = c = \sigma_x$ and $a' = b' = c' = \sigma_y$ and in the ideal case reaches the arithmetic limit of 4. These measurements are a subset of those used for the three-photon tomography. Of the 4798 triplet counts from the tomography, 674 correspond to the measurements for the Mermin inequality. They lead to the correlation values shown in table 4.1. Combining these results in a Mermin parameter of $\langle S_{\text{Mermin}} \rangle = 3.04 \pm 0.10$ that violates the local hidden variable limit by 10 standard deviations. Because we use Pauli measurements in the Mermin inequality, its violation is also a confirmation that the state is genuinely tripartite entangled [107]. The same conclusion can be reached even if our measurements are not ideal Pauli measurements, since a Mermin parameter larger than $2\sqrt{2}$ is a device independent test of genuine tripartite entanglement [109, 110, 111].

What the Mermin inequality cannot do is confirm the presence of tripartite nonlocality as it can be maximally violated with models allowing for arbitrarily strong correlations between two of the particles [110, 108]. The Svetlichny inequality addresses this problem, by allowing for arbitrarily strong correlations between any pair of particles, but otherwise enforcing locality and realism. [32]. A violation of the Svetlichny inequality thus guarantees the presence of multipartite nonlocality [112], and rules out a large class of non-local hidden variable theories which Mermin's inequality cannot. The Svetlichny inequality for three

| Mermin | | Svetlichny | |
|---|---|---|---|
| $E(a,b,c)$ | $-0.78 \pm 0.05$ | $E(a,b,c)$ | $0.56 \pm 0.06$ |
| $E(a,b',c')$ | $0.74 \pm 0.05$ | $E(a,b,c')$ | $0.63 \pm 0.06$ |
| $E(a',b,c')$ | $0.74 \pm 0.05$ | $E(a,b',c)$ | $0.65 \pm 0.06$ |
| $E(a',b',c)$ | $0.77 \pm 0.05$ | $E(a,b',c')$ | $-0.55 \pm 0.06$ |
| | | $E(a',b,c)$ | $0.59 \pm 0.06$ |
| | | $E(a',b,c')$ | $-0.59 \pm 0.06$ |
| | | $E(a',b',c)$ | $-0.62 \pm 0.05$ |
| | | $E(a',b',c')$ | $-0.71 \pm 0.05$ |
| $S_{\text{Mermin}}$ | $3.04 \pm 0.10$ | $S_{\text{Svet}}$ | $4.88 \pm 0.16$ |

Table 4.1: Mermin and Svetlichny correlations. Note that the Mermin and Svetlichny measurements for $c$ and $c'$ are not the same.

particles is

$$\begin{aligned} S_{\text{Svet}} = |&E(a,b,c) + E(a,b,c') + E(a,b',c) - E(a,b',c') + E(a',b,c) \\ &-E(a',b,c') - E(a',b',c) - E(a',b',c')| \leq 4. \end{aligned}$$

This inequality can be violated with a GHZ state, but the Pauli measurements from the three-qubit tomography are no longer sufficient. To test the Svetlichny inequality we perform another experiment using the measurement settings $a = b = \sigma_x$, $a' = b' = \sigma_y$, $c = \frac{1}{\sqrt{2}}(\sigma_x + \sigma_y)$ and $c' = \frac{1}{2}(\sigma_x - \sigma_y)$. In the ideal case, these measurements would result in a value of $S_{\text{Svet}} = 4\sqrt{2}$, which is the maximum value allowed by quantum mechanics. For this experiment 1960 three-fold coincidences are measured over a period of 3.2 hours. The values of the correlation are shown in Table 4.1. We find a Svetlichny parameter of $\langle S_{\text{Svet}} \rangle = 4.88 \pm 0.16$, violating the bound by 5 standard deviations. To the best of our knowledge, this is the strongest measured violation of the three-particle Svetlichny inequality to date.

## 4.6 Heralded Bell states

Our cascaded downconversion method of generating GHZ states allows us to directly herald Bell states, something which cannot be done with states produced using two independent

SPDC sources. Indeed, while previous experiments have shown heralded two-photon entangled states using photon pairs from SPDC and linear optics [113, 114], these schemes require a minimum of three photon pairs [96, 115]. To illustrate how our setup can be used as an event ready source of two-photon entanglement, we rewrite the GHZ state as

$$|\mathrm{GHZ}^+\rangle = \frac{1}{\sqrt{2}}(|\Phi^+\rangle|D\rangle + |\Phi^-\rangle|A\rangle), \tag{4.4}$$

where $|D\rangle = \frac{1}{\sqrt{2}}(|H\rangle + |V\rangle)$ and $|A\rangle = \frac{1}{\sqrt{2}}(|H\rangle - |V\rangle)$ represent diagonal and anti-diagonal polarizations respectively, and $|\Phi^\pm\rangle = \frac{1}{\sqrt{2}}(|HH\rangle \pm |VV\rangle)$ are Bell states. By projecting one of the photons in the diagonal basis, we can herald the presence of one of two Bell states in the other two modes. The heralding detection should come from one of the photons at telecom wavelengths so that the conversion efficiency of the second downconversion does not affect the overall heralding efficiency. In our experiment, we chose the 1530 nm photon to act as the herald. For this measurement the phase is set to prepare a $|\mathrm{GHZ}^+\rangle$ state. We measure the 1530 nm photon in the diagonal basis, and perform quantum state tomography on the other two photons. The density matrices resulting from each of the heralding outcomes (Fig. 4.5, A to D) have a fidelity of 89.3% with $|\Phi^+\rangle$ when heralding with $|D\rangle$, and 90.4% with $|\Phi^-\rangle$ when heralding with $|A\rangle$. Ignoring the outcome of the heralding measurement results in an incoherent mixture of $|HH\rangle$ and $|VV\rangle$ (Fig. 4.5, E and F). The fidelity with an equally weighed incoherent mixture is 96.6%.

We measure a rate of heralded two-photon pairs of 450 per hour. From this we can extract the heralding efficiency of the system, defined as the probability of detecting a Bell state given a heralding signal. For this experiment, the signal at the heralding detectors is dominated by dark counts, of which there are approximately 330 per second. This leads to a heralding efficiency of $1.9 \times 10^{-4}$. However, this is in no way a fundamental limit; it is entirely dominated by the ratio of signal photons to dark counts at the heralding detector. In cases where the heralding signal is not caused by a dark count but by a signal photon, the heralding efficiency is as high as 0.06, and is only limited by the coupling efficiency of the other two photons.

The measured heralding efficiency could be improved by using detectors with a lower dark count rate, by increasing the triplet production rate, or by optimizing the efficiency of single mode fiber coupling. Alternatively, switching the pump to a pulsed laser would

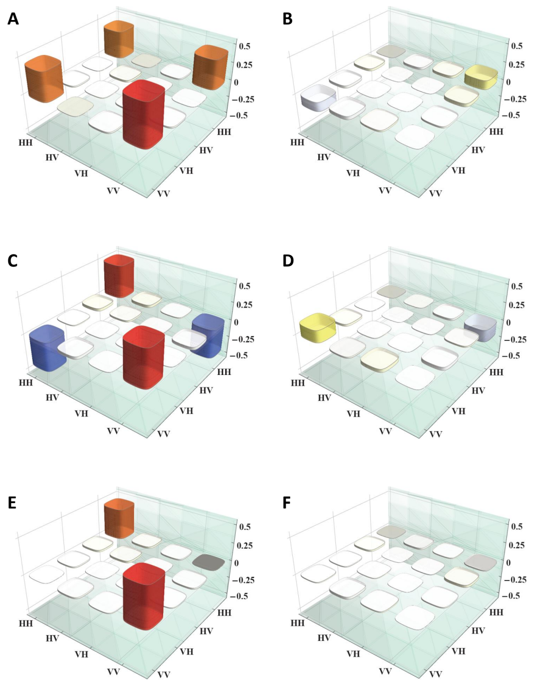

Figure 4.5: Real and imaginary parts of the reconstructed density matrices of the heralded two-photon states. The density matrices are reconstructed from 1632 triplets which were measured in 3.6 hours. (**A** and **B**) Heralding with $|D\rangle$ results in a state close to $|\Phi^{+}\rangle$. (**C** and **D**) Heralding with $|A\rangle$ results in a state close to $|\Phi^{-}\rangle$. (**E** and **F**) When heralding with $|D\rangle$ and $|A\rangle$ but ignoring the measurement outcomes, the coherent terms vanish, resulting in an incoherent mixture of $|HH\rangle$ and $|VV\rangle$.

provide additional timing information on the expected arrival time of the triplets, thus eliminating a significant portion of the dark counts at the heralding detectors.

It is interesting to compare the performance of our source of heralded Bell states to previous experiments. Entangled two-photons states have been heralded with rates and fidelities similar to that of our setup from optically [116] and electrically [117] pumped quantum dot systems. However, these experiments have much lower heralding efficiencies; to the best of our knowledge, the best reported heralding efficiency for these systems is $3.3 \times 10^{-9}$ [118], five orders of magnitude lower than what we measure here.

As for experiments based on six-photon schemes, they resulted in two-photon states with a lower fidelity of 84% [113] and 87% [114]. The measured heralding efficiency of approximately $10^{-2}$ (including coupling and detection losses) reported by the six-photon experiments is higher, but with the changes discussed above our measured heralding efficiency would approach or even surpass this value. In terms of detection rates, however, cascaded downconversion has a significant advantage compared to the the six-photon experiments. They detected at most 4 heralded Bell states per hour, a rate that is two orders of magnitude less than what we measure with our cascaded SPDC source. Moreover, the six photon schemes have an inherent trade-off between trigger rates and heralding efficiency. In our setup there is no such trade-off. The heralding efficiency is entirely limited by experimental imperfections, and would actually be improved by higher trigger rates. Cascaded downconversion has the additional advantage that, unlike the six-photon schemes which require all of the photons to be at the same wavelength so that they can interfere, it can be tuned to produce Bell pairs over a wide wavelength range. Our source is therefore compatible with both telecom and atomic systems, making it ideally suited for long-distance entanglement distribution.

Because of the high rate of heralded Bell states with cascaded SPDC, we are able to accumulate enough statistics to violate a Bell inequality with our heralded two-photon states. We use the CHSH inequality [13]

$$S^{\pm}_{\text{CHSH}} = |E(a,b) - E(a,b') \pm E(a',b) \pm E(a',b')| \leq 2, \tag{4.5}$$

where $a = \sigma_z$, $a' = \sigma_x$, $b = \frac{1}{\sqrt{2}}(\sigma_z + \sigma_x)$ and $b' = \frac{1}{\sqrt{2}}(\sigma_z - \sigma_x)$. Quantum mechanics predicts that the inequality can be violated up to a maximum of $S_{\text{CHSH}} = 2\sqrt{2}$. The results of our measurements are shown in Table 4.2. We find $S_{\text{CHSH}} = 2.62 \pm 0.16$ when heralding with $|D\rangle$, and $S_{\text{CHSH}} = 2.70 \pm 0.19$ when heralding with $|A\rangle$. Both correspond to violations by over 3 standard deviations of the local hidden variable limit.

| | $\vert D\rangle$ Heralding | $\vert A\rangle$ Heralding |
|---|---|---|
| $E(a,b)$ | $0.71 \pm 0.07$ | $0.77 \pm 0.06$ |
| $E(a,b')$ | $-0.66 \pm 0.08$ | $-0.65 \pm 0.07$ |
| $E(a',b)$ | $0.57 \pm 0.08$ | $-0.59 \pm 0.10$ |
| $E(a',b')$ | $0.68 \pm 0.07$ | $-0.69 \pm 0.07$ |
| $S_{\text{CHSH}}$ | $2.62 \pm 0.16$ | $2.70 \pm 0.19$ |

Table 4.2: CHSH correlations and $S_{\text{CHSH}}$ when heralding Bell states with $|D\rangle$ and $|A\rangle$.

A useful property of our method of heralding two-photon entangled states is that the amount of entanglement of the resulting two-qubit state can be tuned based on the heralding measurement, which is not possible in the six-photon schemes. For example, by projecting the second photon of a $|\text{GHZ}^-\rangle$ state onto $|\chi(\beta)\rangle = \cos\beta|H\rangle_2 + \sin\beta|V\rangle_2$, we obtain states of the form

$$|\psi(\beta)\rangle = \cos\beta|H\rangle_1|H\rangle_3 - \sin\beta|V\rangle_1|V\rangle_3. \tag{4.6}$$

To verify this, we vary the projection angle $\beta$, and perform tomography on the resulting two-photon state. The fidelity of the measured states with the predicted states, for $\beta = \pi/4$, $\beta = \pi/8$ and $\beta = 0$ is 78.4%, 87.8% and 96.4% respectively (82.0%, 85.6% and 94.8% for the orthogonal projections). The density matrices for these states are shown in the supplementary material.

## 4.7 Conclusions

In this experiment we demonstrate the direct generation of three-photon polarization entanglement with cascaded downconversion. This method does not rely on the interference of independently produced photon pairs, or on outcome post-selection of detected photons; every photon triplet produced in our source is in the desired GHZ state. The unique properties of this source enable a multitude of photonic quantum information tasks. As a first such demonstration, we have shown that our source can herald high-fidelity Bell states. It could also be useful as a source of multipartite entanglement for quantum communications protocols, such as quantum secret sharing [119]. We expect that our photon triplets are entangled in energy-time [102], opening the door to a demonstration of hyperentangled photon triplets [120]. With improved coupling efficiency out of the secondary downconversion, our method could be used for photon precertification [97] to mitigate the impact of loss inherent to sending photons over long distances; this would allow for extended range of quantum communication, device-independent quantum key distribution [121], and loophole-free Bell tests [97]. In addition, with further improvements in conversion efficiency through novel materials or pumped third-order nonlinearities [89], it may be possible to add more stages to the downconversion cascade. This provides an avenue to the direct generation of four or more photon states, and consequently the heralding of GHZ states.

## 4.8 Supplementary Materials

### 4.8.1 Materials and Methods

#### Production of photon triplets

A 25 mW 404 nm fiber-coupled grating stabilized laser diode (Toptica Bluemode) is used to pump a Sagnac source of entangled photons. The downconversion occurs in a 30mm periodically-poled potassium titanyl phosphate (PPKTP) crystal. This crystal's phasematching is temperature tuned to produces entangled photon pairs at 776 nm and 842 nm. The 842 nm photons are measured according to analyzer A1. The 776 nm photons are sent into a polarizing Mach-Zehnder interferometer, which contains a 30mm periodically-poled lithium niobate (PPLN) waveguide in each arm. The PPLN waveguides are also temperature controlled, phasematched to produce photons centered at 1530 nm and 1570 nm. After the Mach-Zehnder interferometer, the telecom photons are split by a dichroic mirror. The photons at 1530 nm and 1570 nm are measured at analyzers A2 and A3 respectively. The combined coupling and detection efficiency of the 842 nm photons is $\eta_1 = 0.23$ and for the 1530 nm and 1570 nm photons we have $\eta_2 = \eta_3 = 0.30$, measured from the coincidence to single detections ratio.

### Stabilization of the Mach-Zehnder interferometer

The phase in the interferometer is kept constant by active stabilization. A piezo positioning stage controls the position of the PBS at the exit of the Mach-Zehnder, based on a feedback signal provided by a 778 nm stabilization laser. The piezo stage's range alone is insufficient to stabilize the interferometer over long periods of time. It is therefore mounted on a motorized linear stage which is activated whenever the piezo stage approaches the limits of its range of motion.

### Projective measurements

The projective measurements on each photon are controlled using one half-wave plate and one quarter-wave plate, each of which is in a computer-controlled motorized rotation stage, placed in front of a polarizing beam splitter (PBS). Photons are measured at both outputs of the PBS. The correlation of a measurement is obtained by calculating the difference in relative frequency of events with a positive and negative product of outcomes. For example, for the $\sigma_z\sigma_z\sigma_z$ measurement, the correlation value is explicitly given by:

$$E(\sigma_z, \sigma_z, \sigma_z) = \frac{N_{hhh} - N_{hhv} - N_{hvh} + N_{hvv} - N_{vhh} + N_{vhv} + N_{vvh} - N_{vvv}}{N_{hhh} + N_{hhv} + N_{hvh} + N_{hvv} + N_{vhh} + N_{vhv} + N_{vvh} + N_{vvv}} \tag{4.7}$$

where $N$ is the number of counts with each outcome combination, and $h$ and $v$ represent the positive and negative eigenvalue outcomes of the $\sigma_x$ measurement.

To mitigate the effect of any imbalance in coupling or detection efficiency, we set the wave plates to alternate which output represents the positive outcome of any given measurement. For example, the $\sigma_z\sigma_z\sigma_z$ measurement is performed in eight different ways, where all three photons being transmitted by their respective PBSs corresponds to a projection onto the states: $|HHH\rangle$, $|HHV\rangle$, $|HVH\rangle$, $|HVV\rangle$, $|VHH\rangle$, $|VHV\rangle$, $|VVH\rangle$ and $|VVV\rangle$.

### Photon detection

Two types of detectors are used for this experiment. The 842 nm photons are detected with free running silicon avalanche photodiodes (Si-APD) which have 40% efficiency at that wavelength. The photons at 1530 nm and 1570 nm are detected using free-running tungsten silicide superconducting nanowire single-photon detectors (SNSPD), with 90% system efficiency. The SNSPDs are operated at a temperature of approximately 330 mK inside a compact, sealed, two-stage sorption-pumped $^3$He refrigerator with a sorption-pumped $^4$He stage for heat sinking of the wiring and optical fibers. The sorption refrigerator stages are cooled by a closed-cycle Gifford-McMahon cryocooler with a nominal cooling power of 100 mW at 4.2 K. For these experiments, the complete cycle lasts 6.5 hours, of which approximately 4 hours is spent with the detectors at operating temperature. We record time stamps of all events when three photons are detected within 15 ns of each other using a time-tagger (DotFast/UQDevices) with a resolution of 156 ps.

### 4.8.2 Description of the quantum state

Assuming a monochromatic pump of frequency $\omega_p$, the quantum state after the first down-conversion can be written as

$$\Psi_{SPDC1} \approx \int_{\omega_1} d\omega_1 G_1(\omega_1, \omega_p - \omega_1) \left[ a^\dagger_{1,H}(\omega_1) a^\dagger_{0,H}(\omega_p - \omega_1) + e^{i\theta(\vartheta)} a^\dagger_{1,V}(\omega_1) a^\dagger_{0,V}(\omega_p - \omega_1) \right], \quad (4.8)$$

where $G_1(\omega_1, \omega_p - \omega_1)$ is the joint-spectral functions resulting from the phasematching in the PPKTP crystal. We assume that it the same for the horizontal and vertical photons since in the Sagnac configuration they both come from the same crystal. After the second SPDC, the state becomes

$$\begin{aligned} \Psi_{CSPDC} \approx \int_{\omega_1} \int_{\omega_2} & d\omega_1 d\omega_2 G_1(\omega_1, \omega_p - \omega_1) \\ & \Big[ G_{2,H}(\omega_2, \omega_p - \omega_1 - \omega_2) a^\dagger_{1,H}(\omega_1) a^\dagger_{2,H}(\omega_2) a^\dagger_{3,H}(\omega_p - \omega_1 - \omega_2) + \\ e^{i(\theta(\vartheta)+\phi)} & G_{2,V}(\omega_2, \omega_p - \omega_1 - \omega_2) a^\dagger_{1,V}(\omega_1) a^\dagger_{2,V}(\omega_2) a^\dagger_{3,V}(\omega_p - \omega_1 - \omega_2) \Big], \end{aligned} \quad (4.9)$$

where $G_{2,H}(\omega_2, \omega_p - \omega_1 - \omega_2)$ and $G_{2,V}(\omega_2, \omega_p - \omega_1 - \omega_2)$ are joint-spectral functions for photons produced in either of the PPLN crystals. These include effects of phasematching, as well as any dispersion coming from the fibers after the downconversion. If the two joint spectral functions are equal, in other words if the photons produced in either one of the two PPLN crystals are indistinguishable, then we have

$$\begin{aligned}\Psi_{CSPDC} \approx \int_{\omega_1}\int_{\omega_2} d\omega_1 d\omega_2 G_1(\omega_1, \omega_p - \omega_1) G_2(\omega_2, \omega_p - \omega_1 - \omega_2) \\ \Big[a^\dagger_{1,H}(\omega_1) a^\dagger_{2,H}(\omega_2) a^\dagger_{3,H}(\omega_p - \omega_1 - \omega_2) + e^{i(\theta(\vartheta)+\phi)} a^\dagger_{1,V}(\omega_1) a^\dagger_{2,V}(\omega_2) a^\dagger_{3,V}(\omega_p - \omega_1 - \omega_2)\Big].\end{aligned} \tag{4.10}$$

In this form, the energy-time and polarization correlations of the state are evident. Considering only polarization, the resulting state is

$$\Psi_{CSPDC} = \frac{1}{\sqrt{2}}(|HHH\rangle + e^{i(\theta(\vartheta)+\phi)}|VVV\rangle), \tag{4.11}$$

which is the desired entangled GHZ state.

It is crucial that the two joint-spectral functions be equal. To achieve this, the phasematching curves of both crystals are measured, and their temperatures are independently controlled and set to have maximum overlap of the two downconversion spectra. Additionally, because the telecom photons produced in the second downconversion are broadband (~30 nm FWHM), the entanglement visibility can be easily degraded by unbalanced group velocity dispersion in optical fibers. This was significant in our experiment because the fibers pigtailed to the PPLN samples were not exactly of the same length. We compensated for this imbalance by including additional polarization maintaining fiber in one arm. To find the optimal length of fiber to add, we tried different lengths of fibers and measured the resulting entanglement visibility of the Mach-Zehnder source (Fig. 4.6). This is measured by pumping the Mach-Zehnder source with a laser and measuring the photon pairs in the diagonal basis without stabilizing the phase. The visibility of the resulting fringes is the entanglement visibility. Based on these measurements, we added 15 cm of polarization maintaining fiber to one path of the interferometer.

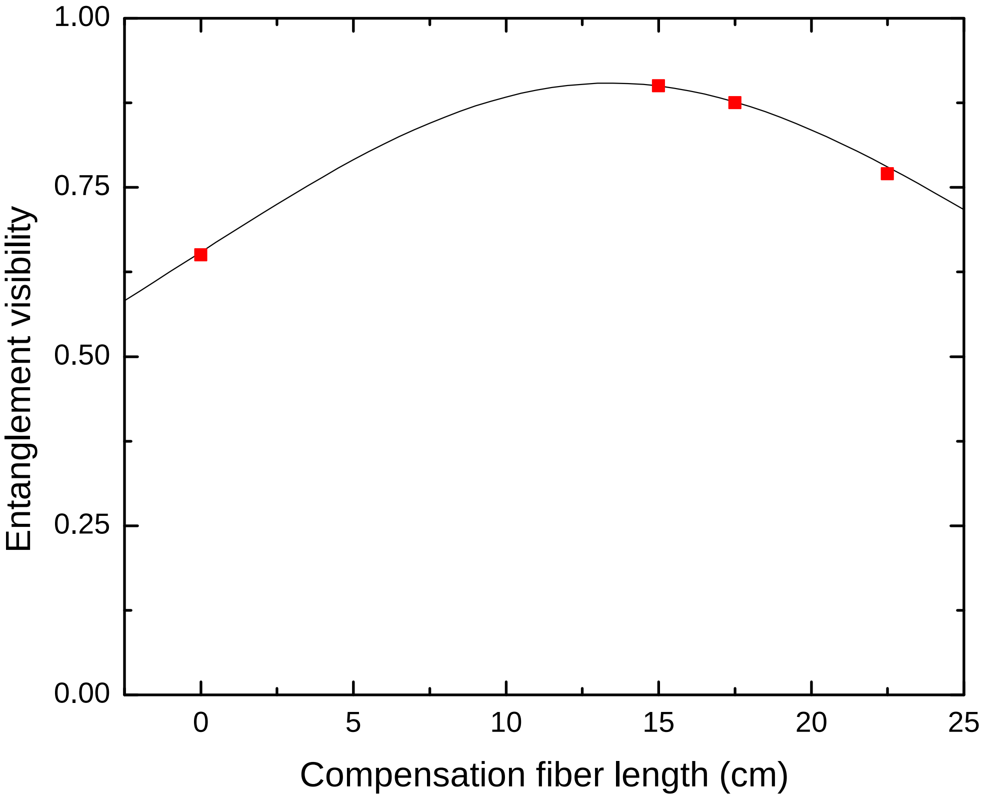

Figure 4.6: Effect of fiber length mismatch on entanglement visibility. The data points correspond to measured entanglement visibility of the Mach-Zehnder source when different compensation fibers were inserted. The line is calculated using dispersion data for fused silica, assuming an SPDC bandwidth of 28nm and a maximum visibility of 90%

### 4.8.3 Heralding non-maximally entangled states

As was discussed in the main text, our two-photon state heralding method allows us to tune the amount of entanglement in the heralded states. We start with the $|\mathrm{GHZ}^-\rangle$ state

$$|\mathrm{GHZ}^-\rangle = \frac{1}{\sqrt{2}}(|HHH\rangle - |VVV\rangle). \tag{4.12}$$

By projecting the heralding photon onto the state $|\chi(\beta)\rangle = \cos\beta|H\rangle + \sin\beta|V\rangle$, we obtain the following two-photon state in the other two modes:

$$|\psi(\beta)\rangle = \cos\beta|HH\rangle - \sin\beta|VV\rangle. \tag{4.13}$$

To showcase this, we selected three values of $\beta$: $\pi/4$, $\pi/8$ and 0. For each value of $\beta$, we reconstructed the heralded two-photon state using quantum state tomography. The reconstructed density matrices of the heralded states are in Figure 4.7. The fidelity with the ideal states for $\beta = \pi/4$, $\beta = \pi/8$ and $\beta = 0$ is 78.4%, 87.8% and 96.4% respectively for the positive outcome of the $|\chi(\beta)\rangle$ measurement, and 82.0%, 85.6% and 94.8% for the negative outcome of the $|\chi(\beta)\rangle$ measurement.

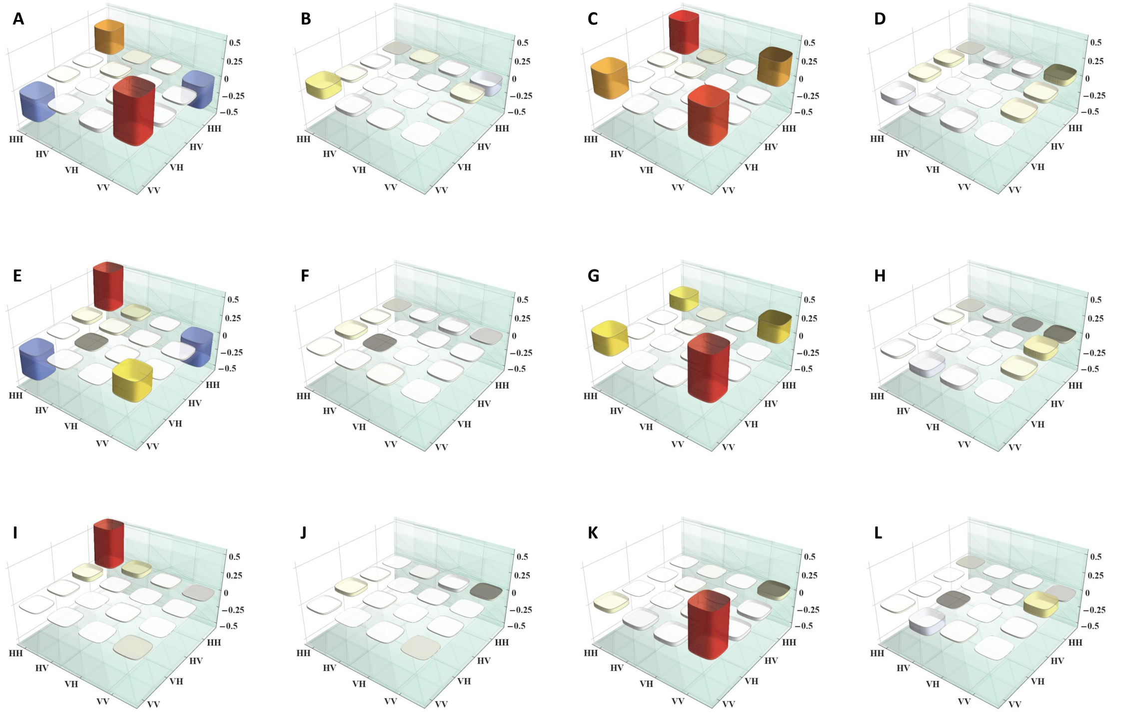

Figure 4.7: Reconstructed density matrices of heralded non-maximally entangled two-photon states. The real and imaginary parts of the density matrices are shown when heralding with $\cos\beta|H\rangle + \sin\beta|V\rangle$ and the corresponding orthogonal measurement. For $\beta = \pi/4$, the fidelities with the ideal states are 78.4% (**A** and **B**), and 82.0% (**C** and **D**); for $\beta = \pi/8$ the fidelities are 87.8% (**E** and **F**) and 85.6% (**G** and **H**); and for $\beta = 0$ the fidelities are 96.4% (**I** and **J**) and 94.8% (**K** and **L**).

# Chapter 5

# Additional experimental details

## 5.1 The Sagnac source of entangled photons

In most respects, the Sagnac source of entangled photon pairs used for the experiments shown in Chapter 4 is similar to the one described in my MSc thesis. [31]. Consequently, instead of presenting a detailed description of the Sagnac source of entangled photons, we will highlight the differences between the two sources. The main changes are shown in Figure 5.1.

The first necessary modification is the PPKTP crystal. In my MSc work, degenerate SPDC at 808 nm was produced in a PPKTP crystal from a 404 nm pump. In the experiments described here, we need SPDC at 776 nm and 842 nm from the same pump wavelength. To reach these frequencies with the same crystal, it would have to be heated to approximately 200 °C. Since this is not practical, we need a crystal with a different poling period. We replace the PPKTP crystal with a 30 mm crystal which has a slightly shorter poling period of 9.35 $\mu$m, thus producing 776 nm downconversion at around 45 °C. This is illustrated in the theoretical phasematching curves in Figure 5.6.

Because the Sagnac source is no longer operated at wavelength degeneracy, several components need to be changed. Some of these modifications are fairly obvious — the dual wavelength HWP and PBS in the Sagnac loop now need to act at three different wavelengths: 404 nm, 776 nm and 842 nm. The HWP is a superachromatic quartz and MgF2

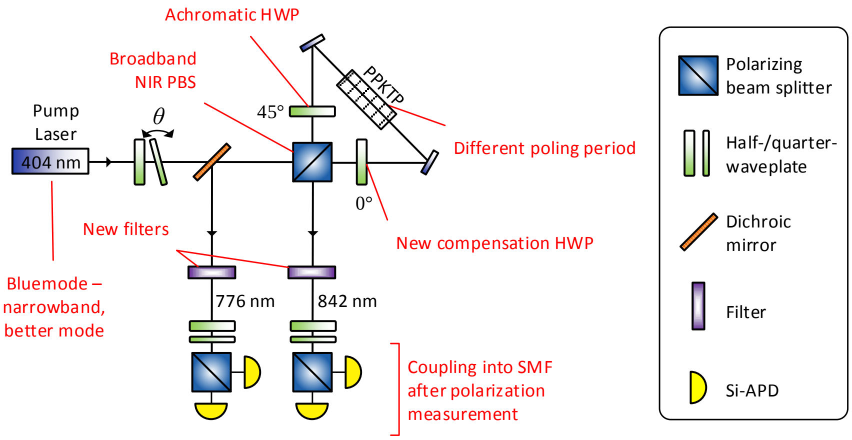

Figure 5.1: Sagnac source of entangled photon pairs. The important changes to the sources are shown in red. See text for details.

retarder from B. Halle, which is designed to work from 310 nm to 1100 nm. It is difficult (or at least expensive) to find a PBS designed to perform well at these three wavelengths. We therefore used one which is designed to function at the two SPDC wavelengths, and that worked reasonably well for the pump. This is acceptable because even if it does not perform perfectly for the pump, the quality of the produced entangled state is not affected; it only causes an additional loss for one of the pumping directions of the Sagnac loop, and this can be compensated by changing the polarization of the pump beam.

Another necessary modification to the setup was changing the filters placed in front of the single mode fiber couplers. These filters help reduce background light, notably by various sources of fluorescence in the setup. For this experiment, we used 12 nm bandpass filters from Semrock, centered at 780 nm and 840 nm.

We also added a second achromatic HWP inside the Sagnac. Experimentally, we found that without this compensation wave plate the source had a visibility in the diagonal basis of 87.5%. When we added the second wave plate we measured a visibility of over 95%.

Other modifications were unrelated to the downconversion wavelengths. We changed the pump laser, from a Toptica iWave to a Toptica Bluemode. The latter has a narrower frequency range, which was necessary for the demonstration of energy-time entanglement in Chapter 3. It also has the benefit of being fiber coupled, which results in a pump beam with a higher quality mode. Finally, we now perform the polarization measurement on the photons before coupling them into single-mode fibers, which helps to optimize the total photon coupling efficiency.

## 5.2 PPLN phasematching conditions

To observe cascaded SPDC, the wavelength produced by the first downconversion must match the acceptance bandwidth of the PPLN waveguides. We measured this acceptance bandwidth by sending a tunable pump laser in the PPLN waveguide and measuring the output power as a function of pump wavelength. These results are shown in Figure 5.2. The peak has a full width at half maximum of 0.3 nm, but to obtain optimal efficiency there is a range of approximately 0.05 nm which is ideal. The curve is also very asymmetric. These features can be understood by considering the phasematching curve of PPLN, a measurement of which is shown in Figure 5.3. We can see that for type-0 SPDC, there is no downconversion when the pump wavelength is longer that at the degeneracy point. This is why the conversion efficiency in Figure 5.2 drops off much faster as the pump goes to longer wavelengths.

Explaining the slower but significant drop in efficiency for shorter wavelengths requires more analysis. We can look at the theoretical PPLN phasematching curves which include bandwidth information, as shown in Figure 5.4. When the pump is near the degeneracy point so that the two downconversion spectrums begin to overlap, the effective SPDC bandwidth becomes very broad. This means that more frequency modes are phasematched, allowing for a stronger SPDC signal. To get a quantitative measure of this effect, we integrate Figure 5.4 over the entire SPDC bandwidth. This gives us the expected relative efficiency of downconversion as a function of the pump wavelength. The result of this calculation is shown and compared to our measurements in Figure 5.5. We can see that near the degeneracy point, the calculation agrees very well with our measured acceptance bandwidth. The agreement is not as good for shorter pump wavelengths, when the downconversion becomes very degenerate. The discrepancy is likely due to a combination of

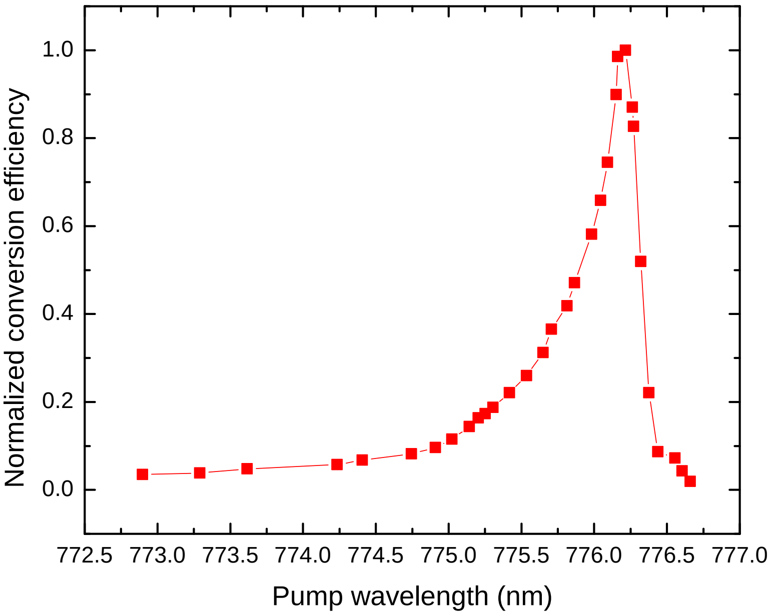

Figure 5.2: Measured pump wavelength dependance of PPLN downconversion efficiency. Here we show the normalized SPDC conversion efficiency of a PPLN waveguide as a function of the pump wavelength. The peak has a full width at half maximum of approximately 0.3 nm. The peak is asymmetric, with the efficiency falling off much more slowly for lower pump wavelengths. This can be understood from the phasematching curves shown in Figure 5.3, as explained in the main text.

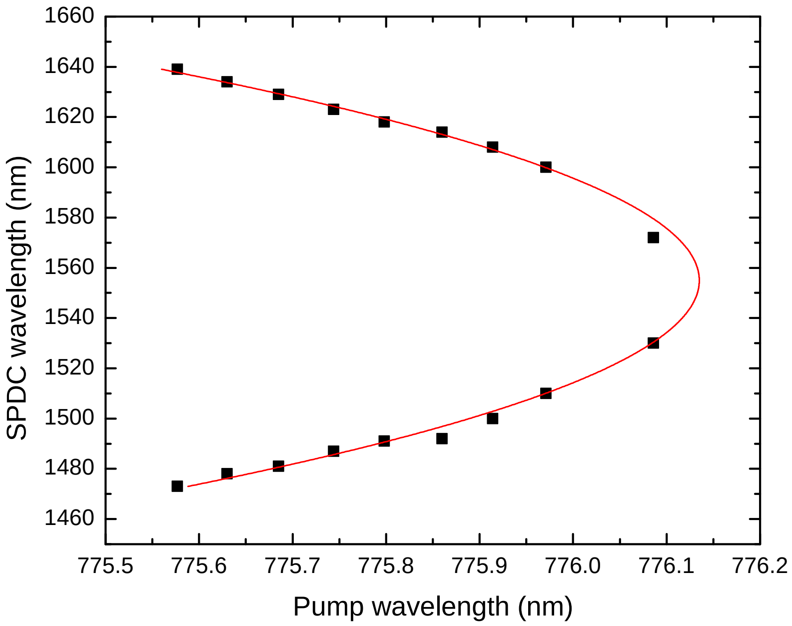

Figure 5.3: Measured PPLN phasematching curve. The curve is measured with the crystal at a temperature of 50.2 °. The points represent experimental measurements. The solid line is a polynomial fit, and is meant to act as a guide to the eye. There is no downconversion when the pump wavelength is longer than at the degeneracy point. As discussed in the main text, this explains the rapid drop in efficiency in Figure 5.2 for pump wavelengths longer than at the degeneracy point.

lower powermeter sensitivity and imperfect transmission in the waveguide and pig-tailed fiber for wavelengths far from 1550 nm. Another factor could be that the phasematching calculations are for a bulk crystal instead of a waveguide.

## 5.3 Setting the PPKTP temperature

Since the PPLN waveguides have a small acceptance bandwith, setting the PPKTP crystal to the right temperature is critical. As mentioned earlier, we need a precision on the 776 nm photon of around 0.05 nm. To get a sense of the restrictions this puts on the PPKTP temperature, we can compare it with theoretical phasematching curves for PPKTP, shown in Figure 5.6. From the slope of the curve, we calculate that the temperature dependance of the lower wavelength photon is approximately 0.22 nm/°C. Consequently, the precision requirement on the PPKTP temperature is of 0.2 °C.

Keeping the crystal at a specific temperature with a tolerance of 0.2 °C is not difficult. However, we must first determine the temperature at which the crystal needs to be set. At first glance, this might seem simple given the we have the data from Figure 5.2. However, there are a few caveats:

- The wavelengths in Figure 5.2 are measured with a spectrometer that is not sensitive to single-photon intensities. Setting the PPKTP temperature based on an absolute wavelength value from this plot would require a second spectrometer, which would have to be sensitive to single photons and very well calibrated with the first one.
- The phase matching curves for PPKTP in Figure 5.6 are very sensitive to the pump wavelength. The Toptica Bluemode, which we use as a pump, is usually stable on the timescale of our experiments, but sometimes when it is turned off and on again it will stabilize to a different wavelength. It is therefore preferable to optimize the PPKTP temperature before every experiment.
- Figure 5.2 is obtained by measuring the total output power from the PPLN waveguide. The maximum output power is obtained near degeneracy. However, in the experiments we use a dichroic mirror to split up the two wavelengths, and this dichroic

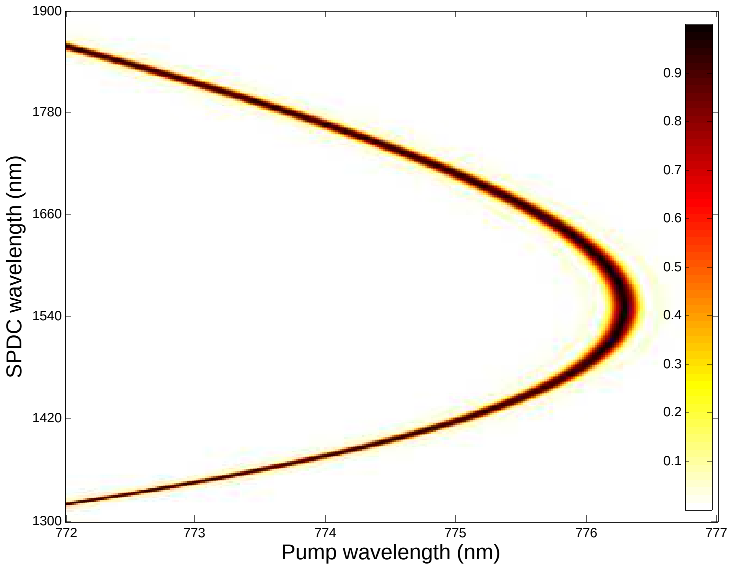

Figure 5.4: Theoretical PPLN phasematching curve for a 30 mm bulk PPLN crystal quasi-phasematched to produce degenerate SPDC from a 776.3 nm pump. The data for this curve was provided by L. K. Shalm [122].

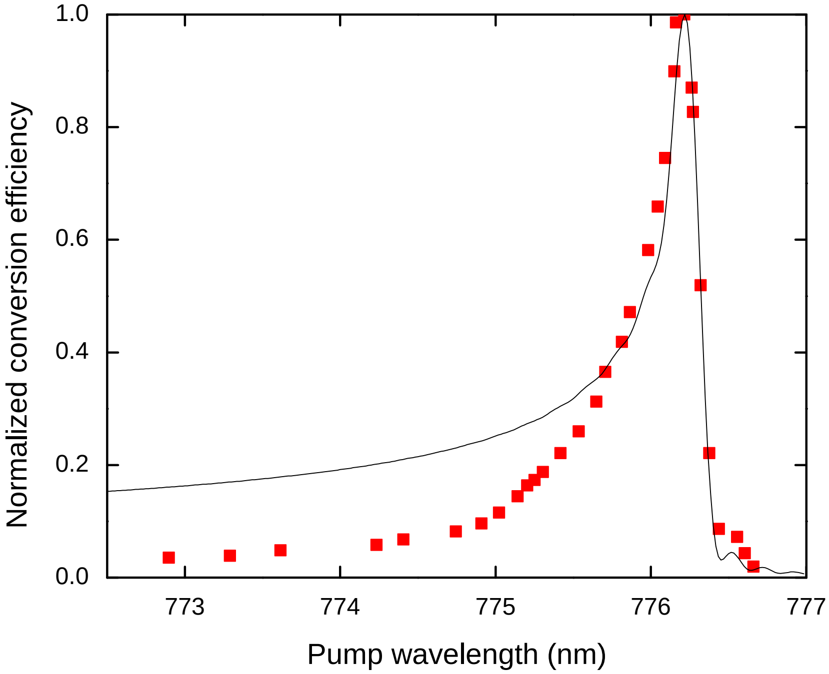

Figure 5.5: Theoretical pump wavelength dependance of PPLN downconversion efficiency. The line is obtained by integrating the phasematching curve in Figure 5.4 over downconversion wavelengths. The squares are the measured efficiencies from Figure 5.2. Both the theoretical and measured values are normalized. Far from degeneracy the agreement between the two curves is not as good, possibly because of lower powermeter sensitivity and higher loss in the waveguide for wavelengths far from 1550 nm.

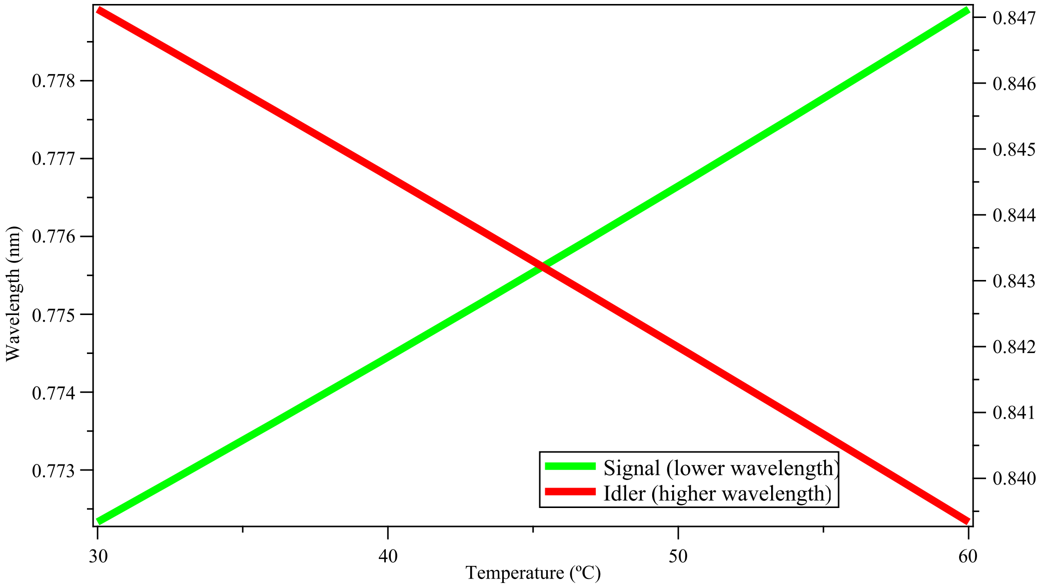

Figure 5.6: Theoretical PPKTP phasematching curves. These curves are calculated with the equations described in Appendix B of my MSc thesis [31], using a pump wavelength of 404 nm and a poling period of 9.35 $\mu$m. The lower wavelength photon has a temperature dependance of 0.22nm/°C.

mirror cannot function properly if the two telecom photons have the same wavelengths.

- The data from Figure 5.2 is obtained by pumping the PPLN crystal with an intensity of a few mW. This much intensity is sufficient to produce a rise in the temperature of the PPLN crystal, enough to change its phasematching conditions. Therefore, the optimal pump wavelength for the PPLN waveguides is different when it is pumped by single photons then with the strong laser.

As a solution to these issues, we use the following procedure. We pump the PPLN waveguides using a very weak tunable laser, and use single photon detectors to detect photons produce by SPDC. We then adjust the laser's wavelength to maximize the number of coincidences. Once the wavelength is optimized, we measure it on a spectrometer which is sensitive to single-photon intensities. This gives us the ideal wavelength at which the downconversion photons from the PPKTP crystal should be produced.

Before running an experiment, we measure the wavelength of SPDC photons coming from the PPKTP crystal using the same spectrometer. By tuning the PPKTP crystal's temperature for the downconversion wavelength to match the previously determined ideal wavelength, we can ensure an optimal efficiency for the cascaded SPDC process.

## 5.4 Stabilization of the Mach-Zehnder interferometer

### 5.4.1 Why use a Mach-Zehnder interferometer?

Ideally, the second SPDC source would also employ a Sagnac interferometer. However, the PPLN waveguides we use are fiber pigtailed with single mode fibers, so they can only be pumped in one direction. They are therefore not compatible with the Sagnac configuration.

Instead, we use two PPLN crystals in a Mach-Zehnder configuration. The main inconvenience is that unlike Sagnac interferometers, Mach-Zehnder interferometers are not inherently phase stable. The two possible paths through the interferometer are not the same, so temperature fluctuations or vibrations can affect the two paths differently, changing the relative phase between the two paths. This effect can be significant, and our Mach-Zehnder interferometer is no exception.

First, our Mach-Zehnder interferometer has relatively long path lengths of around 5 meters. In addition, most of the length of these paths is in optical fibers, which are sensitive to temperature changes. The temperature sensitivity is aggravated by the presence of a heated PPLN waveguide in the middle. The combined effect of all these factors is that the phase in the interferometer is only stable on the order of tens of seconds. Since we need to perform experiments that will last several hours, this phase stability must be addressed. The solution is to use active stabilization, as we described in Chapter 3. Here we give a few more technical details about this active stabilization.

### 5.4.2 Wavelength of the stabilization laser

The stabilization is complicated by the fact that light needs to go through three different waveguides in the interferometer: 780 nm PM fiber, the PPLN waveguide, and 1550 nm PM fiber. This limits the range of wavelengths that can be used for the stabilization. The PPLN waveguides in particular do not have good transmission at many wavelengths. We therefore chose to use a stabilization laser close to 776 nm, a wavelength which has good transmission through both types of optical fibers and through the waveguides. However, we need to be certain that the stabilization laser is not too close to 776 nm, otherwise it will be produce SPDC in the PPLN crystals. To see exactly how far from 776 nm the stabilization laser has to be, we can refer to Figure 5.2 again.

As discussed previously, the efficiency curve is asymmetric, dropping off much faster for pump wavelengths longer than at the degeneracy point. We exploit this asymmetry by setting the stabilization laser to a wavelength longer than 776 nm, thus minimizing any stray downconversion which it could produce. For the experiments, we use as a source for the stabilization a tuneable grating-stabilized laser diode (Toptica DL-100PRO) set to a wavelength between 778 nm and 780 nm.

### 5.4.3 Coherence length of the stabilization laser

We encountered difficulties with the stabilization, arising from fluctuations in the intensity of the individual beams going through each path of the Mach-Zehnder interferometer. One cause for this was interference within a single path, probably caused from back reflections at some of the fiber interfaces. To mitigate this problem, we reduced the coherence length of the laser artificially by using the scan control module (SC 110) of the DL-100PRO laser. For this to work, we need the amplitude of the modulation to be large enough for the coherence length of the laser to be smaller than the lengths between two reflections, which would be a few meters if the reflections occur in the optical fibers. We also need the modulation frequency to be faster than the acquisition frequency of the stabilization signal, which is about 100 Hz. For the experiments, the frequency was 985 Hz, and the amplitude setting was set to “2” on the SC 110, with symmetric modulation and no amplitude offset.

### 5.4.4 Input for the stabilization light

The next challenge to address for the stabilization is where to input the stabilizer laser light into the Mach-Zehnder interferometer. We considered a few options, shown in Figure 5.7.

The first one we tried was sending the light into the unused port of the PBS at the entrance of the interferometer, shown as Input 1 in Figure 5.7. The problem with this option is that the PPLN crystals act like partial polarizers, so most of the stabilization light will not be transmitted by the waveguide. We do not require much signal for the stabilization, so the attenuation alone is not a problem. The complications only arise when we take measurements over long periods. If over time there a small change in the polarization of the light going into the waveguide, it can have a large relative effect on the intensity transmitted through it. This option is therefore not optimal; it is better for the stabilization laser to enter the interferometer with the same polarization as the 776 nm SPDC photons.

The next alternative we tried (Input 2) was to send the stabilization laser light through the dichroic mirror of the Sagnac source. This mirror is supposed to reflect the 776 nm SPDC light, so it is highly reflective for the stabilization laser as well. Nonetheless, by

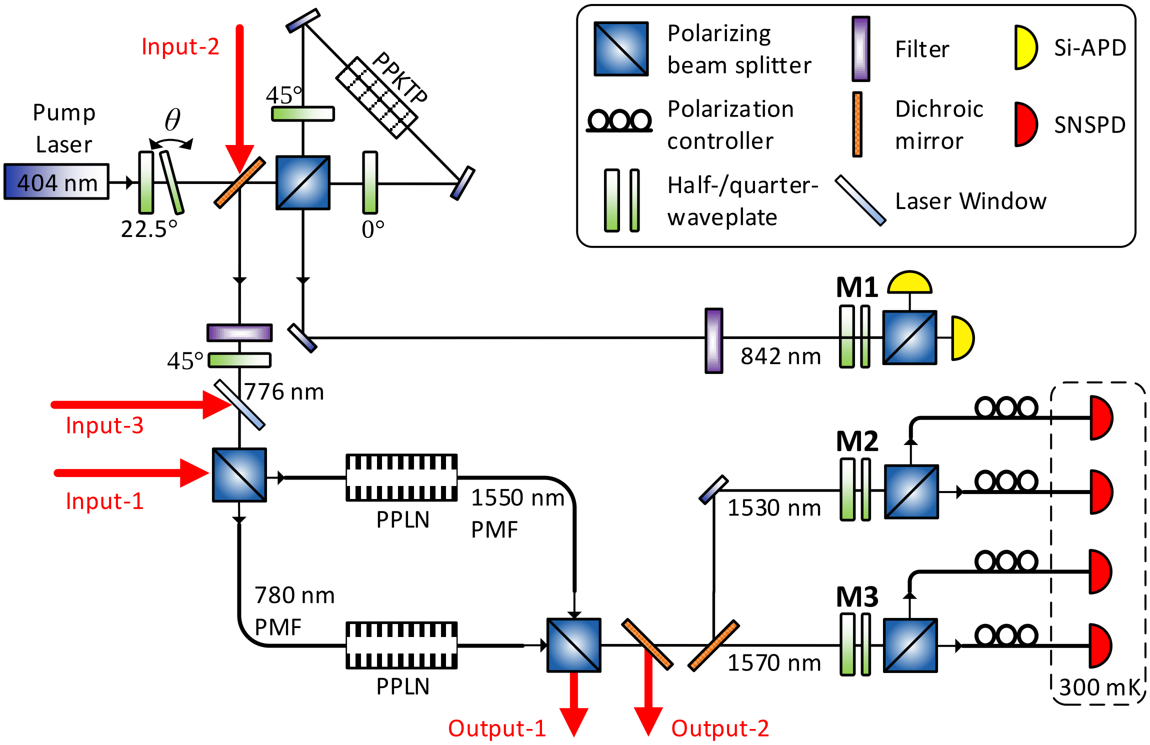

Figure 5.7: Possible inputs and outputs for stabilization laser. For the experiments, we used input 3 and output 2, as this was found to produce the most stable signal.

sending the stabilization laser in path 2, a small portion of the light — around 1% — is transmitted and can be used to stabilize the interferometer. This however leads to the same problem as the first option: a small absolute change in the transmission of the dichroic mirror results in a large absolute change in the transmitted intensity. Again, we found that these fluctuations were to large too make this option practical.

Finally, we tried Input 3, which uses a low reflectivity laser window to combine the stabilization beam with the 776 nm SPDC beam. Because the laser window has very low transmission, this option has, in principle, the same issue as the other two. There is no alternative, since two modes cannot be combined without loss. In practice however the laser window — perhaps because it is designed for this task — turned out to have much more stable reflection coefficient, sufficient for the stabilization to keep the interferometer phase stable for a few days.

### 5.4.5 Collection and detection of the stabilization light

A similar decision has to be made for the location where we want to collect the stabilization light after it has traversed the interferometer. Here there are two obvious choices: the unused port of the exit PBS, or the reflection from the filter. These are respectively called output 1 and 2 in Figure 5.7. We found the second option to be the best. For the same reasons as described when choosing the input port, we want to chose the collecting port that has the most intensity. In our setup, we found that even after passing through the 1550 nm PM fibers and a 1550 nm HWP, the stabilization light still has mostly the same polarization as the telecom SPDC photons, and therefore exits the interferometer through the same port of the PBS. The best place to collect them is therefore from the filter.

For the detection of the stabilization light, we chose to use single-photon detectors. More specifically, we employ the same type of Si-APD from PerkinElmer used to detect the 842 nm photons. This allowed us to have the lowest amount of light possible for stabilization, which is good for two reasons: it results in less noise for the telecom detectors, and it prevents the stabilization light from heating the PPLN waveguides and changing their phasematching conditions.

### 5.4.6 Finding zero path length difference for the Mach-Zehnder interferometer

For the experiment to work, the two paths through the Mach-Zehnder need to be indistinguishable. Amongst other things, it is required that the two paths through the interferometer have the same length. More precisely, the difference between the two paths must be smaller then the coherence length of the 776 nm photons from the first downconversion. To verify that this is the case, we can send light with a similar coherence length through the interferometer, and maximize the visibility of the observed interference. For this task, it is convenient to use the 776 nm SPDC photons themselves. This can be done in two ways.

The first method uses detections of 776 nm photons. We pump the Sagnac source in one direction only, and add a HWP at 22.5° before the Mach-Zehnder interferometer. The transmission of the 776 nm photons through the Mach-Zehnder interferometer is approximately 10%, leaving plenty of signal at the stabilization detector to observe interference. The position of one of the couplers at the output of the Mach-Zehnder interferometer can then be adjusted to change one of the path lengths so that the interference visibility is maximized. It also useful to make the piezo stage move slowly during the measurement, as it makes the fringes easier to see.

The second method is more complicated, but does not require a HWP before the Mach-Zehnder interferometer. Without that HWP, the Sagnac needs to be pumped in both directions so that photons will travel in each arm of the Mach-Zehnder interferometer. In this configuration, the singles will not show any interference. However, if we look at coincidences between 842 nm photons and 776 nm photons coming out of the Mach-Zehnder interferometer, we can see interference, provided we use the right basis. Indeed, measuring the 842 nm photon in the horizontal basis does not lead to any interference, but measuring it for example in the diagonal basis will lead to interference fringes. This interference can be used to minimize the path length difference between the two arms of the interferometer. Note that the reason we measure the 842 nm photon in the diagonal basis is to erase the information it contains about which way its partner photon with travel through the Mach-Zehnder; this is effectively an implementation of a quantum eraser, employed here as a way of aligning the setup.

### 5.4.7 An example of a stabilization measurement

Here we show some graphs that help to illustrate the operation and performance of the stabilization. These results were taken during and after the measurement of Svetlichny inequality in Chapter 4. In Figure 5.8, we show the position of the piezo stage and the direction of movement of the mechanical motor during the experiment. We see that when the piezo approaches the end of its range, the motor is activated, moving at 10 nm/s, to bring the piezo closer to its middle point.

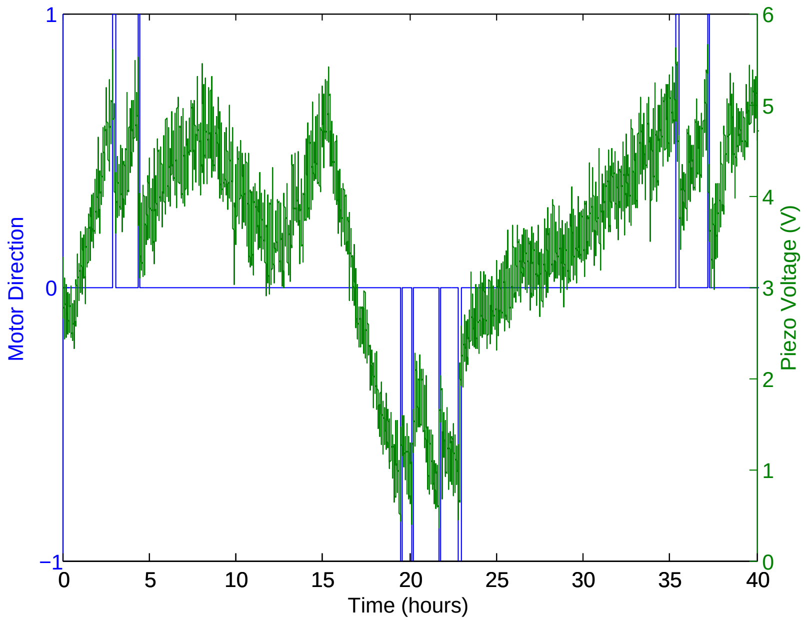

Figure 5.8: Piezo voltage and motor direction during stabilization.

The next two figures, Figure 5.9 and Figure 5.10, show how well the stabilization is keeping the counts stable. In this case, the setpoint was set to $1.0 \times 10^6$ counts per second. The counts stay largely within the range of $0.9 \times 10^6$ to $1.1 \times 10^6$ counts per second, whereas the fringe pattern, if the phase was not stabilized, would have spanned approximately $0.1 \times 10^6$ to $2 \times 10^6$ counts per second.

To check whether the stabilization is truly always staying on one fringe, it is useful to

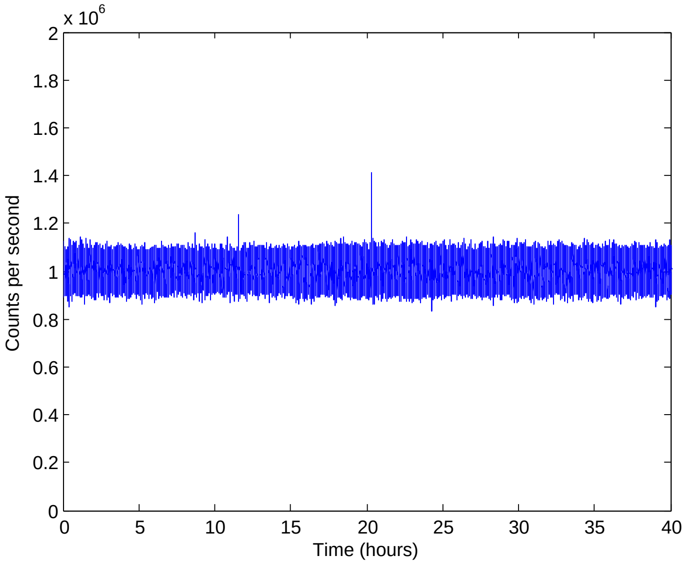

Figure 5.9: Variation of stabilization counts.

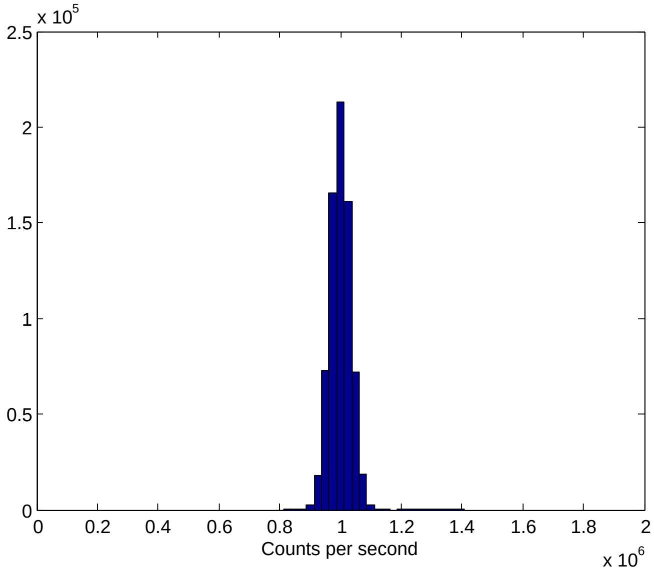

Figure 5.10: Histogram of stabilization counts.

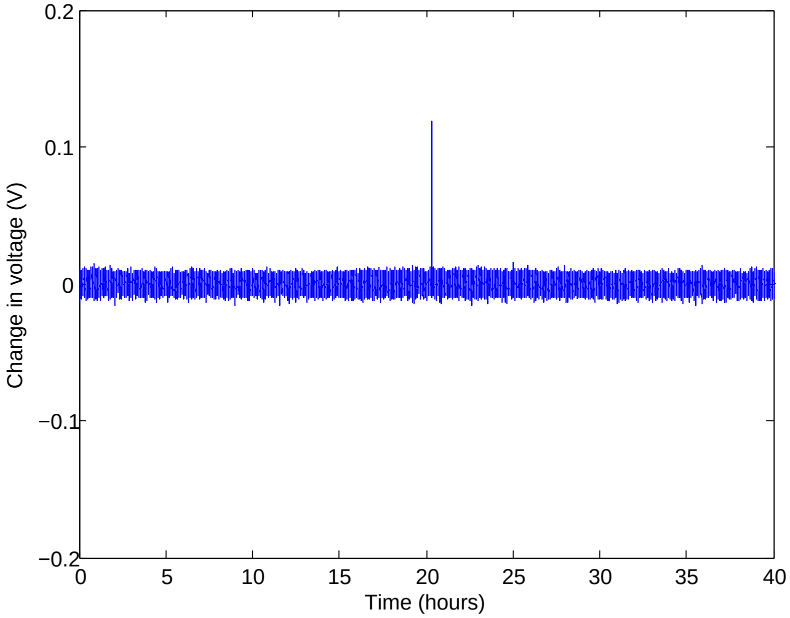

Figure 5.11: Differences between subsequent piezo voltages. The spike is an indication that the stabilization might have skipped a fringe at that point.

look at the difference in voltage between subsequent points. Any sudden change in the position of the piezo could indicate that the stabilization momentarily lost its lock and has skipped a fringe. A graph showing the difference between subsequent piezo positions is shown in Figure 5.11. We can see that a large spike occurs after approximately 20 hours. This is an indication, but not a guarantee, that the piezo might have skipped to the next fringe at that time. Note that the data collection for the Svetlichny inequality measurement in Chapter 4 was stopped before that spike occurred.

## 5.5 Showing polarization entanglement with lower efficiency telecom detectors

In this section, we discuss a similar experiment to the polarization entanglement described in Chapter 4, which was performed before we had access to the nanowire detectors. The

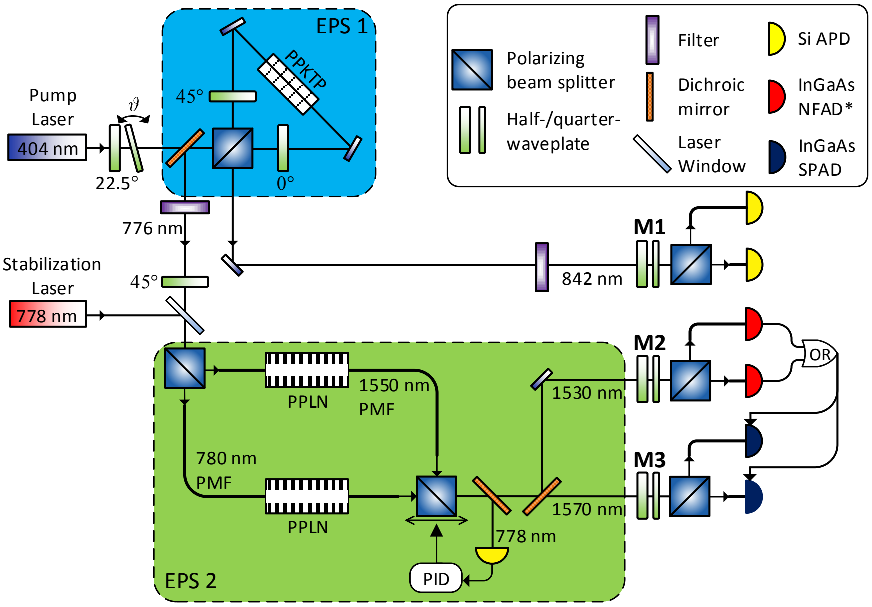

Figure 5.12: Experimental setup for polarization entanglement with NFAD detectors.

setup is shown in Figure 5.12. A combination of free-running NFAD detectors and gated InGaAs SPAD (idQuantique id201) is used, similarly to what was employed for the experiment in Chapter 3. However, because this experiment uses a pair of each types of detectors, an additional "OR" operation is needed. This was implemented with two Ortec NIM-logic modules. A discriminator (ORTEC 935 Quad CFD) was used to discriminate signals from the NFAD and convert them to NIM pulses, and a quad logic unit (ORTEC CO4020 QUAD 4-input Logic) was used to perform the "OR" operation.

Our goal was to show genuine tripartite polarization entanglement, but since we were still using the same detectors as in Chapter 3, we only had 9.5 triplets per hour. Entanglement tests that require a lot of measurements, such as quantum state tomography, were thus not feasible. Instead, we needed an entanglement criterion which was as efficient as possible in the number of measurements. We used an entanglement witness, which allows for entanglement detection using only a limited set of measurements. As was discussed in Section 2.2.2, GHZ states with any number of qubits can be detected using only two local measurements [123]. Recall that for a three qubit state, this entanglement witness is given by Equation 2.14:

$$W = \frac{3}{2} - \sigma_x^{(1)}\sigma_x^{(2)}\sigma_x^{(3)} - \frac{1}{2}\left[\sigma_z^{(1)}\sigma_z^{(2)} + \sigma_z^{(1)}\sigma_z^{(3)} + \sigma_z^{(2)}\sigma_z^{(3)}\right]$$

Measuring a negative value for this observable ensures that the state is genuinely tripartite entangled. This witness has the additional benefit that it can be used to put a lower bound on the fidelity of our state [59]. More precisely, as shown in Appendix B, the fidelity with the target GHZ state is lower bounded by

$$F_{\text{GHZ}} \geq \frac{1 - \langle W \rangle}{2}. \tag{5.1}$$

Just like we did for the experiments described in Chapter 4 (see Figure 4.2), we start by performing a $\sigma_x\sigma_x\sigma_x$ measurement while scanning the phase . The result of this measurement is shown in Figure 5.13. We pick the phase with the best correlation, and start the measurement of the entanglement witness.

We collected data for 20 hours, during which we measured an average of 9.5 triplets per hour. The results are summarized and compared to the expected values in Figure 5.14. Based on these measurements, we calculate the expectation value of the witness to be $\langle W \rangle = -0.68 \pm 0.08$. The system is therefore conclusively entangled by a margin of over 8 standard deviations. Additionally, from equation 5.1, we find a lower bound for the fidelity of $F_{\text{GHZ}} \geq 0.84 \pm 0.04$.

These results show that the high efficiency nanowire detectors were not strictly necessary to observe the presence of polarization entanglement from cascaded down conversion. They do however allow for a much more complete characterization of the state.

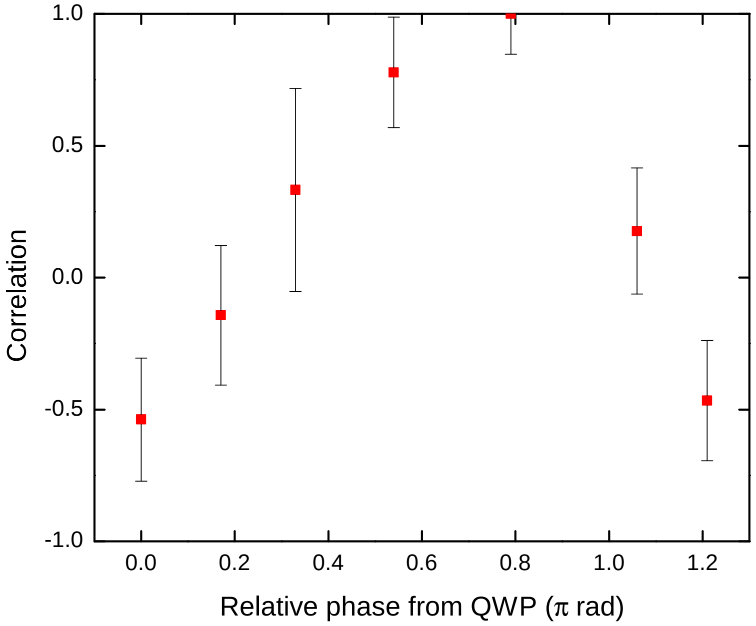

Figure 5.13: Determination of optimal phase for GHZ witness measurement.

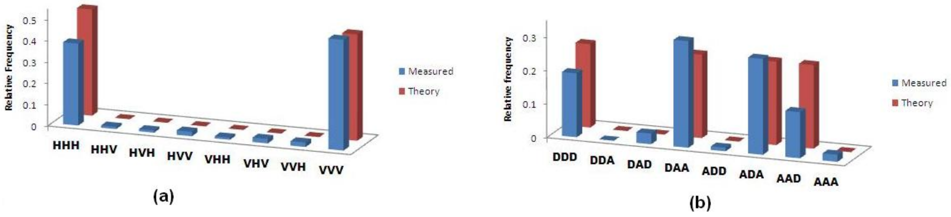

Figure 5.14: Results of GHZ witness measurement. The predicted and measured relative frequencies for a) $\sigma_z^{(1)}\sigma_z^{(2)}\sigma_z^{(3)}$ and b) $\sigma_x^{(1)}\sigma_x^{(2)}\sigma_x^{(3)}$ are shown.

# Chapter 6

# Conclusion and Outlook

In this thesis, we have shown a novel source of tripartite photonic entanglement using cascaded downconversion. This is the first direct source of multi-photon entanglement, meaning that post-selection based on photon detections is not explicitly required by the scheme.

Using new time-bandwidth inequalities that detect genuine tripartite entanglement, we were able to show that the photon triplets produced by this source are energy-time entangled. We then showed polarization-entangled triplets from cascaded downconversion. Our tomographic reconstruction of the state has the highest fidelity for a three-photon GHZ state to date. We also violated the Mermin and Svetlichny inequalities, beating the strongest previous violation for the Svetlichny inequality. Finally, we proved that our state can herald Bell pairs. Our tomographic reconstruction of the heralded Bell pairs showed higher fidelity than previously demonstrated six-photon schemes, and our higher count rates also allowed us to violate a CHSH inequality with the heralded Bell pairs.

Where can we go from here? On the technical side, there are still significant improvements that could be applied to the polarization entanglement source. First, there are manners to improve the fidelity of the state. We know that the main error in our state came from phase errors; this could be due to several different causes. The active stabilization might not be precise enough, and could certainly be improved. It is also possible that the spectra from the two PPLN crystals were not perfectly overlapped, since it was difficult to measure them precisely — particularly because, as discussed earlier, pumping the crystals with a strong laser heats them enough to modify their phasematching. This could perhaps be improved with careful optimization of the crystal temperature. It may also be possible to add spectral filters before the telecom detectors to ensure that only an overlapping portion of the spectrums is detected. Another idea could be to use a waveguide that is not fiber-pigtailed; this might allow for a configuration for the second downconversion which only requires one crystal, such as a double pass or a Sagnac interferometer. Finally, we saw that unbalanced dispersion after the PPLN waveguide could limit the interference visibility. While we tried to address this limitation by adding fiber lengths to compensate the unbalanced dispersion, further improvements may be possible on that front.

Secondly, another interesting direction to improve the source could be to increase the count rates. In the past, these were severely limited by the telecom detectors. but now that we have used the SNSPDs, there is very little improvement left to be made on that front. Of course, for our experiments we were still using a Si-APD with 40% efficiency to detect the 842 nm photons, so there is a factor of 2 to be gained on that side. Switching to detectors capable of higher count rates than the current Si-APDs would also allow us to use a stronger pump laser, which could also lead to higher rates of detected triplets. There is also certainly some room to improve the count rates by optimizing the coupling efficiency of the photons, particularly from the Sagnac source. Beyond that we would have to focus on new materials with better conversion efficiency; any improvement in that direction would directly translate itself to higher count rates.

For the source of heralded Bell pairs, one figure of merit that requires an amelioration is the heralding efficiency: the probability, given a click at the trigger detector, that a Bell pair will be detected by the other two detectors. This is because the production rates of triplets is still low enough that most of the detections at the trigger detector are just dark counts. Therefore, any of the improvements in absolute triplet count rates discussed previously would also improve the heralding efficiency of Bell pairs by the same amount. An additional possibility is to replace the current continuous-wave pump with a pulsed pump. This would provide us with additional timing information about the produced triplets, which would allow us to effectively eliminate a large portion of the dark counts at the trigger detector.

For the energy-time entanglement, our conclusion requires that downconversion respects energy conservation. Although there is nothing suggesting that it does not, and the fact that our Mach-Zehnder interferometer is able to produce polarization entanglement strongly indicates that energy is conserved in downconversion, it is nonetheless true that we were not able to simultaneously show that energy was conserved *and* measure the time-bandwidth uncertainty inequalities in the same experiment. It would therefore be of interest to do an alternative demonstration of the energy-time entanglement. One possible experiment would be a three-photon version of a Franson experiment [81]. This would provide an independent confirmation of the energy-time entanglement of the photon triplets produced by cascaded downconversion, one that would no require any assumptions about energy conservation.

# APPENDICES

# Appendix A

# Producing tripartite entanglement with post-selection

In this appendix we want to discuss the usual method for producing multipartite photonic entanglement [35], and specifically why post-selection is an integral part of the scheme. We use as an example the experiment by Bouwmeester at al. [36] which was the first to show a three-photon GHZ state. However, the principles are the same for other experiments with a larger number of photons.

Consider the setup shown in Figure A.1. The SPDC crystal is chosen and oriented to produce pairs of photons in the state:

$$|\psi\rangle = \frac{1}{\sqrt{2}} \left(|H\rangle_{\mathrm{a}}|V\rangle_{\mathrm{b}} - |V\rangle_{\mathrm{a}}|H\rangle_{\mathrm{b}}\right) \tag{A.1}$$

using Kwiat's single emitter method [27]. The crystal is pumped with a strong pulsed laser, so that the next term in the expansion shown in Equation 2.41 is needed. Its contribution to the state in modes a and b is proportional to:

$$|\psi\rangle \sim \left(\hat{a}^{\dagger}_{H,\mathrm{a}}\hat{a}^{\dagger}_{V,\mathrm{b}} + \hat{a}^{\dagger}_{V,\mathrm{a}}\hat{a}^{\dagger}_{H,\mathrm{b}}\right)^2 |\mathrm{vac}\rangle, \tag{A.2}$$

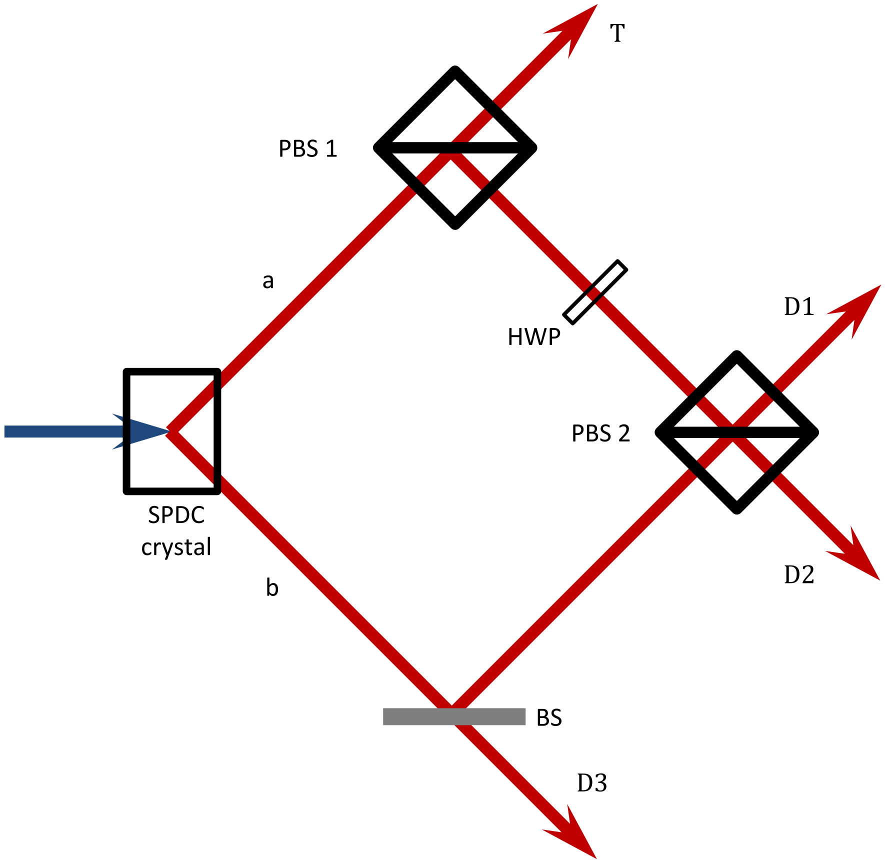

Figure A.1: Double pairs from a single emitter setup used for the first production of GHZ states. An SPDC source is pumped with a pulsed laser to produce entangled pairs. Detectors are placed in each of the output modes T, D1, D2 and D3. In the case where two pairs are produced at the same time, and by post-selecting on the cases where all four detectors get a detection, a GHZ state is produced. This figure and its caption were originally published in my MSc thesis [31].

where and a and b indicate the mode, and $H$ and $V$ indicate the polarization of the created photons. In the setup, each of these creation operators are modified according to:

$$\begin{aligned}\hat{a}^\dagger_{H,\mathrm{a}} &\rightarrow \hat{a}^\dagger_{H,\mathrm{T}} &\text{(A.3)}\\ \hat{a}^\dagger_{V,\mathrm{b}} &\rightarrow \frac{1}{\sqrt{2}}\left(\hat{a}^\dagger_{V,2}+\hat{a}^\dagger_{V,3}\right) &\text{(A.4)}\\ \hat{a}^\dagger_{V,\mathrm{a}} &\rightarrow \frac{1}{\sqrt{2}}\left(\hat{a}^\dagger_{V,1}+\hat{a}^\dagger_{H,2}\right) &\text{(A.5)}\\ \hat{a}^\dagger_{H,\mathrm{b}} &\rightarrow \frac{1}{\sqrt{2}}\left(\hat{a}^\dagger_{H,1}+\hat{a}^\dagger_{H,3}\right). &\text{(A.6)}\end{aligned}$$

Substituting these into Equation A.2 yields:

$$|\psi\rangle \sim \left[\hat{a}^\dagger_{H,\mathrm{T}}\cdot\frac{1}{\sqrt{2}}\left(\hat{a}^\dagger_{V,2}+\hat{a}^\dagger_{V,3}\right)+\frac{1}{\sqrt{2}}\left(\hat{a}^\dagger_{V,1}+\hat{a}^\dagger_{H,2}\right)\cdot\frac{1}{\sqrt{2}}\left(\hat{a}^\dagger_{H,1}+\hat{a}^\dagger_{H,3}\right)\right]^2|\mathrm{vac}\rangle. \tag{A.7}$$

We will not completely expand this equation here; it is quite a long and complicated expression which is not particularly instructive for our purpose. The important point is that the state obtained by expanding Equation A.7 *is not* a GHZ state. It is something a lot more complicated. The trick then, and the key to this scheme, is to only keep the terms that have one photon going in each output mode (1,2,3 and T). After renormalization, this results in:

$$|\psi\rangle = \frac{1}{\sqrt{2}}\left(\hat{a}^\dagger_{H,\mathrm{T}}\hat{a}^\dagger_{V,1}\hat{a}^\dagger_{V,2}\hat{a}^\dagger_{H,3}+\hat{a}^\dagger_{H,\mathrm{T}}\hat{a}^\dagger_{H,1}\hat{a}^\dagger_{H,2}\hat{a}^\dagger_{V,3}\right)|\mathrm{vac}\rangle. \tag{A.8}$$

By applying the creation operators to the vacuum we get the state:

$$|\psi\rangle = \frac{1}{\sqrt{2}}|H\rangle_T\left(|V\rangle_1|V\rangle_2|H\rangle_3+|H\rangle_1|H\rangle_2|V\rangle_3\right), \tag{A.9}$$

which is the desired GHZ state if the trigger mode is traced out. But as we mentioned before, this is only the quantum state in cases where there was a photon in all four output modes. The selection of only these cases is called *"post-selection"*.

# Appendix B

# Obtaining a fidelity bound from a GHZ entanglement witness

In this appendix, we will show that the two-setting entanglement witness from Tóth and Gühne [123] can be used to bound the fidelity of a state with a GHZ state [59]. We treat the three-particle version of their witness, given by:

$$W = \frac{3}{2} - \sigma_x^{(1)}\sigma_x^{(2)}\sigma_x^{(3)} - \frac{1}{2}\left[\sigma_z^{(1)}\sigma_z^{(2)} + \sigma_z^{(1)}\sigma_z^{(3)} + \sigma_z^{(2)}\sigma_z^{(3)}\right]. \tag{B.1}$$

It is useful to write the witness in the GHZ basis, which is constituted of the following set of orthonormal state vectors:

$$\begin{aligned} |\mathrm{GHZ}^{\pm}\rangle = |\Delta_0^{\pm}\rangle &= \frac{1}{\sqrt{2}}\left(|HHH\rangle \pm |VVV\rangle\right) \\ |\Delta_1^{\pm}\rangle &= \frac{1}{\sqrt{2}}\left(|VHH\rangle \pm |HVV\rangle\right) \\ |\Delta_2^{\pm}\rangle &= \frac{1}{\sqrt{2}}\left(|HVH\rangle \pm |VHV\rangle\right) \\ |\Delta_3^{\pm}\rangle &= \frac{1}{\sqrt{2}}\left(|HHV\rangle \pm |VVH\rangle\right). \end{aligned} \tag{B.2}$$

In the notation of the basis state, the index indicates which of the three particles has a different polarization than the other two; the "0" subscript implies that they are all the same. To write the witness in the GHZ basis, we can first write it in the computational basis, and then apply the necessary transformation. The matrix representation of $W$ in the computational basis is:

$$[W]_{\text{comp}} = \begin{pmatrix} 0 & 0 & 0 & 0 & 0 & 0 & 0 & -1 \\ 0 & 2 & 0 & 0 & 0 & 0 & -1 & 0 \\ 0 & 0 & 2 & 0 & 0 & -1 & 0 & 0 \\ 0 & 0 & 0 & 2 & -1 & 0 & 0 & 0 \\ 0 & 0 & 0 & -1 & 2 & 0 & 0 & 0 \\ 0 & 0 & -1 & 0 & 0 & 2 & 0 & 0 \\ 0 & -1 & 0 & 0 & 0 & 0 & 2 & 0 \\ -1 & 0 & 0 & 0 & 0 & 0 & 0 & 0 \end{pmatrix}. \tag{B.3}$$

The square brackets with the "comp" subscript indicate that the operator is written in the computational basis. By using the computational basis decomposition of the states given by Equation B.2 as columns in a matrix $T$, we obtain the transformation matrix which takes states from the GHZ basis to the computational basis:

$$T = \begin{pmatrix} 1 & 1 & 0 & 0 & 0 & 0 & 0 & 0 \\ 0 & 0 & 0 & 0 & 0 & 0 & 1 & 1 \\ 0 & 0 & 0 & 0 & 1 & 1 & 0 & 0 \\ 0 & 0 & 1 & -1 & 0 & 0 & 0 & 0 \\ 0 & 0 & 1 & 1 & 0 & 0 & 0 & 0 \\ 0 & 0 & 0 & 0 & 1 & -1 & 0 & 0 \\ 0 & 0 & 0 & 0 & 0 & 0 & 1 & -1 \\ 1 & -1 & 0 & 0 & 0 & 0 & 0 & 0 \end{pmatrix}. \tag{B.4}$$

We use this transformation matrix to write $W$ in the GHZ basis.

$$[W]_{\text{GHZ}} = T^{-1}[W]_{\text{Comp}}T = \begin{pmatrix} -1 & 0 & 0 & 0 & 0 & 0 & 0 & 0 \\ 0 & 1 & 0 & 0 & 0 & 0 & 0 & 0 \\ 0 & 0 & 1 & 0 & 0 & 0 & 0 & 0 \\ 0 & 0 & 0 & 3 & 0 & 0 & 0 & 0 \\ 0 & 0 & 0 & 0 & 1 & 0 & 0 & 0 \\ 0 & 0 & 0 & 0 & 0 & 3 & 0 & 0 \\ 0 & 0 & 0 & 0 & 0 & 0 & 1 & 0 \\ 0 & 0 & 0 & 0 & 0 & 0 & 0 & 3 \end{pmatrix}. \tag{B.5}$$

Notice that in the GHZ basis, the witness is diagonal and only the first element is negative. These are the key points which allow us to use the witness to put a bound on the fidelity with the GHZ state.

We now consider a quantum state with density matrix $\rho$. We will call the element in the i-th row and j-th collum of the GHZ decomposition of this density matrix $\rho_{i,j}$. Combining this with Equation B.5, it is easy to see that the expectation value of the witness for this state is given by:

$$\langle W\rangle_\rho = \text{Tr}(W\rho) = -\rho_{1,1} + \rho_{2,2} + \rho_{3,3} + 3\rho_{4,4} + \rho_{5,5} + 3\rho_{6,6} + \rho_{7,7} + 3\rho_{8,8}. \tag{B.6}$$

We know that $\text{Tr}(\rho) = 1$, so $\sum_{i=1}^{8} \rho_{i,i} = 1$. This allows us to simplify the last equation to:

$$\langle W\rangle_\rho = 1 - 2\rho_{1,1} + 2\rho_{4,4} + 2\rho_{6,6} + 2\rho_{8,8}. \tag{B.7}$$

Therefore, we have:

$$\frac{1 - \langle W\rangle_\rho}{2} = \rho_{1,1} - \rho_{4,4} - \rho_{6,6} - \rho_{8,8} \leq \rho_{1,1}, \tag{B.8}$$

by using the fact that the diagonal elements of a density matrix are non-negative. The $\rho_{1,1}$ term which is left is exactly the fidelity of the state $\rho$ with $|\mathrm{GHZ}^+\rangle$. Indeed, this fidelity is given by $F = \langle \mathrm{GHZ}^+|\rho|\mathrm{GHZ}^+\rangle = \rho_{1,1}$. We thus have the desired result:

$$F \geq \frac{1 - \langle W \rangle_\rho}{2} \tag{B.9}$$

Therefore, with only two measurement settings we can measure the expectation value of $W$, which allows us not only to check for entanglement, and also to put a bound lower on the fidelity of $\rho$ with the $|\mathrm{GHZ}^+\rangle$ state.

# Bibliography

[1] P. W. Shor, Polynomial-Time Algorithms for Prime Factorization and Discrete Logarithms on a Quantum Computer. *arXiv:quant-ph/9508027* (1995). 1

[2] M. A. Nielsen, I. L. Chuang, *Quantum Computation and Quantum Information* (Cambridge University Press, 2000). 1, 28

[3] E. Knill, R. Laflamme, G. Milburn, A scheme for efficient quantum computation with linear optics. *Nature* **409**, 46–52 (2001). 1, 4, 58

[4] C. H. Bennett, G. Brassard, *Proceedings of the IEEE International Conference on Computers, Systems and Signal Processing* (IEEE Press, New York, 1984), pp. 175–179. 1

[5] A. K. Ekert, Quantum cryptography based on Bell's theorem. *Phys. Rev. Lett.* **67**, 661–663 (1991). 1, 28

[6] K. Goda, O. Miyakawa, E. E. Mikhailov, S. Saraf, R. Adhikari, K. Mckenzie, R. Ward, S. Vass, A. J. Weinstein, N. Mavalvala, A quantum-enhanced prototype gravitational-wave detector. *Nature Physics* **4**, 472 (2008). 1, 28

[7] B. Hage, A. Samblowski, J. DiGuglielmo, A. Franzen, J. Fiurasek, R. Schnabel, Preparation of distilled and purified continuous-variable entangled states. *Nature Physics* **4**, 915–918 (2008). 1, 28

[8] J. Ye, H. Kimble, H. Katori, Quantum state engineering and precision metrology using state-insensitive light traps. *Science* **320**, 1734–1738 (2008). 1, 28

[9] T. D. Ladd, F. Jelezko, R. Laflamme, Y. Nakamura, C. Monroe, J. L. O'Brien, Quantum computers. *Nature* **464**, 45–53 (2010). 1

[10] E. Schrödinger, Discussion of Probability Relations between Separated Systems. *Proceedings of the Cambridge Philosophical Society* **31**, 555 (1935). 2

[11] A. Einstein, B. Podolsky, N. Rosen, Can quantum-mechanical description of physical reality be considered complete? *Phys. Rev.* **47**, 777–780 (1935). 2, 13, 28

[12] J. S. Bell, On the Einstein Podolsky Rosen paradox. *Physics* **1**, 195–200 (1964). 3, 28

[13] J. F. Clauser, M. A. Horne, A. Shimony, R. A. Holt, Proposed experiment to test local hidden-variable theories. *Phys. Rev. Lett.* **23**, 880–884 (1969). 3, 69

[14] S. J. Freedman, J. F. Clauser, Experimental test of local hidden-variable theories. *Phys. Rev. Lett.* **28**, 938–941 (1972). 3

[15] A. Aspect, P. Grangier, G. Roger, Experimental tests of realistic local theories via Bell's theorem. *Phys. Rev. Lett.* **47**, 460–463 (1981). 3

[16] A. Aspect, J. Dalibard, G. Roger, Experimental test of Bell's inequalities using time-varying analyzers. *Phys Rev Lett* **49**, 1804–1807 (1982). 3

[17] A. Aspect, P. Grangier, G. Roger, Experimental realization of Einstein-Podolsky-Rosen-Bohm gedankenexperiment: A new violation of Bell's inequalities. *Phys. Rev. Lett.* **49**, 91–94 (1982). 3, 28

[18] K. Edamatsu, Entangled photons: Generation, observation and characterization. *Japanese Journal of Applied Physics* **46**, 7175–7187 (2007). 3, 22

[19] S. E. Harris, M. K. Oshman, R. L. Byer, Observation of tunable optical parametric fluorescence. *Phys. Rev. Lett.* **18**, 732–734 (1967). 3

[20] D. Magde, H. Mahr, Study in Ammonium Dihydrogen Phosphate of Spontaneous Parametric Interaction Tunable from 4400 to 16 000 Å. *Phys. Rev. Lett.* **18**, 905–907 (1967). 3

[21] B. Y. Zel'Dovich, D. N. Klyshko, Field Statistics in Parametric Luminescence. *ZhETF Pisma Redaktsiiu* **9**, 69 (1969). 3

[22] D. C. Burnham, D. L. Weinberg, Observation of simultaneity in parametric production of optical photon pairs. *Phys. Rev. Lett.* **25**, 84–87 (1970). 3

[23] L. Mandel, Quantum effects in one-photon and two-photon interference. *Rev. Mod. Phys.* **71**, S274–S282 (1999). 3

[24] Z. Y. Ou, L. Mandel, Violation of Bell's inequality and classical probability in a two-photon correlation experiment. *Phys. Rev. Lett.* **61**, 50–53 (1988). 3

[25] Y. H. Shih, C. O. Alley, New type of Einstein-Podolsky-Rosen-Bohm experiment using pairs of light quanta produced by optical parametric down conversion. *Phys. Rev. Lett.* **61**, 2921–2924 (1988). 3

[26] T. E. Kiess, Y. H. Shih, A. V. Sergienko, C. O. Alley, Einstein-Podolsky-Rosen-Bohm experiment using pairs of light quanta produced by type-ii parametric down-conversion. *Phys. Rev. Lett.* **71**, 3893–3897 (1993). 3

[27] P. G. Kwiat, K. Mattle, H. Weinfurter, A. Zeilinger, A. V. Sergienko, Y. Shih, New high-intensity source of polarization-entangled photon pairs. *Phys. Rev. Lett.* **75**, 4337–4341 (1995). 3, 22, 58, 103

[28] P. G. Kwiat, E. Waks, A. G. White, I. Appelbaum, P. H. Eberhard, Ultrabright source of polarization-entangled photons. *Phys. Rev. A* **60**, R773–R776 (1999). 3, 22, 58

[29] M. Fiorentino, G. Messin, C. E. Kuklewicz, F. N. C. Wong, J. H. Shapiro, Generation of ultrabright tunable polarization entanglement without spatial, spectral, or temporal constraints. *Phys. Rev. A* **69**, 041801 (2004). 3

[30] T. Kim, M. Fiorentino, F. N. C. Wong, Phase-stable source of polarization-entangled photons using a polarization Sagnac interferometer. *Phys. Rev. A* **73**, 012316 (2006). 3, 22, 58, 60

[31] D. R. Hamel, Realization of novel entangled photon sources using periodically poled materials (2010). 3, 11, 12, 22, 24, 25, 26, 78, 86, 104

[32] G. Svetlichny, Distinguishing three-body from two-body nonseparability by a Bell-type inequality. *Phys. Rev. D* **35**, 3066–3069 (1987). 4, 62, 65

[33] N. D. Mermin, Extreme quantum entanglement in a superposition of macroscopically distinct states. *Phys. Rev. Lett.* **65**, 1838–1840 (1990). 4, 62

[34] D. M. Greenberger, M. A. Horne, A. Shimony, A. Zeilinger, Bell's theorem without inequalities. *American Journal of Physics* **58**, 1131–1143 (1990). 4, 5, 59

[35] A. Zeilinger, M. A. Horne, H. Weinfurter, M. Żukowski, Three-particle entanglements from two entangled pairs. *Phys. Rev. Lett.* **78**, 3031–3034 (1997). 4, 5, 58, 103

[36] D. Bouwmeester, J.-W. Pan, M. Daniell, H. Weinfurter, A. Zeilinger, Observation of three-photon Greenberger-Horne-Zeilinger entanglement. *Phys. Rev. Lett.* **82**, 1345–1349 (1999). 4, 58, 103

[37] J. Pan, M. Daniell, S. Gasparoni, G. Weihs, A. Zeilinger, Experimental demonstration of four-photon entanglement and high-fidelity teleportation. *Phys. Rev. Lett.* **86**, 4435–4438 (2001). 4, 58

[38] Z. Zhao, Y. Chen, A. Zhang, T. Yang, H. Briegel, J. Pan, Experimental demonstration of five-photon entanglement and open-destination teleportation. *Nature* **430**, 54–58 (2004). 4

[39] C.-Y. Lu, X.-Q. Zhou, O. Gühne, W.-B. Gao, J. Zhang, Z.-S. Yuan, A. Goebel, T. Yang, J.-W. Pan, Experimental entanglement of six photons in graph states. *Nature Physics* **3**, 91–95 (2007). 4, 58

[40] X.-C. Yao, T.-X. Wang, P. Xu, H. Lu, G.-S. Pan, X.-H. Bao, C.-Z. Peng, C.-Y. Lu, Y.-A. Chen, J.-W. Pan, Observation of eight-photon entanglement. *Nature Photonics* **6**, 225–228 (2012). 4, 58

[41] P. Walther, K. J. Resch, T. Rudolph, E. Schenck, H. Weinfurter, V. Vedral, M. Aspelmeyer, A. Zeilinger, Experimental one-way quantum computing. *Nature* **434**, 169–176 (2005). 4

[42] M. Eibl, N. Kiesel, M. Bourennane, C. Kurtsiefer, H. Weinfurter, Experimental realization of a three-qubit entangled $W$ state. *Phys. Rev. Lett.* **92**, 077901 (2004). 4, 58

[43] R. Prevedel, G. Cronenberg, M. S. Tame, M. Paternostro, P. Walther, M. S. Kim, A. Zeilinger, Experimental realization of dicke states of up to six qubits for multiparty quantum networking. *Phys. Rev. Lett.* **103**, 020503 (2009). 4

[44] T. C. Ralph, N. K. Langford, T. B. Bell, A. G. White, Linear optical controlled-not gate in the coincidence basis. *Phys. Rev. A* **65**, 062324 (2002). 5

[45] K. Banaszek, P. L. Knight, Quantum interference in three-photon down-conversion. *Phys. Rev. A* **55**, 2368–2375 (1997). 5

[46] M. Corona, K. Garay-Palmett, A. B. U'Ren, Experimental proposal for the generation of entangled photon triplets by third-order spontaneous parametric downconversion in optical fibers. *Opt. Lett.* **36**, 190–192 (2011). 5, 36

[47] A. Dot, Etude théorique et expérimentale de la génération et des corrélations quantiques de photons triplets générés par interaction non linéaire d'ordre trois, Ph.D. thesis, Université de Grenoble (2011). 5

[48] A. Dot, A. Borne, B. Boulanger, P. Segonds, C. Félix, K. Bencheikh, J. A. Levenson, Energetic and spectral properties of triple photon downconversion in a phase-matched ktiopo4 crystal. *Opt. Lett.* **37**, 2334–2336 (2012). 5

[49] T. E. Keller, M. H. Rubin, Y. Shih, L.-A. Wu, Theory of the three-photon entangled state. *Phys. Rev. A* **57**, 2076–2079 (1998). 5, 29

[50] N. Sangouard, B. Sanguinetti, N. Curtz, N. Gisin, R. Thew, H. Zbinden, Faithful entanglement swapping based on sum-frequency generation. *Phys. Rev. Lett.* **106**, 120403 (2011). 5, 36

[51] T. Guerreiro, E. Pomarico, B. Sanguinetti, N. Sangouard, J. S. Pelc, C. Langrock, M. M. Fejer, H. Zbinden, R. T. Thew, N. Gisin, Interaction of independent single photons based on integrated nonlinear optics. *Nature Communications* **4**, 2324 (2013). 5

[52] J. Persson, T. Aichele, V. Zwiller, L. Samuelson, O. Benson, Three-photon cascade from single self-assembled InP quantum dots. *Phys. Rev. B* **69**, 233314 (2004). 5

[53] S. N. Gupta, Multiple photon production in electron-positron annihilation. *Phys. Rev.* **96**, 1453 (1954). 5

[54] E. Lötstedt, U. D. Jentschura, Triple compton effect: A photon splitting into three upon collision with a free electron. *Phys. Rev. Lett.* **108**, 233201 (2012). 5

[55] T. Zhong, F. N. C. Wong, T. D. Roberts, P. Battle, High performance photon-pair source based on a fiber-coupled periodically poled ktiopo4 waveguide: erratum. *Opt. Express* **18**, 20114–20114 (2010). 6

[56] H. Hübel, D. R. Hamel, A. Fedrizzi, S. Ramelow, K. J. Resch, T. Jennewein, Direct generation of photon triplets using cascaded photon-pair sources. *Nature* **466**, 601–603 (2010). 6, 28, 33, 59

[57] W. Dür, J. I. Cirac, R. Tarrach, Separability and distillability of multiparticle quantum systems. *Phys. Rev. Lett.* **83**, 3562–3565 (1999). 8, 29, 37, 38

[58] M. Bourennane, M. Eibl, C. Kurtsiefer, S. Gaertner, H. Weinfurter, O. Gühne, P. Hyllus, D. Bruß, M. Lewenstein, A. Sanpera, Experimental detection of multipartite entanglement using witness operators. *Phys. Rev. Lett.* **92**, 087902 (2004). 8, 29, 37, 38

[59] O. Gühne, G. Tóth, Entanglement detection. *Physics Reports* **474**, 1 – 75 (2009). 11, 12, 97, 106

[60] Z. Hradil, Quantum-state estimation. *Phys. Rev. A* **55**, R1561–R1564 (1997). 11

[61] D. F. V. James, P. G. Kwiat, W. J. Munro, A. G. White, Measurement of qubits. *Phys. Rev. A* **64**, 052312 (2001). 11, 62

[62] M. Horodecki, P. Horodecki, R. Horodecki, Separability of mixed states: necessary and sufficient conditions. *Physics Letters A* **223**, 1–8 (1996). 12

[63] D. M. Greenberger, M. A. Horne, A. Zeilinger, *Bell's Theorem, Quantum Theory, and Conceptions of the Universe*, no. 73-76 (Kluwer Academics, The Netherlands, 1989). 13, 36, 58, 62

[64] L.-M. Duan, G. Giedke, J. I. Cirac, P. Zoller, Inseparability criterion for continuous variable systems. *Phys. Rev. Lett.* **84**, 2722–2725 (2000). 14

[65] P. van Loock, A. Furusawa, Detecting genuine multipartite continuous-variable entanglement. *Phys. Rev. A* **67**, 052315 (2003). 16, 29, 36, 38, 40, 46

[66] J. Lavoie, R. Kaltenbaek, K. J. Resch, Experimental violation of Svetlichny's inequality. *New Journal of Physics* **11**, 073051 (2009). 16, 18, 62

[67] C. K. Hong, L. Mandel, Theory of parametric frequency down conversion of light. *Phys. Rev. A* **31**, 2409–2418 (1985). 19

[68] Z. Y. Ou, L. J. Wang, L. Mandel, Vacuum effects on interference in two-photon down conversion. *Phys. Rev. A* **40**, 1428–1435 (1989). 19

[69] R. Ghosh, C. K. Hong, Z. Y. Ou, L. Mandel, Interference of two photons in parametric down conversion. *Phys. Rev. A* **34**, 3962–3968 (1986). 21

[70] A. V. Burlakov, M. V. Chekhova, O. A. Karabutova, D. N. Klyshko, S. P. Kulik, Polarization state of a biphoton: Quantum ternary logic. *Phys. Rev. A* **60**, R4209–R4212 (1999). 22

[71] Y.-H. Kim, M. V. Chekhova, S. P. Kulik, M. H. Rubin, Y. Shih, Interferometric Bell-state preparation using femtosecond-pulse-pumped spontaneous parametric down-conversion. *Phys. Rev. A* **63**, 062301 (2001). 22

[72] R. W. Boyd, *Nonlinear Optics* (Academic Press, 2008), third edn. 23

[73] J. A. Armstrong, N. Bloembergen, J. Ducuing, P. S. Pershan, Interactions between light waves in a nonlinear dielectric. *Phys. Rev.* **127**, 1918–1939 (1962). 24

[74] M. Yamada, N. Nada, M. Saitoh, K. Watanabe, First order quasi phase matched LiNbO3 waveguide periodically poled by applying an external field for efficient blue second harmonic generation. *Applied Physics Letters* **62**, 435 –436 (1993). 25

[75] D. S. Hum, M. M. Fejer, Quasi-phasematching. *Comptes Rendus Physique* **8**, 180 – 198 (2007). Recent advances in crystal optics. 25

[76] H.-J. Briegel, W. Dür, J. I. Cirac, P. Zoller, Quantum repeaters: The role of imperfect local operations in quantum communication. *Phys. Rev. Lett.* **81**, 5932–5935 (1998). 28, 59

[77] T. Monz, P. Schindler, J. T. Barreiro, M. Chwalla, D. Nigg, W. A. Coish, M. Harlander, W. Hänsel, M. Hennrich, R. Blatt, 14-qubit entanglement: Creation and coherence. *Phys. Rev. Lett.* **106**, 130506 (2011). 28

[78] T. Aoki, N. Takei, H. Yonezawa, K. Wakui, T. Hiraoka, A. Furusawa, P. van Loock, Experimental creation of a fully inseparable tripartite continuous-variable state. *Phys. Rev. Lett.* **91**, 080404 (2003). 28

[79] A. S. Coelho, F. A. S. Barbosa, K. N. Cassemiro, A. S. Villar, M. Martinelli, P. Nussenzveig, Three-Color Entanglement. *Science* **326**, 823– (2009). 28

[80] T. E. Keller, M. H. Rubin, Theory of two-photon entanglement for spontaneous parametric down-conversion driven by a narrow pump pulse. *Phys. Rev. A* **56**, 1534–1541 (1997). 28

[81] J. Franson, Bell inequality for position and time. *Phys. Rev. Lett.* **62**, 2205–2208 (1989). 28, 31, 36, 49, 101

[82] P. G. Kwiat, A. M. Steinberg, R. Y. Chiao, High-visibility interference in a Bell-inequality experiment for energy and time. *Phys. Rev. A* **47**, 2472–2475 (1993). 28, 31, 36, 49

[83] M. V. Fedorov, M. A. Efremov, A. E. Kazakov, K. W. Chan, C. K. Law, J. H. Eberly, Spontaneous emission of a photon: Wave-packet structures and atom-photon entanglement. *Physical Review A* **72**, 032110 (2005). 30

[84] J. Sun, B. J. S. Gale, D. T. Reid, Testing the energy conservation law in an optical parametric oscillator using phase-controlled femtosecond pulses. *Optics Express* **15**, 4378–4384 (2007). 31

[85] T. Ikegami, S. Slyusarev, S.-I. Ohshima, E. Sakuma, Accuracy of an optical parametric oscillator as an optical frequency divider. *Optics Communications* **127**, 69–72 (1996). 31

[86] J. C. Howell, R. S. Bennink, S. J. Bentley, R. W. Boyd, Realization of the einstein-podolsky-rosen paradox using momentum- and position-entangled photons from spontaneous parametric down conversion. *Phys. Rev. Lett.* **92**, 210403 (2004). 36

[87] R. J. Collins, R. H. Hadfield, G. S. Buller, Commentary: New developments in single photon detection in the short wavelength infrared regime. *Journal of Nanophotonics* **4**, 040301 (2010). 36

[88] S. Richard, K. Bencheikh, B. Boulanger, J. A. Levenson, Semiclassical model of triple photons generation in optical fibers. *Opt. Lett.* **36**, 3000–3002 (2011). 36

[89] N. K. Langford, S. Ramelow, R. Prevedel, W. J. Munro, G. J. Milburn, A. Zeilinger, Efficient quantum computing using coherent photon conversion. *Nature* **478**, 360–363 (2011). 36, 71

[90] Z. Yan, D. R. Hamel, A. K. Heinrichs, X. Jiang, M. A. Itzler, T. Jennewein, An ultra low noise telecom wavelength free running single photon detector using negative feedback avalanche diode. *Review of Scientific Instruments* **83** (2012). 44

[91] D. N. Klyshko, Coherent photon decay in a nonlinear medium. *JETP Lett.* **6**, 23–25 (1967). 49

[92] H. Vahlbruch, M. Mehmet, S. Chelkowski, B. Hage, A. Franzen, N. Lastzka, S. Goßler, K. Danzmann, R. Schnabel, Observation of squeezed light with 10-db quantum-noise reduction. *Phys Rev Lett* **100**, 033602–4 (2008). 49

[93] P. Kok, W. J. Munro, K. Nemoto, T. C. Ralph, J. P. Dowling, G. J. Milburn, Linear optical quantum computing with photonic qubits. *Rev. Mod. Phys.* **79**, 135–174 (2007). 58

[94] J.-W. Pan, Z.-B. Chen, C.-Y. Lu, H. Weinfurter, A. Zeilinger, M. Żukowski, Multiphoton entanglement and interferometry. *Rev. Mod. Phys.* **84**, 777–838 (2012). 58

[95] M. Żukowski, A. Zeilinger, M. A. Horne, A. K. Ekert, "event-ready-detectors" bell experiment via entanglement swapping. *Phys. Rev. Lett.* **71**, 4287–4290 (1993). 59

[96] P. Kok, S. L. Braunstein, Limitations on the creation of maximal entanglement. *Phys. Rev. A* **62**, 064301 (2000). 59, 67

[97] A. Cabello, F. Sciarrino, Loophole-free bell test based on local precertification of photon's presence. *Phys. Rev. X* **2**, 021010 (2012). 59, 71

[98] T. B. Pittman, B. C. Jacobs, J. D. Franson, Probabilistic quantum logic operations using polarizing beam splitters. *Phys. Rev. A* **64**, 062311 (2001). 59

[99] D. E. Browne, T. Rudolph, Resource-efficient linear optical quantum computation. *Phys. Rev. Lett.* **95**, 010501 (2005). 59

[100] G. M. D'Ariano, M. Rubin, M. F. Sacchi, Y. Shih, Quantum Tomography of the GHZ State. *Fortschritte der Physik* **48**, 599–603 (2000). 59

[101] H. Hübel, D. R. Hamel, K. J. Resch, T. Jennewein, *AIP Conference Proceedings* (2011), vol. 1363, pp. 331–334. 59, 60

[102] L. K. Shalm, D. R. Hamel, Z. Yan, C. Simon, K. J. Resch, T. Jennewein, Three-photon energy-time entanglement. *Nature Physics* **9**, 19–22 (2013). 59, 71

[103] F. Marsili, V. B. Verma, J. A. Stern, S. Harrington, A. E. Lita, T. Gerrits, I. Vayshenker, B. Baek, M. D. Shaw, R. P. Mirin, S. W. Nam, Detecting single infrared photons with 93% system efficiency. *Nature Photonics* **7**, 210–214 (2013). 59

[104] A. Fedrizzi, T. Herbst, A. Poppe, T. Jennewein, A. Zeilinger, A wavelength-tunable fiber-coupled source of narrowband entangled photons. *Opt. Express* **15**, 15377–15386 (2007). 60

[105] I. Herbauts, B. Blauensteiner, A. Poppe, T. Jennewein, H. Hübel, Demonstration of active routing of entanglement in a multi-user network. *Opt. Express* **21**, 29013–29024 (2013). 60

[106] H.-X. Lu, J.-Q. Zhao, X.-Q. Wang, L.-Z. Cao, Experimental demonstration of tripartite entanglement versus tripartite nonlocality in three-qubit Greenberger-Horne-Zeilinger˘class states. *Phys. Rev. A* **84**, 012111 (2011). 62

[107] G. Tóth, O. Gühne, M. Seevinck, J. Uffink, Addendum to "sufficient conditions for three-particle entanglement and their tests in recent experiments". *Phys. Rev. A* **72**, 014101 (2005). 62, 65

[108] J. L. Cereceda, Three-particle entanglement versus three-particle nonlocality. *Phys. Rev. A* **66**, 024102 (2002). 62, 65

[109] M. Seevinck, J. Uffink, Sufficient conditions for three-particle entanglement and their tests in recent experiments. *Phys. Rev. A* **65**, 012107 (2001). 65

[110] D. Collins, N. Gisin, S. Popescu, D. Roberts, V. Scarani, Bell-type inequalities to detect true $n$-body nonseparability. *Phys. Rev. Lett.* **88**, 170405 (2002). 65

[111] J.-D. Bancal, N. Gisin, Y.-C. Liang, S. Pironio, Device-independent witnesses of genuine multipartite entanglement. *Phys. Rev. Lett.* **106**, 250404 (2011). 65

[112] J.-D. Bancal, J. Barrett, N. Gisin, S. Pironio, Definitions of multipartite nonlocality. *Phys. Rev. A* **88**, 014102 (2013). 65

[113] S. Barz, G. Cronenberg, A. Zeilinger, P. Walther, Heralded generation of entangled photon pairs. *Nature Photonics* **4**, 553–556 (2010). 67, 69

[114] C. Wagenknecht, C.-M. Li, A. Reingruber, X.-H. Bao, A. Goebel, Y.-A. Chen, Q. Zhang, K. Chen, J.-W. Pan, Experimental demonstration of a heralded entanglement source. *Nature Photonics* **4**, 549–552 (2010). 67, 69

[115] C. Śliwa, K. Banaszek, Conditional preparation of maximal polarization entanglement. *Phys. Rev. A* **67**, 030101 (2003). 67

[116] R. J. Young, R. M. Stevenson, A. J. Hudson, C. A. Nicoll, D. A. Ritchie, A. J. Shields, Bell-inequality violation with a triggered photon-pair source. *Phys. Rev. Lett.* **102**, 030406 (2009). 69

[117] R. M. Stevenson, C. L. Salter, J. Nilsson, A. J. Bennett, M. B. Ward, I. Farrer, D. A. Ritchie, A. J. Shields, Indistinguishable entangled photons generated by a light-emitting diode. *Phys. Rev. Lett.* **108**, 040503 (2012). 69

[118] C. L. Salter, R. M. Stevenson, I. Farrer, C. A. Nicoll, D. A. Ritchie, A. J. Shields, An entangled-light-emitting diode. *Nature* **465**, 594–597 (2010). 69

[119] M. Hillery, V. Bužek, A. Berthiaume, Quantum secret sharing. *Phys. Rev. A* **59**, 1829–1834 (1999). 71

[120] P. G. Kwiat, Hyper-entangled states. *Modern Optics* **44**, 2173–2184 (1997). 71

[121] N. Gisin, S. Pironio, N. Sangouard, Proposal for implementing device-independent quantum key distribution based on a heralded qubit amplifier. *Phys. Rev. Lett.* **105**, 070501 (2010). 71

[122] L. K. Shalm, Private communication. 84

[123] G. Tóth, O. Gühne, Detecting genuine multipartite entanglement with two local measurements. *Phys. Rev. Lett.* **94**, 060501 (2005). 97, 106